Shape Evolution in Neutron-Rich Si Isotopes Towards the Neutron Magic Number $N = 28$

Doctoral Dissertation

Masafumi Matsushita

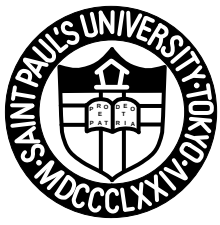

Department of Physics, Rikkyo University

2013

Abstract

Shape Evolution in Neutron-Rich Si Isotopes Towards the Neutron Magic Number N=28

By

Masafumi Matsushita

Excited states in the nuclei ^{38,40,42}Si have been studied using in-beam γ-ray spectroscopy following multi-nucleon removal reactions to investigate the systematics of excitation energies along the $Z = 14$ isotopic chain. The $N = 28$ isotope ^{42}Si can be regarded as a magic nucleus in the traditional shell model since a large energy gap exists at $N = 28$ due to the spin-orbit splitting. The disappearance of the $N = 28$ shell closure together with a large deformation, however, has been suggested from the observation of a low energy 2^+_1 state. Several experiments have been performed to investigate the structure of ^{42}Si so far, but no experimental data have been reported on higher-lying states, which may contribute valuable information on the nature of the collectivity and/or shell evolution. In order to study these states, we performed multi-nucleon removal reactions with radioactive isotope beams of ^{40}S and ^{44}S at the RI Beam Factory accelerator complex operated by the RIKEN Nishina Center and CNS, University of Tokyo. Owing to the high secondary beam intensities, several γ-ray lines, which include candidates for the $4^+_1 \rightarrow 2^+_1$ tranditions, were observed for the first time in addition to the $2^+_1 \rightarrow 0^+_{g.s.}$ γ-ray transitions. Systematics of the energies of the 2^+_1 states and the energy ratios between the 4^+_1 and 2^+_1 states indicate a rapid evolution of deformation and support the previously suggested disappearance of the $N = 28$ shell closure in ^{42}Si.

Contents

List of Figures

List of Tables

Chapter 1

Introduction

Atomic nuclei is a many-body system composed of nucleons bound mainly by the strong force. It has provided a rich laboratory for the study of quantum phenomena and mesoscopic science since the discovery by Ernest Rutherford at the begining of the 20th century [1]. A lot of challenges have been performed to develop a comprehensive understanding of the nuclear structure, the force between nucleons, and the nature of nuclear interactions with each other and with other subatomic particles. In order to gain an unified understanding of the structure of atomic nuclei, the evolution of properties with respect to changes in proton and/or neutron numbers is the crucial questions that must be answered.

One of the most predominant results from experimental studies on such nuclear properties was nuclear shell closure. The resultant "magic numbers" of 2, 8, 20, 28, 50 and 126 have been provided experimentally by a variety of systematic behaviors of physical properties, such as nucleon separation energies, level densities and nucleon capture cross sections. Independent-particle models, where nucleons move independently in a nuclear potential, can demonstrate the magic numbers. In 1949, Mayer [2, 3, 4] and Jensen [5] have independently succeeded to reproduce all the magic numbers by incorporating a strong spin-orbit force into the residual interaction of a nuclear mean-field potential, which pulls down the $l + 1/2$ orbital and pulls up the $l - 1/2$ orbital. This model, referred to as "shell model", explained well most of the ground state properties of nuclei at and near the stability line.

However, there is no well-founded approach to predict structure of nuclei in which numbers of protons and neutrons are extremely unbalanced, since the experimental evidences for the nuclear shell closure are rather limited in region at and near the stability

line where the number of both nucleons are well balanced. It is now well established that magic numbers are not universal and develop along the nuclear chart.

1.1 Studies on Unstable Nuclei

Experimental nuclear physics initially focused on stable nuclei, which comprise only about 300 of the 10,000 nuclei predicted to exist. The research on unstable nuclei not found in nature has achieved significant progress with the development of technology in providing radioactive beams over the last few decades. The method based on the projectile fragmentation reaction of stable nuclei beam has been employed to produce secondary radioactive beams at intermediate and high energies in most of the radioactive beam facilities such as LBL [6], GANIL [7], NSCL [8], GSI [9], and RIKEN [10]. The isotope-separator-on-line (ISOL) plus post-acceleration method has been employed at other facilities such as OSTIS [11] and ISOLDE [12] to produce low secondary beams. An attractive feature of the secondary beams produced by the fragmentation reaction is wide accessibility to nuclei far from stability line, whereas weak intensities and large emittances of the secondary beams make it difficult to perform sound spectroscopic experiments. Recently, Radioactive Isotope Beam Factory (RIBF), a new radioactive beam facility, was constructed at RIKEN [13], where the production mechanism of radioactive isotopes is based on projectile fragmentation reaction and in-flight fission of uranium beam. All the stable nuclei from proton to uranium can be accelerated to around 350 MeV/nucleon in RIBF and wide range of radioactive nuclei can be produced as secondary beams. The other new facilities such as FRIB at NSCL and SPIRAL2 at GANIL are being constructed. Experimental studies investigating structure of unstable nuclei in above facilities have discovered novel phenomena which had not been revealed in the nuclei at and near the stability line.

A breakdown of neutron magic number $N = 20$ in neutron-rich region was one of such discovery. The presence of atypical binding energies for $N = 20$ and 21 sodium isotope ^{31,32}Na was, at first, investigated experimentally by Thibault et al. [14]. The enhancement of the binding energy observed at $N = 20$ and 21 along Na isotopic chain exhibited a quite different behavior from other isotopic chain, which shows the decreased binding energies at the neutron magic number. This irregularity was suggested to be due to the nuclear deformation. The inversion of the neutron single particle level of $1d_{3/2}$ and $1f_{7/2}$ orbitals was proposed by Warburton et al. [15]. They referred to this deformation

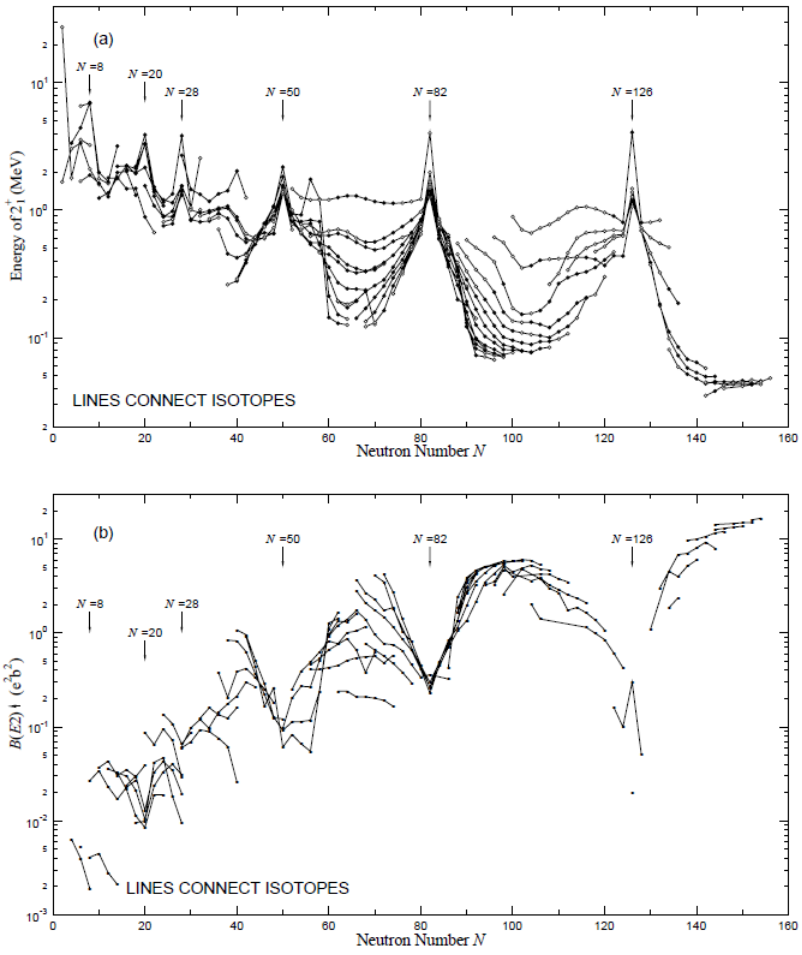

Figure 1.1: Panel (a) and (b) show energies of the first 2^+ states and reduced electric quadrupole transition probabilities $B(E2; 0_1^+ \rightarrow 2_1^+)$ for the even-even nuclei as a function of neutron number, respectively. Both figures were taken from Ref. [16].

region comprising the nine nuclei of ^{30,31,32}Ne, ^{31,32,33}Na and ^{32,33,34}Mg as the "island of inversion".

The indicator of nuclear magicity is not only the nucleon binding energies. Some even-even nuclei have relatively high-energy first 2^+ (2_1^+) states and are thus distinct from their even-even neighbors. A high energy of the 2_1^+ excited state and a corresponding low electric quadrupole transition probability $B(E2; 0_1^+ \rightarrow 2_1^+)$ are in common characteristic signatures of shell closures. The systematic trends of the 2_1^+ excitation energies and $B(E2; 0_1^+ \rightarrow 2_1^+)$ transition strengths for the even-even nuclei are shown as a function of number of neutron in Figure 1.1. The enhanced energies of the 2_1^+ states and the lowering $B(E2; 0_1^+ \rightarrow 2_1^+)$ values are clearly visible at neutron magic number. A similar

trend can be seen in proton case also [16]. In contrast to this, the low energy of the 2_1^+ state at 885.5(7) keV was obtained for $N = 20$ nucleus ^{32}Mg by β-decay spectroscopy of ^{32}Na and regarded as an indication of a large deformation [17, 18]. Motobayashi et al. performed the first experiment of in-beam γ-ray spectroscopy involving intermediate energy Coulomb excitation of ^{32}Mg [19]. The resultant large $B(E2; 0_1^+ \rightarrow 2_1^+)$ value showed a robust evidence for the enhanced collectivity and the breakdown of $N = 20$ magicity in ^{32}Mg. Latter works, in-beam γ-ray spectroscopy on ^{30,32,34}Mg, performed by Yoneda et al. [20] and Takeuchi et al. [21] revealed the shape evolution from a spherical shape of ^{30}Mg to a well-deformed shape of ^{34}Mg by measuring 2_1^+- and 4_1^+- states energies.

The breakdown and appearance of the magic number have been revealed also in other region. The melting of $N = 8$ shell closure [22, 23] suggested that intruder configuration of the neutron $2s_{1/2}$ orbital into the neutron p shell. The appearance of the magicity at $N = 16$ is suggested to be formed by the strong tensor part of nucleon-nucleon interaction [24]. In proton-rich region, a recent study on the $Z = 16$ nucleus ^{28}S [25] revealed a small $B(E2; 0_1^+ \rightarrow 2_1^+)$ value with a hindrance of proton collectivity relative to that of neutron, implying the $Z = 16$ magicity.

These studies, as shown in Figure 1.2, revealed that the concept of the nuclear magic number established in nuclei at and near the stability line is no longer available in region far from stability line. It is, however, a fundamental and at present open question whether and how the changes of the major shell closures and magic numbers, causing shape deformations, occur in very neutron-rich nuclei.

1.2 The Modification of Shell Structure at $N = 28$

The major shell closure of magic number 28 is the lightest shell closure caused by the spin-orbit force, and thus is responsible for all shell closures in heavier nuclei. Recently, the shell structure of neutron-rich nuclei in the vicinity of $N = 28$ has attracted much interests because of some experimental indications for shell structure modification. A lot of experimental data have been collected on $N = 28$ isotones and neighboring nuclei. β - decay spectroscopies, mass measurements, direct reactions, Coulomb excitation and γ-ray spectroscopies were performed and served to constrain theoretical models aiming at describing this mass region.

Figure 1.4 shows the systematics of energies of the 2_1^+ states in even-even nuclei with proton number ranging from $Z = 10$ to $Z = 20$ and neutron number ranging from $N = 18$

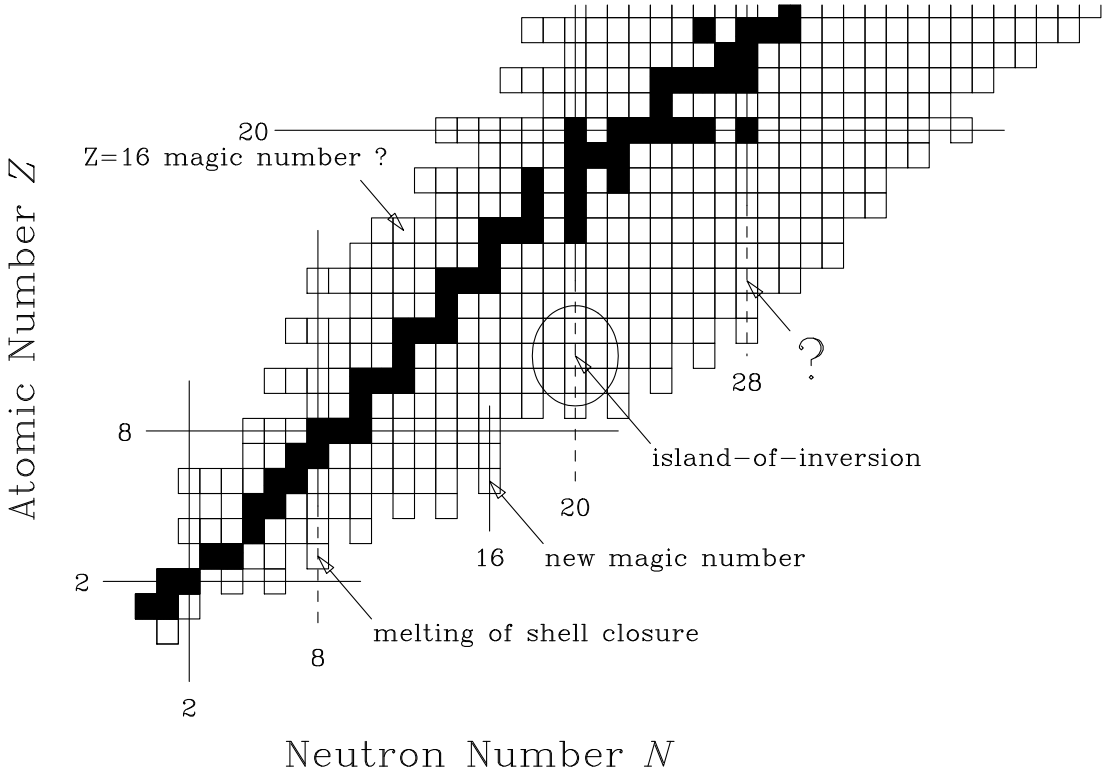

Figure 1.2: Nuclear chart in light- and medium mass region.

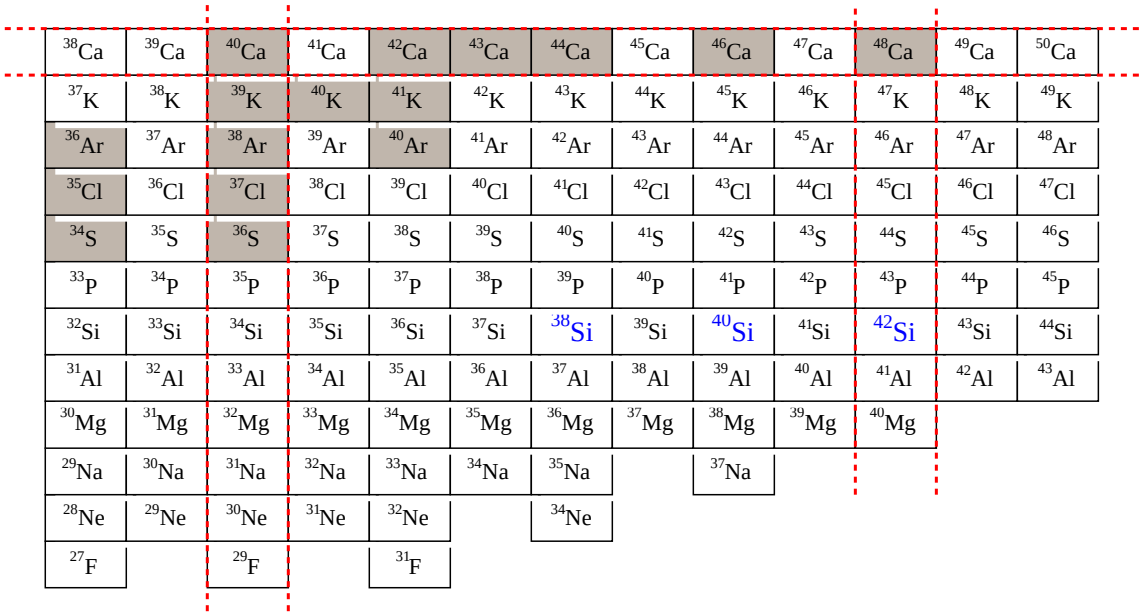

Figure 1.3: Nuclear chart in the vicinity of neutron-rich nuclei ^{38,40,42}Si is shown. The red dashed lines indicates $Z = 20$ and $N = 20, 28$ magic number.

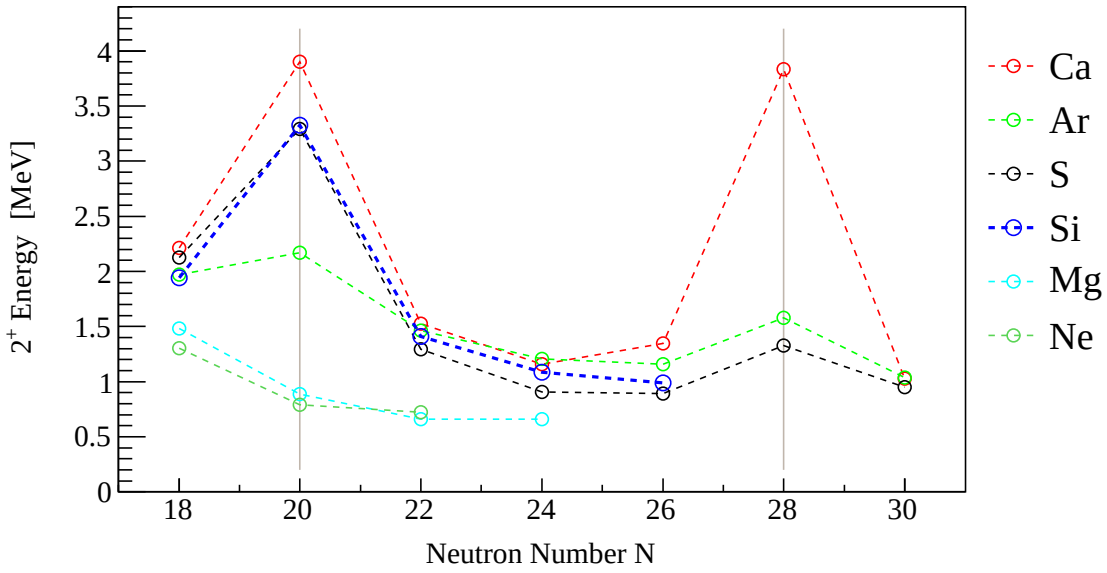

Figure 1.4: Systematics of energies of the 2_1^+ states in neutron-rich even-even nuclei from $Z = 10$ and $N = 20$ to $Z = 20$ and $N = 28$ are shown.

to $N = 30$. As mentioned before, the lowering 2_1^+ energies at $N = 20$ nuclei ^{30}Ne and ^{32}Mg along each isotopic chain are taken as a property of deformed nuclei, while enhanced 2_1^+ energies indicate a spherical shape and persistency of the $N = 20$ magicity in ^{34}Si, ^{36}S, ^{38}Ar and ^{40}Ca. The $N = 20$ shell closure, bound by two orbitals of opposite parity, $d_{3/2}$ and $f_{7/2}$, remains remarkably rigid against quadrupole deformation from $^{40}_{20}$Ca to $^{34}_{14}$Si even after the removal of six protons in the direction of the neutron-rich region [26]. Contrastively, a more rapid shell evolution was revealed in the case of $N = 28$ isotones. Compared with the stable and the spherical doubly magic nucleus ^{48}Ca, a reduction of the $(1f_{5/2})_\nu$ single particle level by 330(90) keV corresponding to $\simeq 10(2)\%$ reduction of the spin-orbit splittings in the f orbital was obtained from the missing mass spectroscopy with $^{46}\mathrm{Ar}(d,p)^{47}\mathrm{Ar}$ transfer reaction [27]. The more neutron-rich $N = 28$ isotone ^{44}S has a structure of shape coexistence. The excited 0_2^+ isomeric state observed at 1365-keV, only 36-keV above the 2_1^+ state, is considered to have a spherical normal configuration with a weak $B(\mathrm{E2}: 0_2^+ \rightarrow 2_1^+)$ [28], in which the neutrons are confined to the orbits below the $N = 28$ gap, whereas the ground state is regarded as originating from the deformed two particle-two hole intruder configuration from a relatively strong $B(\mathrm{E2}; 0_1^+ \rightarrow 2_1^+)$ [29].

For further investigations of the shell evolution at $N = 28$, the next neutron-rich even-

even isotone ^{42}Si also can be regarded as an important milestone . Recently in-beam γ-ray spectroscopies in search for the position of the first 2^+ state in ^{42}Si have been performed by employing two-proton removal reaction at NSCL [30, 31] and GANIL [32, 33]. However, the controversial results have been reported from these two experiments. Though the significant γ-ray transition could not be observed in NSCL case, a nearly spherical shape caused by a large energy gap at $Z = 14$ subshell closure due to the $1d_{5/2}$ - $1d_{3/2}$ spin-orbit splitting was suggested from a small two proton removal cross section $\sigma_{-2p}(^{44}\mathrm{S}\rightarrow^{42}\mathrm{Si})$, which was taken as an indication in favor of a magic spherical nuclei [30, 31]. Shell model and eikonal direct reaction calculation for two proton removal cross section with several sets of parameters of $Z = 14$ and $N = 28$ shell gap were compared with the experimental result, and an enhanced energy gap between the $s_{1/2}$ - $d_{3/2}$ pair and the $d_{5/2}$ proton single particle level, inducing ^{42}Si to be a spherical shape, was established. On the other hand, the low energy of the 2_1^+ state at 770(15) keV was reported in GANIL case from observation of de-excitation γ-ray [32, 33] and regarded as a strong evidence for the disappearance of the $N = 28$ shell closure at ^{42}Si. The very short β-decay lifetimes of the $^{40-42}$Si nuclei [34] also support the picture of derformed ground state configurations. The experimentally measured atomic mass of ^{42}Si could be obtained either for a spherical or deformed shell closure through the comparison with spherical liquid drop model [35]. Beyond $N = 28$, the $N = 30$ nuclei ^{46}S and ^{48}Ar were investigated by in-beam γ-ray spectroscopy with single nucleon exchange reactions [36]. In this work, the monopole-shift and pairing correction in large-scale shell-model calculation in the *sd-pf* shell were modified in such a way as to reproduce the obtained 2_1^+ states, but this shows that the $N = 30$ isotones are much less impacted by the mechanisms driving the nuclear structure at $N = 28$. Therefore, further direct investigations on ^{42}Si, such as the level structure of low-lying and/or highly excited states and the $B(\mathrm{E2}; 0_1^+ \rightarrow 2_1^+)$ quadrupole transition strength, is essential for the understanding on the $N = 28$ shell structure in this mass region.

As for the silicon isotopes, the continuous decrease of the 2_1^+ state energies from $N = 22$ isotope ^{36}Si to $N = 26$ isotope ^{40}Si can be regarded as an indication for a development of quadrupole collectivity. The larger $B(\mathrm{E2}; 0_1^+ \rightarrow 2_1^+)$ values of ^{36}Si and ^{38}Si than that of ^{34}Si, in fact, were observed [26]. The low excitation energy, 985-keV, of the 2_1^+ state in ^{40}Si, suggesting the narrowing of the $N = 28$ shell gap [37], is also considered to be due to the enahanced collectivity. On the other hand, the information on other yrast states, such as 4_1^+ and 6_1^+, are rather limited, which serves as significant indicator for the

nature of quadrupole collectivity, and the nuclear shape. The nuclear collective models describe collective excitation as a deformation (the rotational models) or a vibration (the vibrational models) of the nucleus as a whole. From a model assumption of a statically deformed rotor, the energy ratio between the 4_1^+- and 2_1^+- states is obrained to be 3.3, while it is obtained to be 2.0 from the assumption of a harmonic vibration.

1.3 Thesis Objective

This thesis deals with in-beam γ-ray spectroscopies of the neutron-rich silicon isotopes ^{38,40,42}Si in search for the energies of the 2_1^+- and the higher states, especially for the 4_1^+ states. One of the aims is to determine and/or confirm the 2_1^+ state energy in ^{42}Si which has been suggested to be at the relatively low energy of 770-keV by one of the previous work. The 2_1^+ state energy in even-even nucleus serves as a good indicator for the quadrupole collectivity, together with $B(\mathrm{E2}; 0_1^+ \rightarrow 2_1^+)$ which is more direct physical quantity. Since the 2_1^+- and 4_1^+- state energies are the information reflecting the collective property of even-even nuclei, systematical study on both two states provides whether and how the collectivity develops along the $Z = 14$ isotopic- and the $N = 28$ isotonic- chains. In order to investigate the energies of the excited states in these Si isotopes, in-beam γ-ray spectroscopy experiment was performed. Multi nucleon removal reactions from S isotopes were employed to produce excited states of Si isotopes. This reaction has a high accesibility to the high spin excited states, especially to yrast states, and therefore gives a possibility to determine excitation energy of the 4_1^+ state in addition to that of the 2_1^+ state.

In Chapter 2, experimental method and setup are explained in detail. Chapter 3 deals with the procedures of data analysis for deducing the excitation energy. Experimental results and discussions are presented in Chapter 4. The summary and conclusions are given in Chapter 5.

Chapter 2

The Experiment Setup

The purpose of the experiment was to investigate excited states of the neutron-rich ^{38,40,42}Si nuclei systematically via multi nucleon removal reaction. Secondary beams of ^{40,44}S were produced and separated by the in-flight fragment separator BigRIPS [38] using a 345 MeV/nucleon ^{48}Ca primary beam incident on a 15 mm-thick ^{9}Be target. The secondary beams then were bombarded on a secondary reaction target of 2.54 g/cm^2 thick carbon to induce multi nucleon removal reactions. Reaction products produced by the secondary reaction target were collected and analysed by the ZeroDegree spectrometer. Section 2.1 presents a description of BigRIPS, the ZeroDegree spectrometer and the secondary reaction target.

A cocktail beam containing many reaction products was produced by BigRIPS and more fragments were produced by the secondary reaction target. Therefore, in order to identify the nuclei event by event, several different types of beam line detectors were used. An explanation of these detectors is given in Section 2.2. The γ rays induced by secondary reactions in coincidence with the projectiles and the ejectiles were detected by the γ-ray spectrometer DALI2 [39]. Section 2.3 describes this γ-ray spectrometer. The electric circuit system and the trigger conditions are described in Section 2.4. Section 2.5 describes the data sets obtained in the present experiment.

2.1 Production and Identification of the RI Beams

In order to measure the C(^{40}S,^{38}Si+γ), C(^{44}S,^{40}Si+γ) and C(^{44}S,^{42}Si+γ) reactions, ^{40}S and ^{44}S secondary beams were produced by projectile fragmentation reactions of a ^{48}Ca (A = 48, Z = 20) primary beam on a ^{9}Be (A = 9, Z = 4) target. The average primary beam

intensity was 70 pnA (×20 enA). Among a variety of fragmentation products, ^{40}S and ^{44}S were collected and separated by the in-flight fragment separator BigRIPS. Secondary beams produced by BigRIPS were transported and bombarded a secondary reaction target of 2.54 g/cm^2 thick carbon located in the F8 focal plane in the ZeroDegree spectrometer. ^{38}Si, ^{40}Si and ^{42}Si reaction products were produced by multi-nucleon removal reactions and identified by the ZeroDegree spectrometer. In the following two sections, a general description of BigRIPS and the ZeroDegree spectrometer is given.

2.1.1 In-flight Fragment Separator BigRIPS

The experiment was performed at the RI Beam Factory (RIBF) of RIKEN Nishina Center (RNC). Figure 2.1 shows a schematic layout of the facility. Because of the high primary beam intensity and high cross section for the secondary beams of interest, a primary beam of ^{48}Ca was chosen to produce the radioactive isotope (RI) beams of ^{40}S and ^{44}S through the projectile fragmentation reactions. The ^{48}Ca primary beam was accelerated by a heavy-ion linear accelerator (RILAC) and a combination of four ring cyclotrons, RRC, fRC, IRC and SRC up to 345 MeV/nucleon, and then transported to the F0 focal plane of BigRIPS. At the entrance of BigRIPS, a production target of 15 mm thick ^{9}Be was placed.

BigRIPS was designed to be a two-stage RI beam separator. The main characteristic features of the BigRIPS are listed in Table 2.1. The first stage from the production target to the F2 focal plane comprises a two-bend achromatic spectrometer, consisting of four superconducting quadrupole triplets (STQ) (STQ1 to STQ4) and two room-temperature dipoles (D1 and D2) with a bending angle of 30 degrees. This first stage is used to produce and separate secondary beams. The secondary beams can be selected by their magnetic rigidity, $B\rho = p/Z$, if a slit (momentum slit) is inserted at the momentum dispersive focal plane F1. As the isotopes produced by the projectile fragmentation reactions have almost the same velocities, a rough separation in terms of their mass-to-charge ratio A/Q is achieved by setting the appropriate magnetic field intensity of D1 and momentum slit at F1. An achromatic wedge-shaped degrader made of aluminum was inserted at F1, which preserved the momentum dispersion. Different $B\rho$ values were produced for the different isotopes due to the energy loss differences in degrader and were analysed by the second dipole magnet (D2) and selected by the slits placed at the achromatic focal plane F2. As a consequence, the $B\rho$ selection was approximately proportional to $A^{2.5}/Z^{1.5}$. Isotopes with similar A/Z and $A^{2.5}/Z^{1.5}$ were therefore selected in the first stage of the BigRIPS.

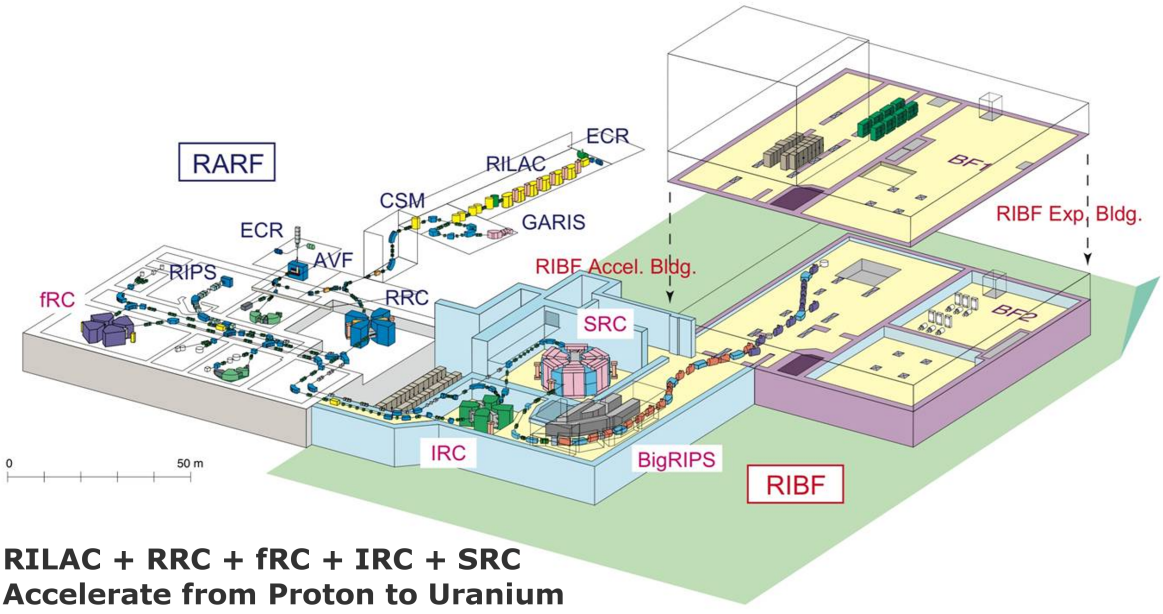

Figure 2.1: Schematic layout of the RIKEN Nishina Center (RNC) facility. The ^{48}Ca primary beam was accelerated by RILAC, RRC, fRC, IRC and SRC, and was transported to BigRIPS.

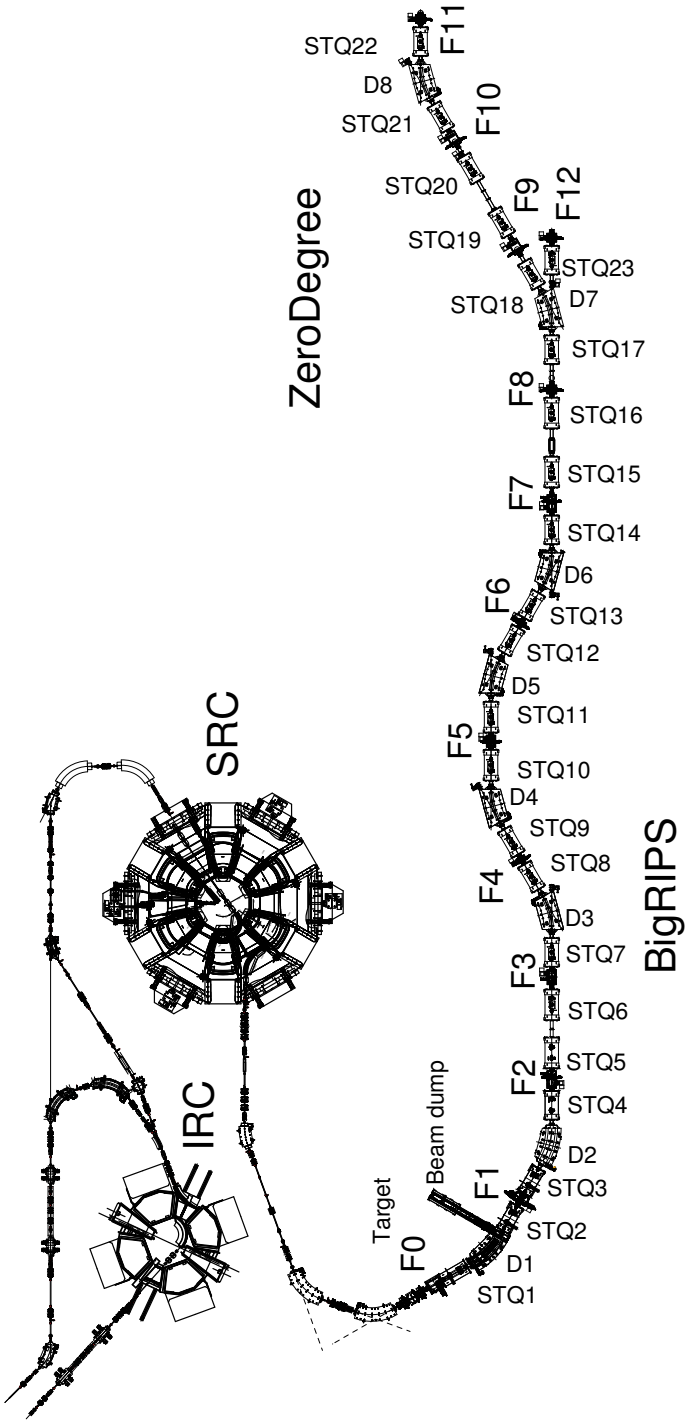

Figure 2.2: Schematic layout of the RIBF facility. The ^{48}Ca primary beam was accelerated by IRC and SRC, and was delivered to BigRIPS (F0 to F7) in order to produce secondary beams. Ejectiles produced at F8 by secondary reactions were analysed by the ZeroDegree spectrometer (F8 to F11).

Configuration	Tandem
Magnet configuration	First stage : TQ-D-TQ-TQ-D-TQ
Angular acceptance	Horizontal : 80 [mrad]
	Second stage : TQ-D-TQ-TQ-D-TQ-TQ-D-TQ-TQ-D-TQ
	Vertical : 100 [mrad]
Momentum acceptance	6 [%]
Total path length	77 [m] (F0-F7)
Momentum dispersion	First stage : -23.1 [mm/%]
	Second stage : 33 [mm/%]
Momentum resolution	First stage : 1290
	Second stage : 3300 [assuming ΔX = 1 mm]
Focal plane	F1 : momentum dispersive
	F2, F3 : achromatic
	F4, F5, F6 : momentum dispersive
	F7 : achromatic

Table 2.1: Main characteristic features describing the BigRIPS in-flight fragment separator in the tandem configuration. (write some important point ,Acceptance, Resolution , compared to other facility)

The second stage from the F3 focal plane to the F7 focal plane consisted of eight STQs (STQ7 to STQ14) and four dipoles (D3 to D6) with a bending angles of 30 degrees, making BigRIPS a four-bend achromatic spectrometer. The intermediate focal plane F5 was momentum dispersive, while the final focal plane F7 was doubly achromatic. As the secondary beams were composed of several isotopes, the second stage of BigRIPS was employed to identify them by mass and charge. Delay-line parallel plate avalanche counter PPAC [40] and plastic scintillators for timing were placed at the focal planes of the second stage to measure the $B\rho$, the time-of-flight and the energy loss of the secondary beams. The detailed descriptions of these beam line detectors are given in Section 2.2. Using these detectors, the secondary beams were identified on an event-by-event basis using the standard TOF-$B\rho$-ΔE method. The tagged (identified) secondary beams were delivered to the F8 focal plane in which the carbon secondary reaction target was placed. The design values for BigRIPS included angular acceptances of 80 mrad horizontally and 100 mrad vertically, and momentum acceptance was 6 %.

2.1.2 ZeroDegree Spectrometer

The ZeroDegree spectrometer from the F8 focal plane to the F11 focal plane consisted of six STQs (STQ17 to STQ22) and two dipoles (D7 to D8) with a bending angle of 30 degrees, making ZeroDegree a two-bend spectrometer. Table 2.2 shows the main characteristic features of the ZeroDegree spectrometer in the larger acceptance mode. Secondary beams separated and identified by BigRIPS bombarded a secondary carbon reaction target placed at the F8 focal plane at the entrance of the ZeroDegree spectrometer. ZeroDegree was employed to collect and identify the reaction products including ^{38}Si, ^{40}Si and ^{42}Si. The achromatic large acceptance mode was chosen for the experiment because of its high angular acceptance (90 mrad in horizontal and 60 mrad in vertical) and sufficient momentum resolution (1240 assuming Δx = 1 mm).

2.1.3 The Reaction Target

As a solid carbon can be treated easily, it was chosen as a reaction target. In general, a higher γ-ray yield can be obtained by a thicker target. On the other hand, a thick target causes a large velocity shift between projectile and ejectile particle, which may spoil the resolution of the γ-ray peaks due to the Doppler broadening. Also a thick target has a large uncertainty in the γ-ray emission position, which affects the energy resolution. With

Ion optics	Achromatic large acceptance mode
Magnet configuration	TQ-D-TQ-TQ-TQ-TQ-D-TQ
Angular acceptance	Horizontal : 90 [mrad]
	Vertical : 60 [mrad]
Momentum acceptance	6 [%]
Total path length	36 [m] (F8-F11)
Momentum dispersion	22.4 [mm/%]
Momentum resolution	1240
Focal plane	F8 : achromatic
	F9, F10 : momentum dispersive
	F11 : doubly achromatic

Table 2.2: Main characteristic features describing the ZeroDegree spectrometer in the achromatic large acceptance mode used in the experiment. (write some important point ,Acceptance, Resolution , compared to other facility)

these considerations, a 2.54 g/cm^2 carbon reaction target was installed at the F8 focal plane of the ZeroDegree spectrometer. The target thickness was determined within 1% uncertainty.

2.2 The Particle Identification Detectors

The descriptions of detectors used to monitor the incident secondary beams and ejectiles are given here. Particle identification of the incident secondary beams was performed by using plastic scintillators placed at the F3, F5 and F7 focal planes of BigRIPS. Plastic scintillators placed at the F8 and F11 focal planes, double-PPACs in the F8 and F9 focal planes, and the tilted electrode gas ionization chamber TEGIC [41] at the F11 focal plane were used for particle identification of the ejectiles.

2.2.1 Delay-line Parallel Plate Avalanche Counters (delay-line PPACs)

Secondary beam and ejectile position were monitored at each focal plane by two-dimensional delay-line parallel-plate avalanche counters (PPACs). Figure 2.3 shows a

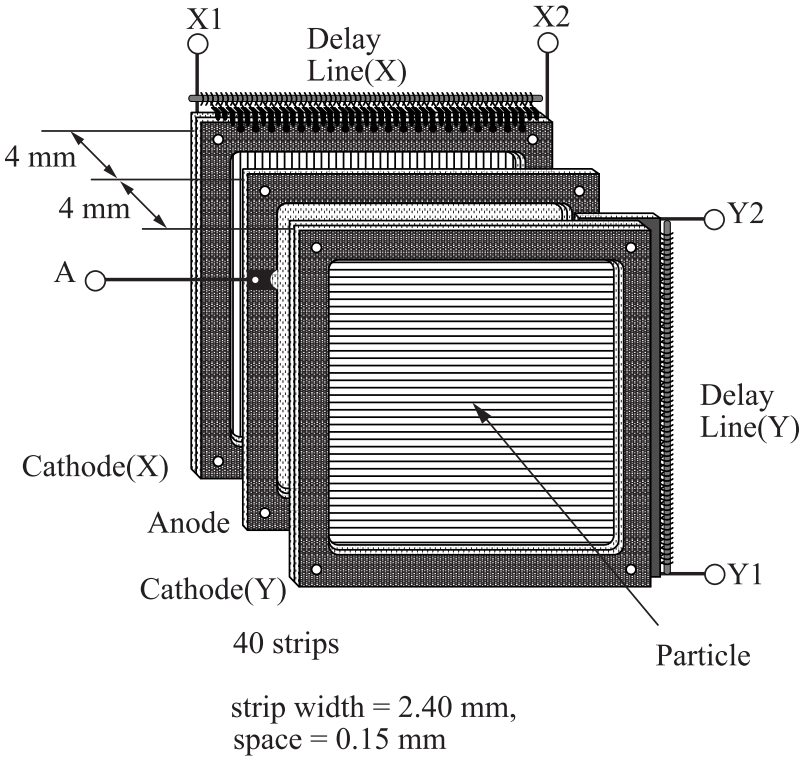

Figure 2.3: Schematic view of the delay-line PPAC.

schematic layout of the PPAC, which consists anode- and two cathode plates separated by 4mm. An anode plate is placed between two cathode plates. Each cathode consists of 2.4 mm pitch strips, which are connected to delay-lines of 1.25mm/nsec delay with 0.15 mm inter-strip spacing. The cathode was made by evaporation of Al or Cu and the base material was 4 μm-thick Mylar foil, which was mounted onto G10 frame of 2mm thickness. The anode was also made by Al or Cu evaporation onto 2 μm-thick Mylar foil and the spacing between the anode and the cathode was 4 mm. The hit position of x- and y-directions is measured by the cathode with strips in the horizontal and vertical axes, respectively. The hit position was deduced from the time differences of the signals at both ends.

The typical position resolution for the PPAC is about 0.5 mm (r.m.s.) for ^{12}C although it might differ, depending on operation condition such as the beam energy, the beam rate, the charge of beam, the supplied bias voltage and gas pressure. For each PPAC unit, five signals, two from both ends of the cathodes and one from the anode, were obtained. Each signal was then split into two signals to be used as timing and analog signals, respectively. Therefore, for each PPAC unit, five timing signals, namely $Tx1$, $Tx2$, $Ty1$, $Ty2$ from both

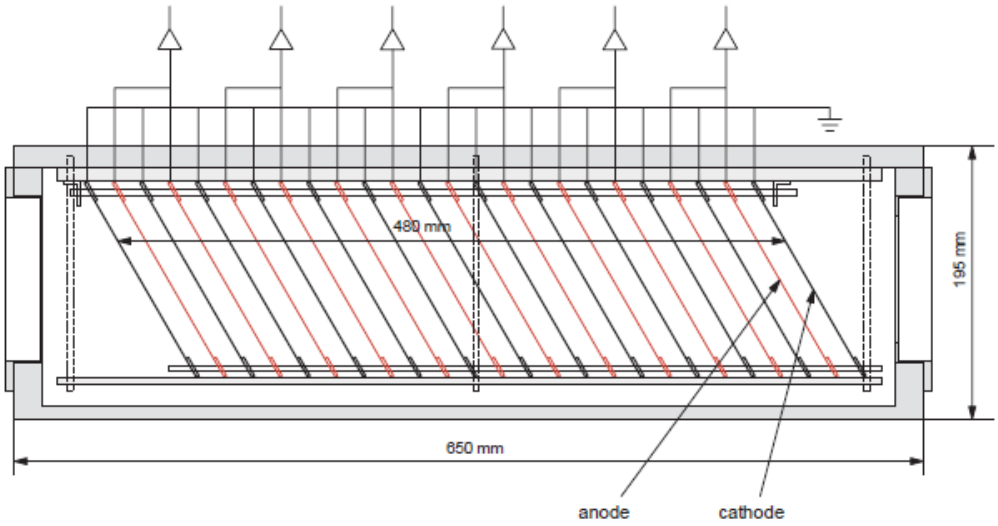

Figure 2.4: Schematic view of the TEGIC. The figure was taken from Ref.[- - -]

ends of cathodes and T_{Anode} from the anode, were obtained. Similarly five analog signals, $Qx1$, $Qx2$, $Qy1$, $Qy2$ and Q_{Anode} were also obtained. A brief description on the electric circuits involved is given in Section 2.4.1. In order to enhance the detection efficiency of one plane, double-PPAC that consists of two PPAC units combined together back-to-back and two detector windows of 12 μm aluminized Mylar foils was designed and installed as a standard position detector of the BigRIPS and the ZeroDegree spectrometer. In the present experiment, each double-PPAC was operated with C_3F_8 gas at a constant pressure around 10 torr and bias voltage around 850 V supplied to anode.

2.2.2 The Tilted Electrode Gas Ionization Chamber (TEGIC)

The tilted electrode gas ionization chamber (TEGIC) placed at the F11 focal plane of the ZeroDegree spectrometer was employed as a ΔE detector to identify atomic number of the ejectiles after the secondary target. Figure 2.4 shows a schematic view of the TEGIC, which consisted of twelve anode planes and thirteen cathode planes placed alternately in 20 mm steps. As a total of 24 parallel plate ionization chambers stacked together back-to-back were utilized, the total length of the TEGIC was 480 mm. The material for the anode and cathode was 4 μm-thick Mylar aluminized on both side. The inner diameter of the electrodes was 116 mm. The whole setup was housed in an aluminum chamber. The beam entrance and exit windows consisted of 150 μm-thick Kapton sheets. Always

the anode plane readout was connected in pairs inside the chamber. Thus, in total six channels were read out by a total of six individual feedthroughs. All cathode plane were connected and grounded commonly. A gas mixture of Ar-CH_4 (Ar 90 %, CH_4 10 %) was used as counting gas.

2.2.3 The Plastic Scintillation Detectors

For particle identification, the velocity of the ions was deduced on an event by event basis by measuring their time-of-flight (TOF). For this purpose, thin plastic scintillation detectors (material:BC-420) were installed in the F3, F5 and F7 focal planes for BigRIPS, and the F8 and F11 focal planed for the ZeroDegree spectrometer. The thickness of all plastic scintillators except at F7 was 1 mm. At F7 focal plane, a 2 mm-thick plastic scintillator was installed to gain more light output for energy loss measurement. For each plastic scintillator, two photo-multiplier tubes (HAMAMATSU H1949 PMT with third stage current boosters) were connected to its left- and right-side edges. The use of a PMT on both sides of the scintillators enabled position dependency corrections of the time information and the pulse height due to attenuation of scintillation photons. The timing information obtained from the plastic scintillators was used to deduce the TOF between F5 and F7, and between F8 and F11, respectively. Between the F5 and F7 focal planes, the particle identification of the secondary beam was performed using only the two plastic scintillators. In addition to the TOF information, for these two detectors the hit position of the beam was deduced from timing differences between the signals of the two PMTs and the pulse height information. The latter was was equivalent to the energy loss ΔE measurement.

2.3 The Devices for In-beam γ-ray Spectroscopy

The in-beam γ-ray spectroscopy setup installed at the F8 focal plane is shown schematically in Figure 2.5. It consisted of three items: A NaI(Tl) detector array for γ-ray detection, three PPACs for beam tracking and scattering trajectory determination, and a reaction target. The NaI(Tl) detectors surrounded the reaction target. Two PPACs were installed upstream from the reaction target, and the other one was located downstream. In general, γ rays are attenuated by material, depending strongly on their energy and the atomic number of the absorbing material. Therefore, as little material as possible should be placed between reaction target and the NaI(Tl) detector array. On the other hand, the

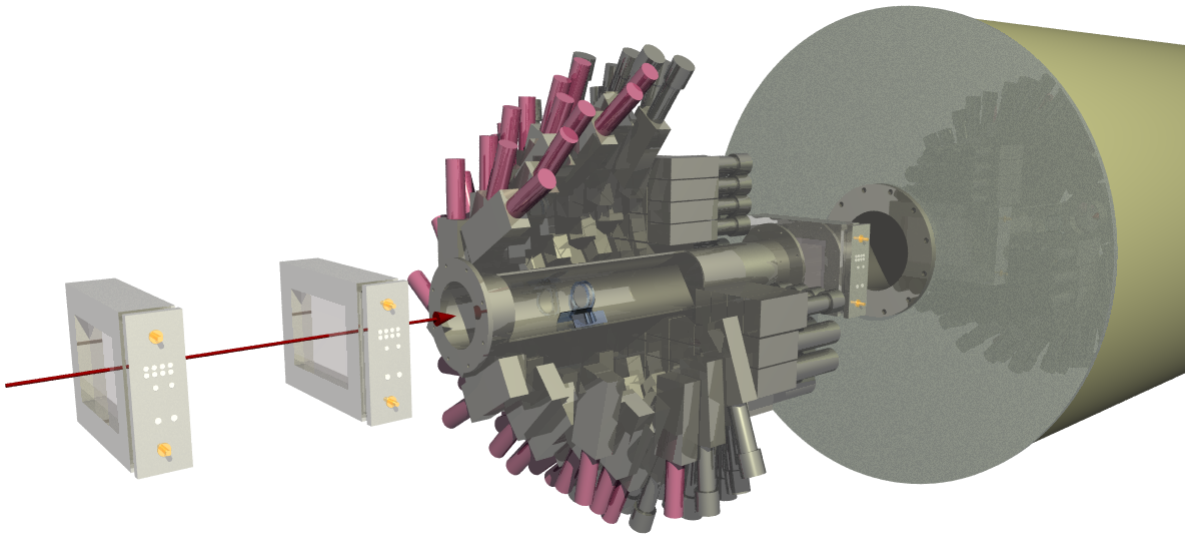

Figure 2.5: An schematic view of the in-beam γ-ray spectroscopy setup installed at the F8 focal plane. 186 NaI(Tl) detectors were arranged surrounding the reaction target and three PPACs were installed as beam tracking monitors.

high atomic number materials, such as Pb or Sn, has high attenuation capacities against low energy γ rays below 200 keV. These high Z materials are thus useful to reduce the background detection of X rays and low energy γ rays. Therefore, low energy atomic-background shielding was employed. The following sections explain the setup at the F8 focal plane in detail.

2.3.1 The γ-ray Detector Array DALI2

The Detector Array for Low Intensity radiation, DALI2, is a device designed for in-beam γ-ray spectroscopy experiments utilizing fast RI beams at the RIBF. DALI2 consists of 186 NaI(Tl) crystals, in total 560 kg of active scintillator material. The design values of DALI2 include a full-energy-peak efficiency of 25 % and an in-beam energy resolution of better than 12 % (FWHM) for 1 MeV γ rays emitted at velocities of $v/c \sim 0.6$.

The NaI(Tl) Scintillation Detectors

DALI2 consisted of three types of NaI(Tl) scintillation detectors, all of them had rectangular shapes. The sizes of the three different detector types are listed in Table 2.3. Each crystal was covered with about 2.8 mm MgO coating and a housing of 1 mm-thick

aluiminum. The typical intrinsic energy resolution was 4.8-, 3.6- and 2.7 % for 660 keV, 1132 keV and 1890 keV γ rays emitted from ^{137}Cs, ^{60}Co and ^{88}Y standard γ-ray sources, respectively. The employed photo-multiplier tubes are also listed in the table.

Company	Num. of piece	Crystal size [mm]	Photo-multiplier tube
Scionix	66	$80 \times 40 \times 160$	HAMAMATSU R580($\phi = 38$)
Saint-Gobain	88	$80 \times 45 \times 160$	HAMAMATSU R580($\phi = 38$)
Bicron	32	$61 \times 61 \times 122$	HAMAMATSU R1306($\phi = 51$)

Table 2.3: List of NaI(Tl) detectors utilized in the DALI2 array.

The DALI2 Configuration

The detector coverage of forward angles is particularly important for in-beam γ-ray spectroscopy at high velocities due to the Lorentz boost towards forward angles. In addition, large NaI(Tl) crystal volumes are required at forward angles to obtain high full-energy peak efficiency because the energies of the γ rays emitted in forward angles are shifted towards higher energies. Figure 2.6 shows the dependency between the Doppler shifted energy and the emission angles for different velocities.

In order to measure the de-excitation γ-ray from the reaction products, 186 NaI(Tl) detectors were arranged around the reaction target. Two types of NaI(Tl) detector arrangements were taken into consideration with the above features of in-beam γ-ray spectroscopy at high velocities. As shown in Figure 2.5, the layout consisted of eleven layers, each of them with 6 - 14 NaI(Tl) detectors arranged coaxially with respect to the beam axis. A wall-like part composed of a cluster of 64 NaI(Tl) detectors was installed in a closely packed configuration to cover the forward angles.

Figure 2.7 shows the polar angular coverage of the NaI(Tl) detectors obtained by Monte Carlo simulations based on GEANT4. The NaI(Tl) detectors cover polar angles ranging from 0.28 to 2.61 rad (16 to 150 deg). The NaI(Tl) detectors cover about 50 mrad ($\sim$7 deg) on average.

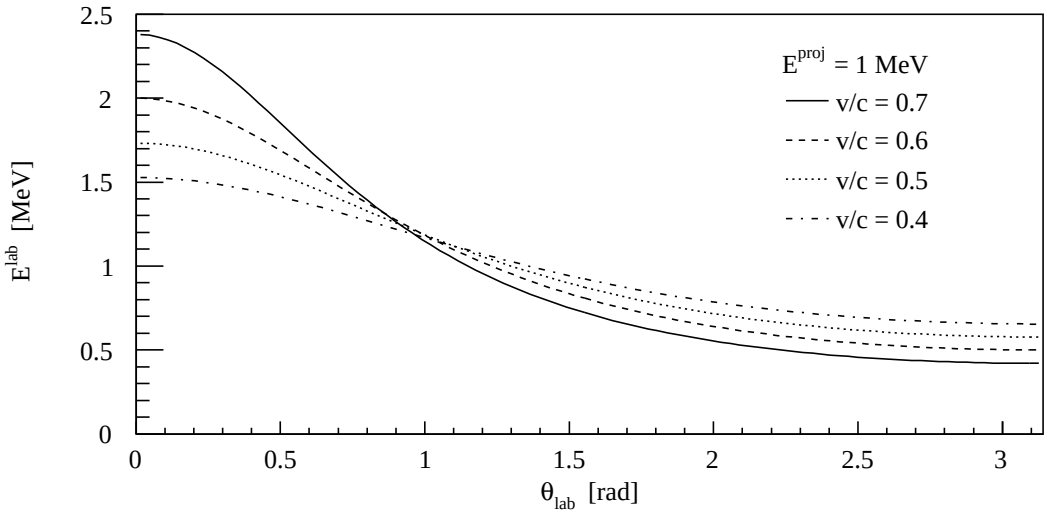

Figure 2.6: Doppler shifted energy in the laboratory frame of 1 MeV γ-ray as a function of the polar angle for different velocities.

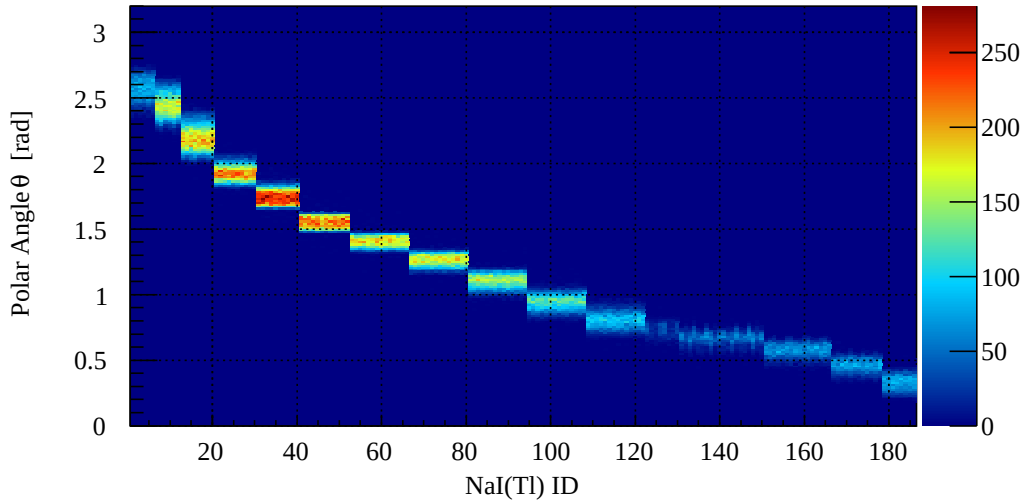

Figure 2.7: Angular coverage of DALI2 γ ray detector array are shown by 2-dimensional plot of NaI(Tl) detector ID and polar angle θ, which results from the Monte Carlo simulations.

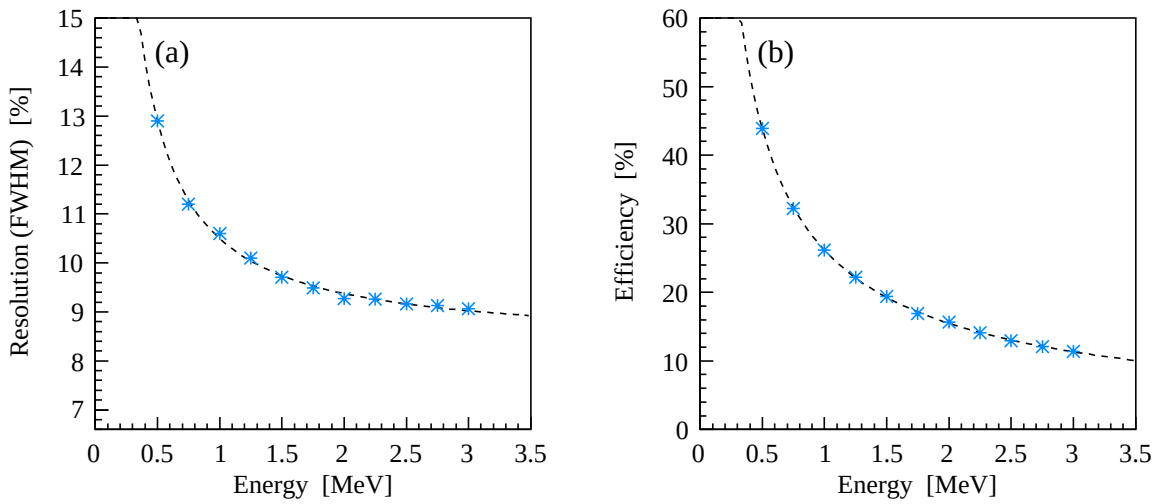

Figure 2.8: Shown are the energy resolution (a) and the full-energy-peak efficiency (b) as a function of γ ray energy obtained by Monte Carlo simulations. The beam velocity was $v/c = 0.6$. The results were fitted by a power function curve and indicated by a dashed line.

Energy Resolution and Full-Energy-Peak Efficiency

Figure 2.8 shows Monte Carlo simulation results based on GEANT4 for the energy resolution (FWHM), denoted by (a), and the full-energy-peak efficiency, denoted by (b), of DALI2 as a function of γ-ray energy. The beam velocity used in the simulation was $v/c = 0.6$. The simulated energy resolution was 10.6 and 9.9 % for 1 and 2 MeV γ rays, respectively, while the full-energy-peak (FEP) efficiency was 26.2 % and 15.7 %, respectively. A detailed explanation about the Monte Carlo simulations is given in Section 3.

2.3.2 Atomic-background

In fast heavy ion collisions, photon emission processes are caused not only by nuclear reactions or Coulomb excitation but also by interactions from atomic processes. This photon emission induced by reactions between projectile particles (ions) and target electrons can be observed as background radiation in de-excitation γ-ray measurements. Background radiation up to about 200 keV can be can be eliminated by imposing an appropriate energy threshold on the electric circuit. However, summing-up events of several

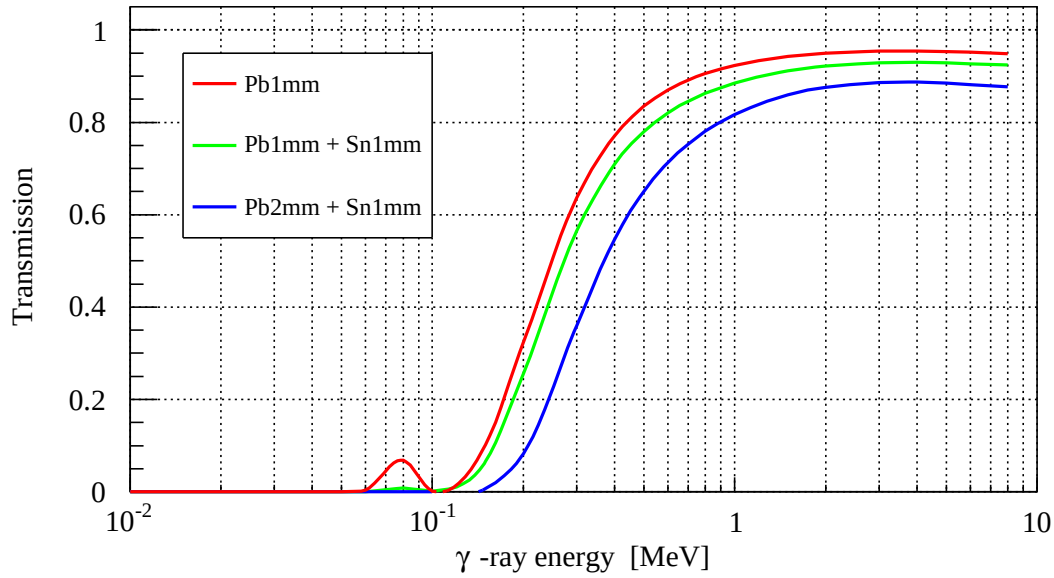

Figure 2.9: Shown is γ-ray transmission as a function of γ-ray energy for three different sets of absorber materials. In the experiment, a shielding of 1 mm-thick Pb was used.

background photons hitting the same detector (pile-up events) can not be eliminated and may cause a worse signal to noise ratio (S/N) in the γ-ray spectrum. Hence background radiations should be reduced by placing the appropriate shielding between reaction target and NaI(Tl) detectors.

A background radiation shielding of Pb with 1 mm thickness was employed as a tube along the beam pipe. Figure 2.9 shows the transmission probability as a function of the γ-ray energy for 1 mm Pb, 1 mm Pb + 1 mm Sn, and 2 mm Pb + 1 mm Sn, respectively, simulated with the GEANT4 framework. For low energies up to about 200 keV, 1 mm Pb has sufficient shielding, while a small bump can be seen around 80 keV. This bump is caused by Pb absorbing the γ ray, releasing a K-shell electron and subsequent electron transition from higher lying shell. By inserting additional Sn shielding, the bump disappears. While little transmission remains at around 80 keV, a Pb shield with 1 mm thickness has a higher transmission in the energy region of interest between a few hundred keV to several MeV. Therefore, atomic background shielding of only 1 mm thick Pb was selected.

The explanation for the origin of the atomic background radiation which expected to be generated in the present experiment is given below.

Radiative Electron Capture

The highly stripped fast heavy ion can capture a free or weakly bound target electron directly into a K-shell vacancy with the subsequent emission of an x-ray photon [42]. This reaction, so called radiative electron capture (REC), has a complex x-ray emission band, which occurs well above the highest characteristic x-ray line for the projectile particle. The energy of the emitted photon is given approximately by the sum of the binding energy of a K-shell electron in a hydrogen-like or helium-like ion and the kinetic energy of an electron which is at rest in the target, relative to the moving ion. The most probable photon energy is otherwise independent of the target material. The cross section of this reaction, $\sigma_{capture}$, is proportional to square of the atomic number of projectile particle and to the atomic number of the target material:

$$\sigma_{capture} \propto Z_p^2 Z_t. \tag{2.1}$$

Here, Z_p and Z_t represents the atomic number of the projectile particle and target, respectively.

Primary Bremsstrahlung

Bremsstrahlung is an x-ray production mechanism in ion-atom collisions. Here the predominant source of bremsstrahlung originates from the electrons of the target and the projectile nucleus. Apart from being captured radiatively into bound states of the projectiles (REC), the target electrons can be scattered into continuum states by the radiation field of the projectile nucleus. The cross section of electron bremsstrahlung resulting from this one-step process, $\sigma_{primary}$, is also proportional to square of the atomic number of projectile particle and to the atomic number of the target material:

$$\sigma_{primary} \propto Z_p^2 Z_t. \tag{2.2}$$

Secondary Electron Bremsstrahlung

Radiation from a two-step process is called secondary electron bremsstrahlung. In the first step, target atoms are ionized via Coulomb excitation. The free electrons produced in this step radiate in the field of another target nucleus. The maximum energy which can be transferred from a projectile with velocity v to a free electron with mass m_e is $2m_e v^2$. For weakly bound electrons, the ionization cross section shows a local maximum at this energy and a rapid decrease of intensity at higher energies. Thus bremsstrahlung

from secondary electrons decreases slowly up to $2m_e v^2$, around 200 keV for the present experiment. The cross section of this reaction, $\sigma_{secondary}$, is proportional to square of the atomic number of projectile particle and to square of the atomic number of the target material:

$$\sigma_{secondary} \propto Z_p^2 Z_t^2. \tag{2.3}$$

Therefore it requires consideration of this background radiation to use the target of high Z material, such as Pb for Coulomb excitation experiment.

2.3.3 The Beam Tracking Detectors at F8

The position of projectile and ejectile particles was measured by three PPACs. Two PPACs were located 1446 mm and 946 mm upstream from the reaction target, and one PPAC was mounted 870 mm downstream. The position measurement allowed for beam tracking in front of the secondary target and scattering angle determination of the ejectiles. This information was also used for particle identification in the ZeroDegree spectrometer.

2.4 The Electric Circuits and Trigger Conditions

In this section, the configuration of electric circuits and the trigger conditions for data acquisition (DAQ) system are explained. The PPACs, plastic scintillators, TEGIC and γ-ray detectors DALI2 were included in the DAQ system. The signal processing for these detectors is explained in Section 2.4.1. The description of trigger conditions applied to the DAQ system is given in Section 2.4.2.

2.4.1 Electric Circuits

Both the timing and the analog signals of all detectors except for the TEGIC were recorded. For the latter, only the pulse height information was obtained. Figure 2.10 shows the electric circuit diagrams of all employed detectors. The analog signals were digitized by using the charge-sensitive or the peak-sensitive analog-to-digital converter modules. Both are denoted as ADC in Figure 2.10. The timing signals were digitized by using the time-to-digital converter modules and are denoted as TDC.

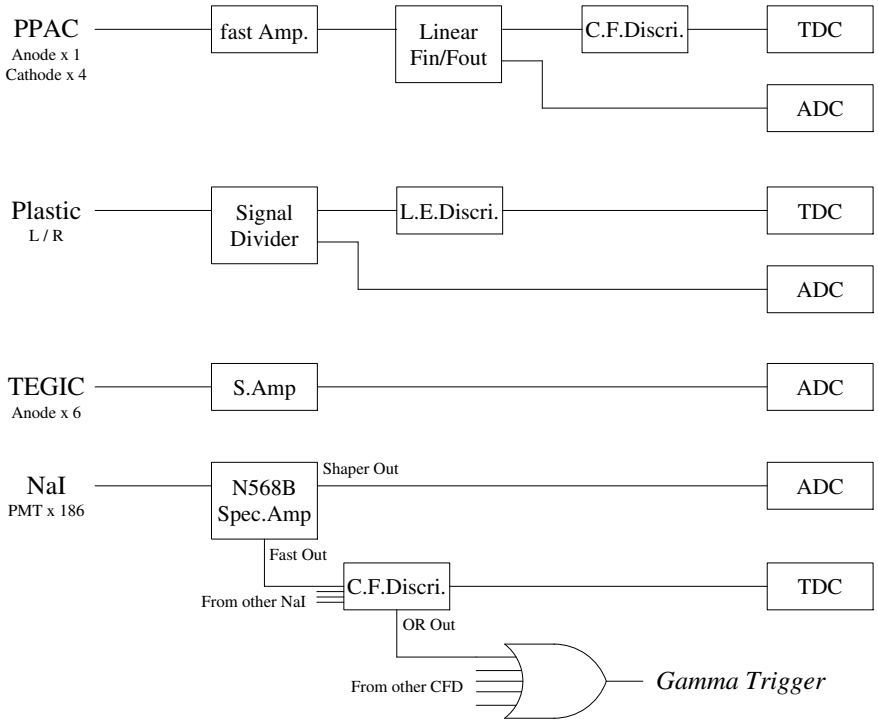

Figure 2.10: Electric circuit diagrams for beam line detectors and NaI(Tl) detectors.

The PPAC Circuit

Each PPAC produced 5 timing- and 5 analog signals as described in Section 2.2.1. All the analog signal produced through pre-amplifier outputs were amplified using fast amplifiers, and then two duplicate analog signals were generated by fan-out circuits of linear fan-in/fan-out modules. One of these two analog signals was directly fed into the charge-sensitive ADC. The other one gave timing information by using a TDC module after being discriminated by a constant fraction discriminator module. The latter is denoted as C.F.Discri. in Figure 2.10. The constant fraction settings of this module were adjusted by using α-emission induced signals from a ^{241}Am source and from background radiation. The delay times of 8 nsec and 5 nsec were adopted to the constant fraction circuit for cathode- and anode signals, respectively, which were around 80 % of rise time of an input signal.

The Plastic Scintillators Circuits

For each plastic scintillator, scintillation photon were detected by two PMTs, one on the left-side and the other one on right. Output signals from the PMTs were split into two analog signals by a signal divider. For timing information, one of two analog signals was discriminated by a leading edge discriminator and then digitized by a TDC module. The another signal was fed into a charge-sensitive ADC.

The TEGIC Circuits

The TEGIC analog signals were amplified by a shaping amplifier with a shaping time of 2 μsec and a gain factor of $\sim$ 30. The bipolar pulse shape outputs were selected and fed into a peak-sensitive ADC. This information corresponded to the energy deposition of ejectile particles in the TEGIC. Timing information was not measured for this detector.

The NaI(Tl) Detector Circuits

The output signals from the anodes of the PMTs connected to the NaI(Tl) scintillation detectors were analysed by employing CAEN N568B Spectroscopy Amplifiers. The modules generated a fast amplifier output (Fast Out) for timing purposes and a shaping amplifier output (Shaper Out) with a programmed gain factor (0.15 to 480) and the selectable shaping time (0.2 μsec to 6 μsec) from an analog input signal. The shaping amplifier was operated with a shaping time of 3 μsec and a gain factor of $\sim$ 64, while fast

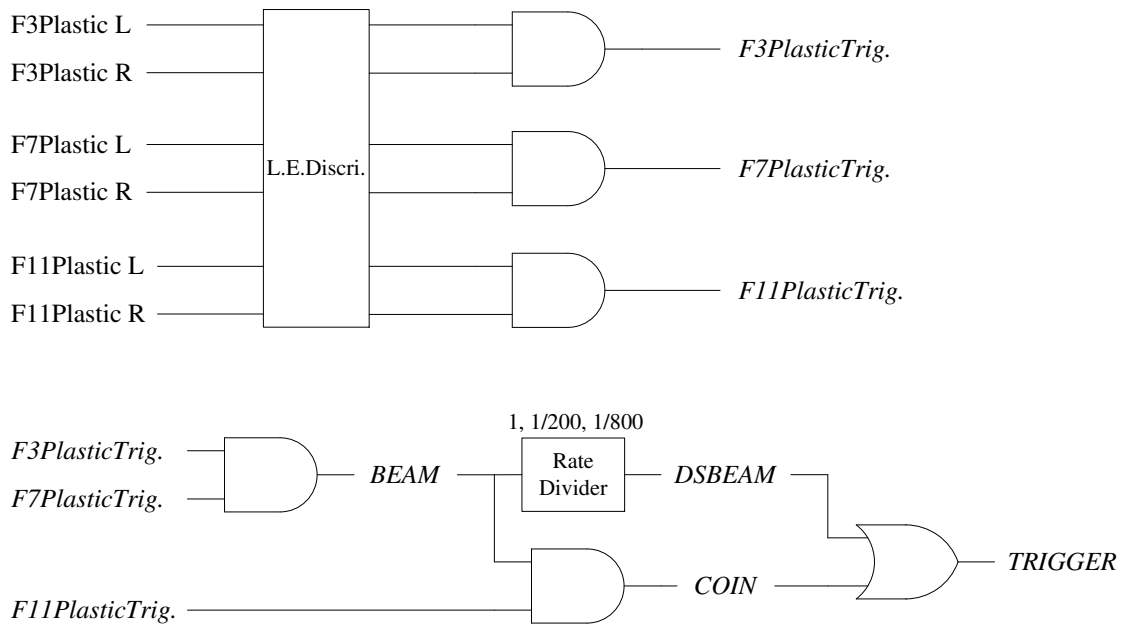

Figure 2.11: Trigger logic diagram. (More explanation here !!!)

amplifier had a fixed gain factor of 20. The fast out signals of the 186 NaI(Tl) detectors were discriminated by using the constant fraction discriminator modules (CAEN V812). A self-trigger, denoted as *Gamma Trigger* in Figure 2.10, was generated through the implementation of the logical OR operation for all the 186 outputs of the C.F.Discri., which was used for measurements of the energy calibration, the efficiency calibration and the background radiation. In a parallel way, each output of the C.F.Discri. was obtained as a timing information by feeding into a TDC module (CAEN V1190) which was operated in a common stop mode. A peak-sensitive ADC module (CAEN V785) was employed to digitize the pulse height of the Shaper Out analog signals from the amplifier, giving the information on the energy deposits of γ rays in the NaI(Tl) scintillator. The threshold of each C.F.Discri. was set to pulse height corresponding to around 200 keV γ-ray.

2.4.2 Trigger Conditions

The trigger logic diagram is shown in Figure 2.11. The main trigger employed was produced from the timing signals of plastic detectors. At first, each plastic trigger was produced through the logical AND operation for both timing signals of the left and the right PMT by using logic coincidence modules. The *BEAM* trigger condition was defined

as the coincidence between $F3PlasticTrig.$ and $F7PlasticTrig.$:

$$BEAM \equiv F3PlasticTrig. \cup F7PlasticTrig.. \tag{2.4}$$

The trigger for the reaction products, denoted as $COIN$, was produced through the logical AND operation of the $BEAM$ and the $F11PlasticTrig.$:

$$COIN \equiv BEAM \cup F11PlasticTrig.. \tag{2.5}$$

Since mainly nucleon removal reactions were measured, the counting rate of reaction products accepted by the ZeroDegree spectrometer was much less than that of beam by the BigRIPS. In order to accumulate data of beam and reaction products effectively, the down scaled $BEAM$ trigger, denoted as $DSBEAM$, with a constant scaling factor of 1/200 or 1/800 was produced and applied to the $TRIGGER$:

$$DSBEAM \equiv 1/200 \; or \; 1/800 \;\; BEAM. \tag{2.6}$$

In the experiment, these two types of triggers, $COIN$ and $DSBEAM$ were used:

$$TRIGGER \equiv COIN \cup DSBEAM. \tag{2.7}$$

Using this $TRIGGER$, the live time of the DAQ system was about 96 %, while the average trigger rate was 300 cps.

2.5 Data Sets and Experimental Parameters

To investigate the excited states of ^{38}Si, ^{40}Si and ^{42}Si, measurements under two different conditions were carried out. The experimental parameters are summarised in Table 2.4.

Secondary Reaction	**C(^{40}S,^{38}Si+γ)**	**C(^{44}S,^{40,42}Si+γ)**
Incident Beam	^{40}S 210 MeV/n	^{44}S 210 MeV/n
Reaction Target	C 2.54 mg/cm^2	C 2.54 mg/cm^2
Ejectile	^{38}Si	^{40,42}Si
Parameters for BigRIPS		
Primary Beam	^{48}Ca 345 MeV/n	^{48}Ca 345 MeV/n
Production Target	15 mm-thick ^{9}Be	15 mm-thick ^{9}Be
$B\rho_{F_0-F_1}$	6.653 Tm	7.226 Tm
$B\rho_{F_1-F_2}$	6.120 Tm	6.680 Tm
Momentum Slit at F1	$\pm$0.1 %	-1 % to 3 %
Energy Degrader at F1	8.05 mm-thick Al	8.05 mm-thick Al
Slit at F2	$\pm$4 mm	$\pm$4 mm
Detector Configuration	F3 : Plastic	
	F5 : Plastic	
	F7 : Plastic	
Parameters for ZeroDegree spectrometer		
Reaction Target at F8	2.54 g/cm^2-thick C	2.54 g/cm^2-thick C
$B\rho_{F_8-F_9}$	4.868 Tm	5.522 Tm
$B\rho_{F_10-F_11}$	4.855 Tm	5.516 Tm
F9, F10 Slit	$\pm$120 mm	$\pm$120 mm
Detector Configuration	F8 : double-PPAC $\times$ 3, Plastic	
	F9 : double-PPAC $\times$ 2	
	F10 : double-PPAC $\times$ 2	
	F11 : double-PPAC $\times$ 2, Plastic, TEGIC	
Others		
Trigger Condition	$COIN \cup DSBEAM(1/800)$	$COIN \cup DSBEAM(1/200)$

Table 2.4: Experimental parameters for the BigRIPS and the ZeroDegree spectrometer. The detector configuration was the same in both data sets.

Chapter 3

Data Analysis

Detailed descriptions of the data analysis procedures are given in this chapter. The beam line detectors and the secondary beams are described in Section 3.1. Analysis procedures for the reaction ejectiles measured with the ZeroDegree spectrometer are explained in Section 3.2.

The analysis procedures for the DALI2 γ-ray detectors are presented in Section 3.3. Here, the energy calibrations, Doppler shift corrections and method for background reduction are explained in detail. Monte Carlo simulations were performed to determine the response function of the γ-ray detectors. Detailed explanations of these simulations are given in Section 3.4. Finally, the systematic errors are evaluated and summarised in Section 3.5.

3.1 Analysis of Secondary Beams

Secondary beam analysis was necessary to identify ^{40}S and ^{44}S fragments within beam cocktails transmitted through the BigRIPS fragment separator. The beam profile and energy at the reaction target position was also determined. These values of the ^{40}S and ^{44}S beams were inserted into Monte Carlo simulations. Also the total number of incident secondary beam particles was determined. This information was extracted from the *DSBEAM* trigger only.

The calibration of the time to digital converters, TDCs, which were used for timing measurements of beam line detectors and DALI2 γ-ray detectors is explained in Section 3.1.1. In Section 3.1.2, the particle identification of the secondary beams is described. The position determination from PPACs and the beam profiles at the reaction target are

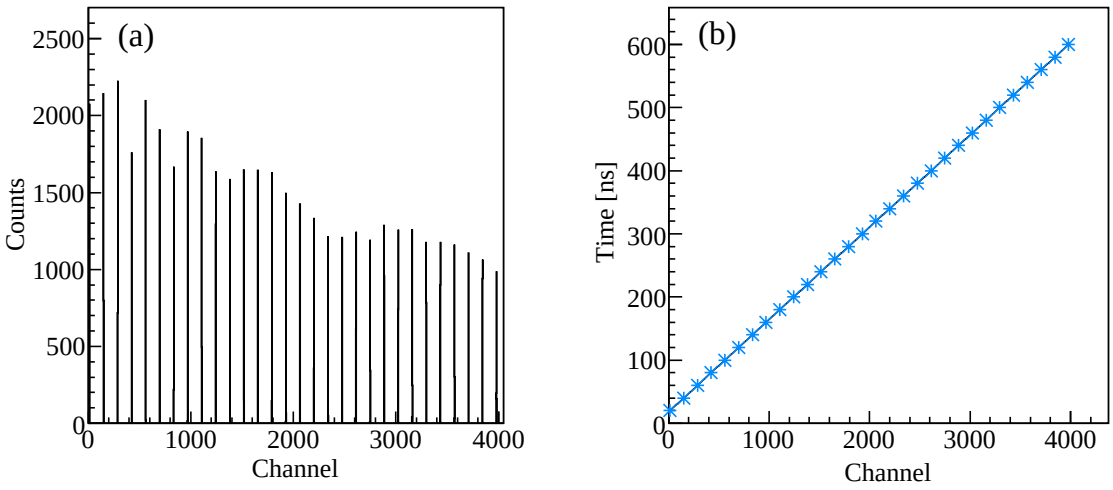

Figure 3.1: Example of a TDC calibration. In the left panel (a), a histogram using the time calibrator module are shown, while the right panel (b) displays the plot of TDC channel versus time. The channel-to-nsec conversion factor was obtained by fitting the plot with a linear function.

presented in Section 3.1.3.

3.1.1 Time Calibration

TDC units were used to deduce the time information from beam line detectors (Plastic Scintillators, PPACs) and DALI2 γ-ray detectors. The time calibration of the TDCs was performed by using a time calibrator module. This module generated a start logic signal followed by a stop logic signal whose time with respect to the start logic signal was altered discretely and periodically with a setup interval. Therefore, a spectrum with a fixed interval was obtained by inserting the start and stop logic signal of the time calibrator into the (common) start and the (common) stop of the TDC modules. Figure 3.1 (a) shows typical histogram obtained for the one PPAC cathode by setting the period to 20 nsec. The channel-to-nsec conversion was performed by plotting the time in nsec against the channel of the TDC, and fitting the plot with a linear function to obtain the conversion factor, as shown in Figure 3.1 (b).

3.1.2 Particle Identification of Secondary Beams

Apart from ^{40}S and ^{44}S, the secondary beams also contained the isotopes ^{39}P and ^{43}P, respectively. The TOF - ΔE - Bρ method was employed to identify secondary beams.

The TOF was deduced from the time differences between the plastic scintillators F5PL and F7PL, TOF(F5-F7), while the integrated charge from the analog signal of the F7PL was used for ΔE information. Both the timing and the integrated charge of the analog signal of the plastic scintillator had a position dependence. The former was due to the fact that the speed of light in the scintillator was almost constant, and thus the time for the light to propagate to the photo-cathode of the PMT depended on the hit position. The latter was due to attenuation of the light generated in the scintillators along the path. Therefore, the horizontal position of the secondary beams at the plastic scintillators could be deduced by reading out the signals of two PMTs installed on the left and the right of each plastic scintillator, respectively. The position independent time, $F5T$, and the horizontal position, $F5X$, of F5PL were then deduced from the following relation:

$$F5T = \frac{F5LT + F5RT}{2}, \tag{3.1}$$

$$F5X = c_0 + c_1 \times (F5LT - F5RT). \tag{3.2}$$

Here, $F5LT$ and $F5RT$ are timings of the left and right PMTs, respectively, the parameters, c_0 and c_1, are the time difference conversion factors for the horizontal position. The position at F7 focal plane can be obtained in the same way from F7PL. The relation between the TOF and the two plastic scintillator times ($F5T$ and $F7T$) is as follows:

$$TOF(F5 - F7) = F7T - F5T + T_{offset}, \tag{3.3}$$

where T_{offset} is the time offset determined experimentally to reproduce the calculated $TOF(F5 - F7)$ values. The integrated charge of the analog signal attenuated exponentially with respect to the path length between hit position and PMT. Therefore, the integrated charge of the F7PL analog signal, $F7Q$, was deduced from the geometric mean value of the left and the right signals:

$$F7Q = \sqrt{F7LQ \times F7RQ}, \tag{3.4}$$

where $F7LQ$ and $F7RQ$ were the integrated charge of the analog signals of the left and right PMT, respectively.

The particle identification of the secondary beam was performed by using F5PL as a TOF and position detector and F7PL as a TOF and ΔE detector. The atomic number Z

and mass-to-charge ratio, A/Q, of the secondary beam were related to TOF, ΔE and Bρ as follows:

$$\Delta E \propto Z^2 \times TOF^2, \tag{3.5}$$

$$A/Q \propto B\rho \times TOF. \tag{3.6}$$

The magnetic rigidity, $B\rho$, of the secondary beam can be expressed by the following approximation:

$$B\rho \simeq B\rho_0 \times (1 + \frac{F5X}{D_{F5}}) \propto F5X. \tag{3.7}$$

In the above expression, $B\rho_0$ is the magnetic rigidity of the central trajectory, which was determined by the magnetic field intensity of the dipole magnets, and D_{F5} is the momentum dispersion at F5 (33 mm/%).

Figure 3.2 shows the particle identification for ^{40}S. The correlation between TOF(F5-F7) and F7Q, shown in Figure 3.2 (a), corresponds to TOF - ΔE, while the correlation between TOF(F5-F7) and F5X, shown in Figure 3.2 (b), corresponds to TOF - Bρ. ^{40}S was selected by applying the two gates indicated by dashed lines in Figure 3.2. The purity of ^{40}S was estimated to be 97 % at an intensity of about 70 kcps. The same analysis was performed for the ^{44}S secondary beam data set as shown in Figure 3.3. The purity and counting rate of ^{44}S was about 85 % and 40 kcps, respectively.

3.1.3 Beam Profile at the Reaction Target

At the reaction target, the incident secondary beams were tracked by two double-PPACs. The ejectiles were tracked using a double-PPAC placed downstream of the reaction target.

PPAC Position Determination

The beam hit positions on the PPACs were deduced from the signal time differences, denoted by $Tx1(Ty1)$ and $Tx2(Ty2)$, between the two ends of the cathodes:

$$X = C_x \times (Tx1 - Tx2 + Toff_{X:Line}) + Xoff_{Intrinsic} + Xoff_{Align}, \tag{3.8}$$

$$Y = C_y \times (Ty1 - Ty2 + Toff_{Y:Line}) + Yoff_{Intrinsic} + Yoff_{Align}. \tag{3.9}$$

In the above equations, C_x and C_y are the slope factors for the delay-lines (typically about 1.2 mm/nsec), $Toff_{X:Line}$ and $Toff_{Y:Line}$ are the intrinsic offsets due to the electronics system, $Xoff_{Intrinsic}$ and $Yoff_{Intrinsic}$ are the offsets due to the delay-line, while

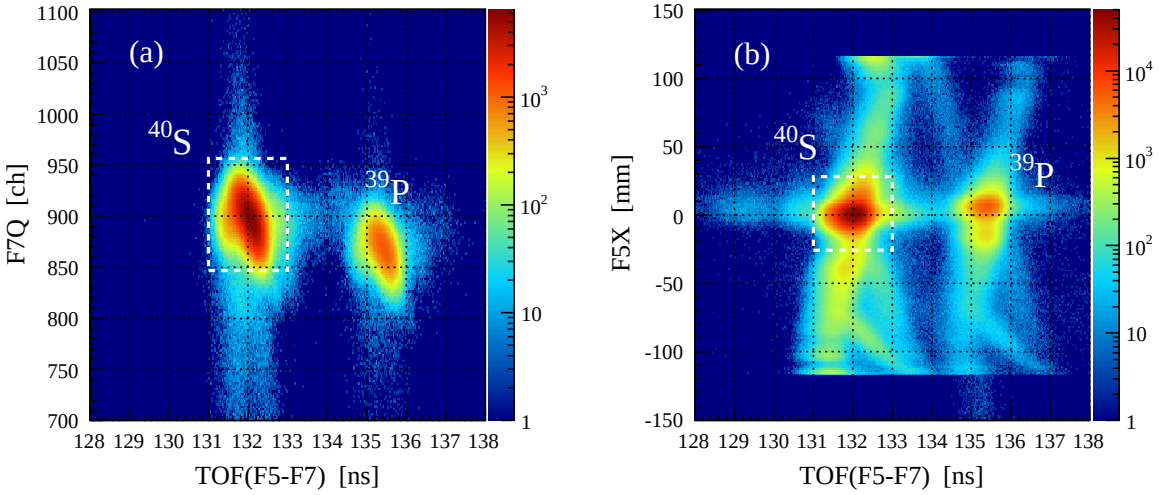

Figure 3.2: Particle identification plot of the secondary beams for ^{40}S setting. The left panel (a) shows the TOF(F5-F7) versus F7Q plot with a TOF-ΔE gate (dashed line), while the right panel (b) shows the TOF(F5-F7) versus F5X plot with a TOF-Bρ gate (dashed line).

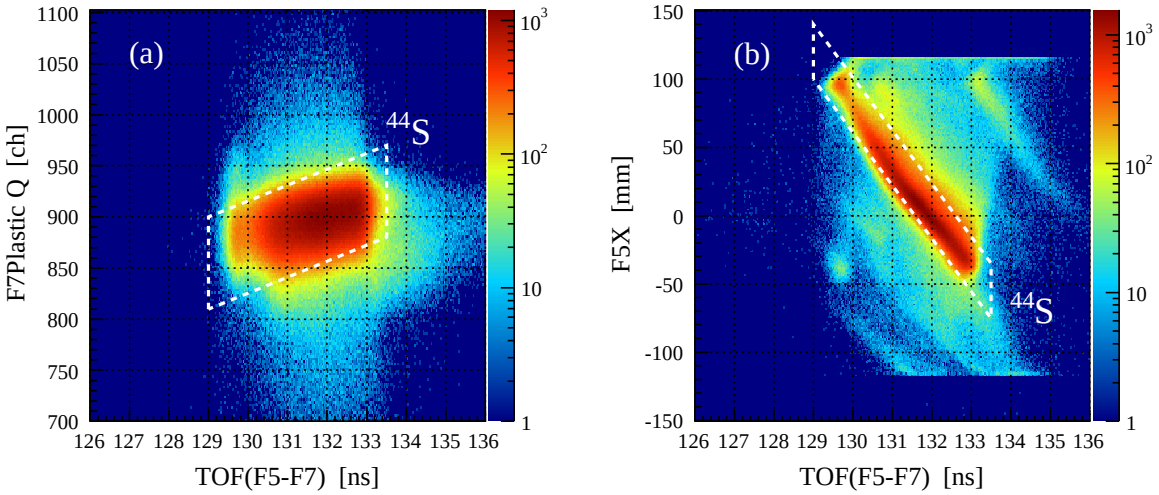

Figure 3.3: Particle identification plot of the secondary beams for ^{44}S setting. The left panel (a) shows the TOF(F5-F7) versus F7Q plot with a TOF-ΔE gate (dashed line), while the right panel (b) shows the TOF(F5-F7) versus F5X plot with a TOF-Bρ gate (dashed line).

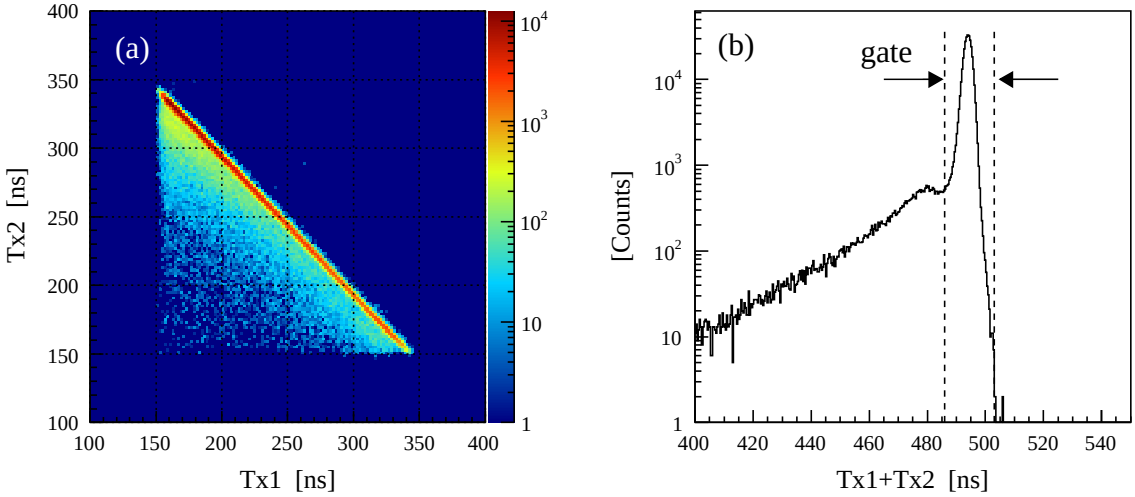

Figure 3.4: Example analysis for a PPAC. The left panel (a) shows the correlation between $Tx1$ and $Tx2$ while the right pannel (b) shows the $T_{sum}(= Tx1 + Tx2)$ spectrum with a T_{sum} gate (dashed line).

$Xoff_{Align}$ and $Yoff_{Align}$ are the offsets due to the geometrical alignment relative to the beam axis. Both of the slope factors and the intrinsic offsets are characteristics of each delay-line and are known parameters. The offsets due to the electronics system were determined by sending two simultaneous pulser signals through circuit to the respective TDC channels, and deducing the timing differences. The geometrical offsets due to the alignment were measured by a theodolite.

Elimination of Pile-up and δ-ray Events

As previously described, each PPAC had two cathodes, which had a strip structure connected to a delay line. The PPAC signals were read out at both ends of the delay line. Thus, if the one particle hit the PPAC, $Tx1$ and $Tx2$ should had a correlation for which the sum of the two ($T_{sum} = Tx1 + Tx2$) was constant. Figure 3.4 (a) shows a typical histogram of the correlation of $Tx1$ and $Tx2$, while Figure 3.4 (b) shows the T_{sum} spectrum, where a sharp constant component and a tail component can be seen. This tail component was due to the multi hit events on the PPAC and δ-rays which originated from the reactions between the secondary beams and electrodes or gas. In order to select the correct events, the T_{sum} gate, as shown in Figure 3.4 (b), was imposed on each PPAC.

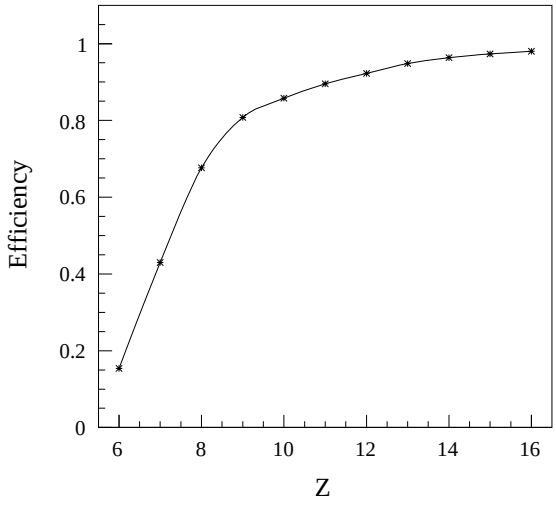

Figure 3.5: Tracking efficiency using two double-PPACs located at F9 as a function of Z. A value of 96.38 % was deduced for Si(Z=14) isotopes.

Trajectory Tracking Method and Efficiency

For the trajectory tracking, at least one position signal for every double-PPACs was required, because the distance between the two cathodes in a double-PPAC unit was too short, $\sim$ 4 cm, to obtain sufficient angular resolution.

In general, the detection efficiency of a gas detector, such as a PPAC, depends on the atomic number, Z, of the incident beam and the supplied high voltage for the ionization amplification. Then the tracking efficiency, $\varepsilon_{Tracking}$, can be defined as

$$\varepsilon_{Tracking} = \frac{n(Tracking \cap Z)}{n(Z)}. \tag{3.10}$$

In above expression, $n(Tracking \cap Z)$ represents the number of simultaneous events in both the tracking and the Z determination, while the $n(Z)$ represents the number of events obtained in Z spectrum. Using this equation, the tracking efficiency of the F9PPACs as a function of Z was extracted, as shown in Figure 3.5. A tracking efficiency of 96.38 % was obtained for Si(Z=14) isotopes. The Z determination method is explained in Section 3.2.1.

Position and Emittance of Incident Beam on Target

The X and Y positions on the reaction target were obtained by extrapolating the hit positions at the F8PPACs.

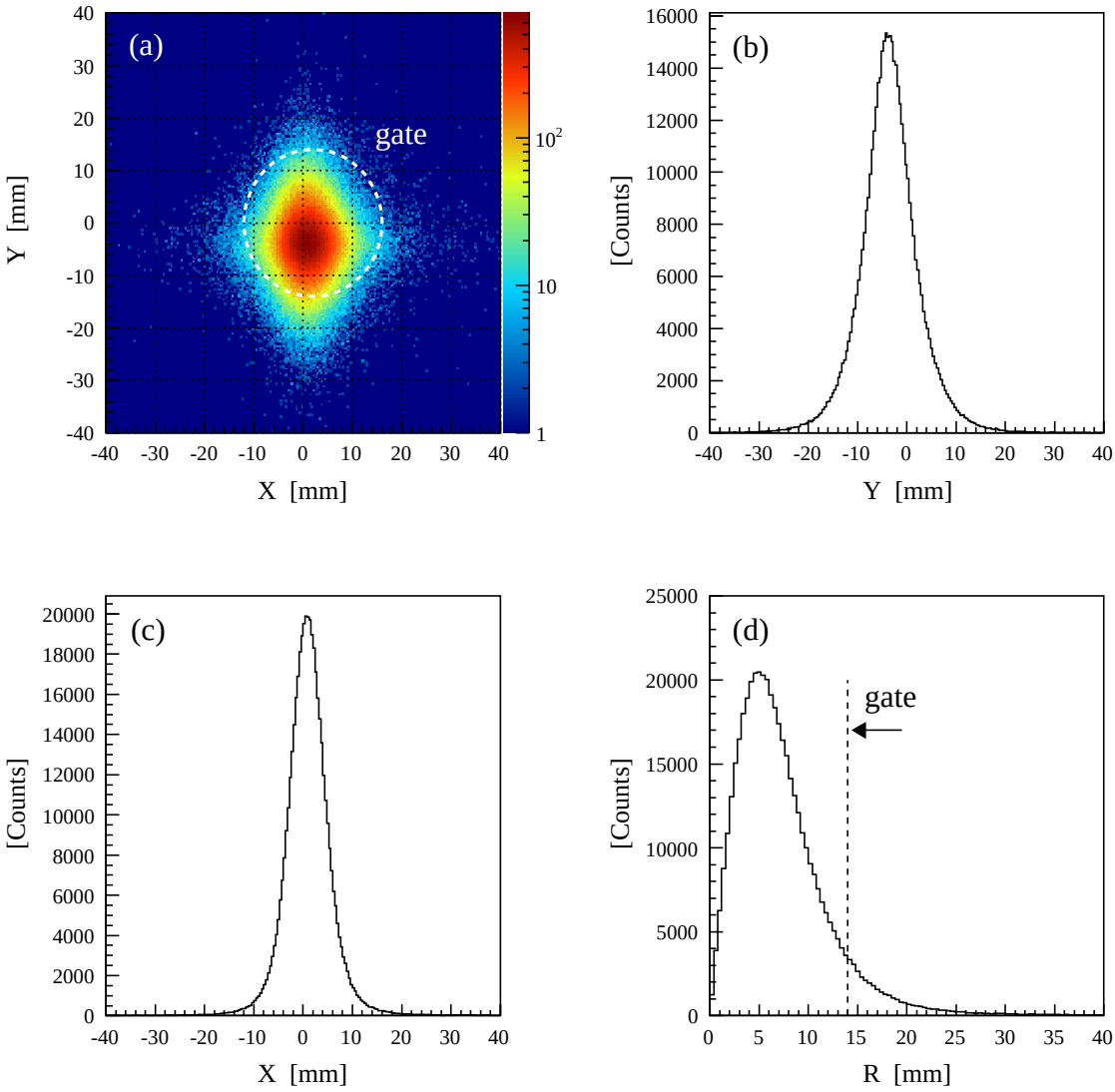

Figure 3.6: Panel (a) shows the position of the secondary ^{44}S beam on the reaction target seen from downstream. The dashed circle line indicates the applied gate on the reaction target position. While panel (b) and (c) show the projected distributions in the Y- and X-direction, respectively. The radial distance from the reaction target center is shown in panel (d) with the applied gate.

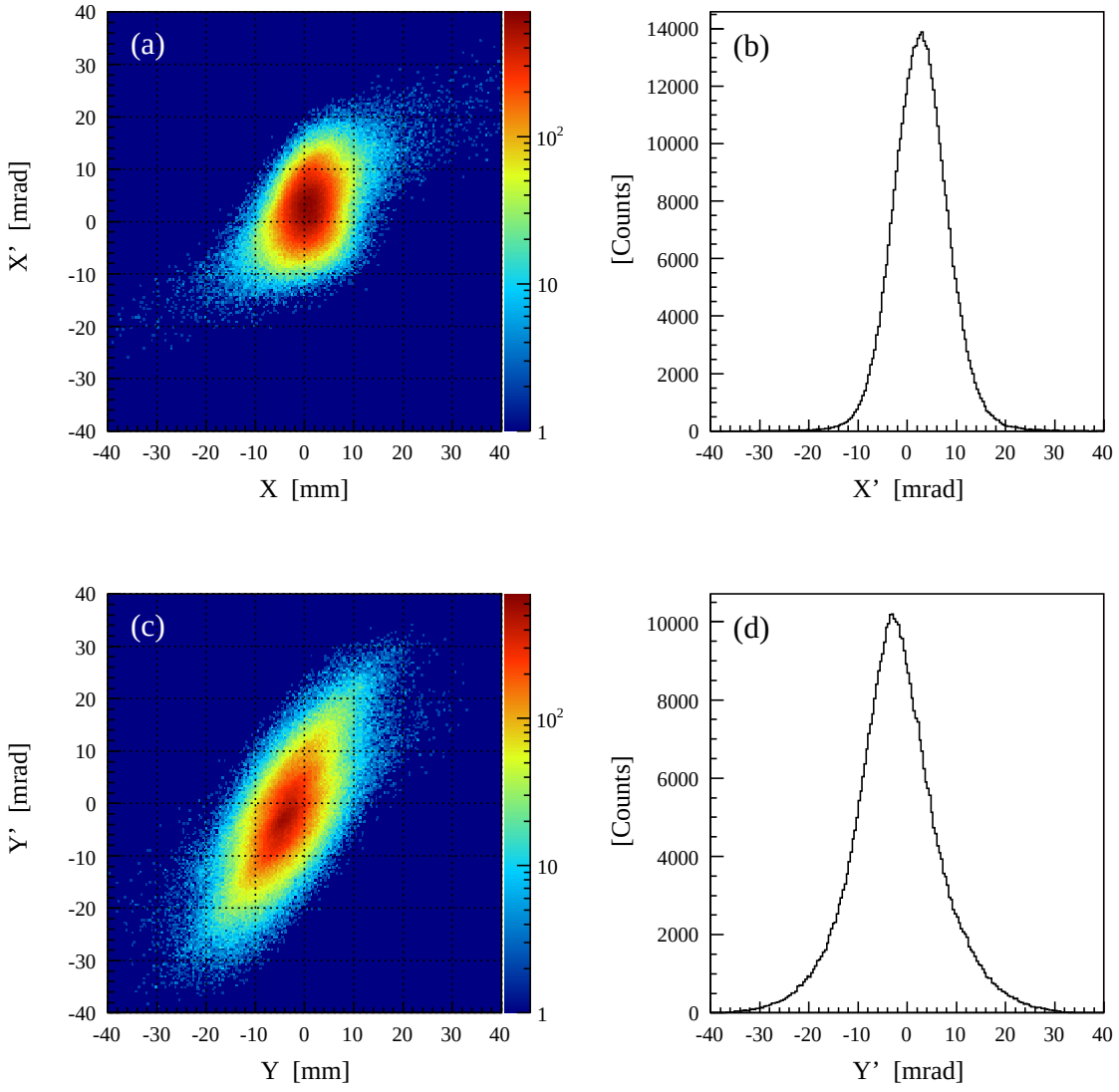

Figure 3.7: Emittance of the ^{44}S secondary beam in the X- and Y-direction. Their projected plane angular distributions are shown in panel (b) and (d), respectively.

Figure 3.6 (a) shows the image of the ^{44}S secondary beam on the reaction target. The X and Y position distributions are shown in Figure 3.6 (b) and Figure 3.6 (c), respectively, while the distance distribution, denoted as R, from the center of the reaction target is shown in Figure 3.6 (d). The center of the incident beam was about 1 mm to left and 4 mm below the center of the reaction target, which located 2 mm to right and 0 mm below the beam axis. The beam positions contained uncertainties inherited from the position resolutions of the PPACs. Assuming an intrinsic position resolution of 0.5 mm for each PPAC, the uncertainty of the beam positions on the reaction target was calculated to be about 2 mm. Taking into account this uncertainty, the beam spot size for the ^{44}S fragment was estimated to be 3 mm (r.m.s) in the X and 4 mm (r.m.s) in the Y dimension. This spot size was small compared to the 30 mm diameter of the reaction target. The distance from the center of the reaction target was restricted to within 14 mm, as indicated in Figure 3.6 (a) and (d), in order to ensure that the ^{44}S fragments hit only the reaction target. With this gate, 90 % of the ^{44}S beam was selected.

Figure 3.7 shows the emittance of the incident beam at the reaction target position. The X' and Y' distributions are shown in Figure 3.7 (b) and (d), respectively. Assuming Gaussian distributions and taking into account the intrinsic resolution of the PPACs, the angular broadenings of the ^{44}S beam were determined to be 5 mrad (r.m.s) and 8 mrad (r.m.s) in the X' and Y' dimensions, respectively.

3.2 Analysis of Ejectiles

The ejectiles produced by the secondary reaction between the projectile particle and the reaction target were selected and identified with the ZeroDegree Spectrometer, which followed the BigRIPS. The total number of the produced ^{38}Si,^{40}Si and ^{42}Si fragments were determined with the ZeroDegree Spectrometer using the $COIN$-triggered data only. The identification of the atomic number, Z, is explained in Section 3.2.1. In Section 3.2.2, the method of the reconstruction of the magnetic rigidity, Bρ, which was necessary to deduce the mass to charge ratio, A/Q, is described. The particle identification plots for the ZeroDegree Spectrometer are shown in Section 3.2.3.

3.2.1 Z Identification

The relation between the energy deposited in the Ion Chamber located at F11 and the TOF between the reaction target and the plastic scintillator located at F11 (TOF-ΔE

method) was used for the identification of the atomic number Z. The energy deposited by a charged particle passing through a unit length of the P10 gas, the stopping power, is given by the Bethe-Bloch formula:

$$-\frac{dE}{dx} \simeq \frac{4\pi e^4 z^2}{m_e v^2} NZ \left[\ln(\frac{2m_e v^2}{I}) - \ln(1 - \frac{v^2}{c^2}) - \frac{v^2}{c^2} \right]. \tag{3.11}$$

In the above expression, v and z are the velocity and atomic number of the ejectile, N and Z are the number of density and atomic number of the P10 gas (90%Ar+10%CH4), e and m_e are the charge and rest mass of the electron, and I is the average excitation and ionization potential of the P10 gas, typically around 210 eV. An approximation gives

$$-\frac{dE}{dx} \propto \frac{z^2}{v^2} \times c. \tag{3.12}$$

The TOF of the ejectiles between the reaction target and the plastic scintillator located at F11 is related to their velocities:

$$TOF \propto v^{-1}. \tag{3.13}$$

Combining the above relations, we obtain

$$\Delta E \propto Z^2 TOF^2. \tag{3.14}$$

With this relation, the ejectiles with different Z can be separated by plotting the ΔE against the TOF.

Figure 3.8 (a) shows a 2-dimensional plot of the energy deposited in the Ion Chamber and the TOF between the reaction target and the plastic scintillator located at F11, where the relation between the energy loss and the TOF can be seen. The distribution of the energy deposited in the Ion Chamber is shown in Figure 3.8 (b). Figure 3.8 (c) shows a 2-dimensional plot of atomic number, Z, deduced by using the relation of Equation 3.14 and the TOF, while the distribution of the atomic number, Z, is shown in Figure 3.8 (d) with a gate applied for Si (Z=14) isotopes. The resolution of the atomic number, ΔZ/Z, for Si (Z=14) isotopes was deduced to 0.9 % (r.m.s).

3.2.2 Reconstruction of Magnetic Rigidity Values

The magnetic rigidity $B\rho$ of a secondary beam particle is proportional to its momentum P:

$$B\rho = \frac{P}{Qe}. \tag{3.15}$$

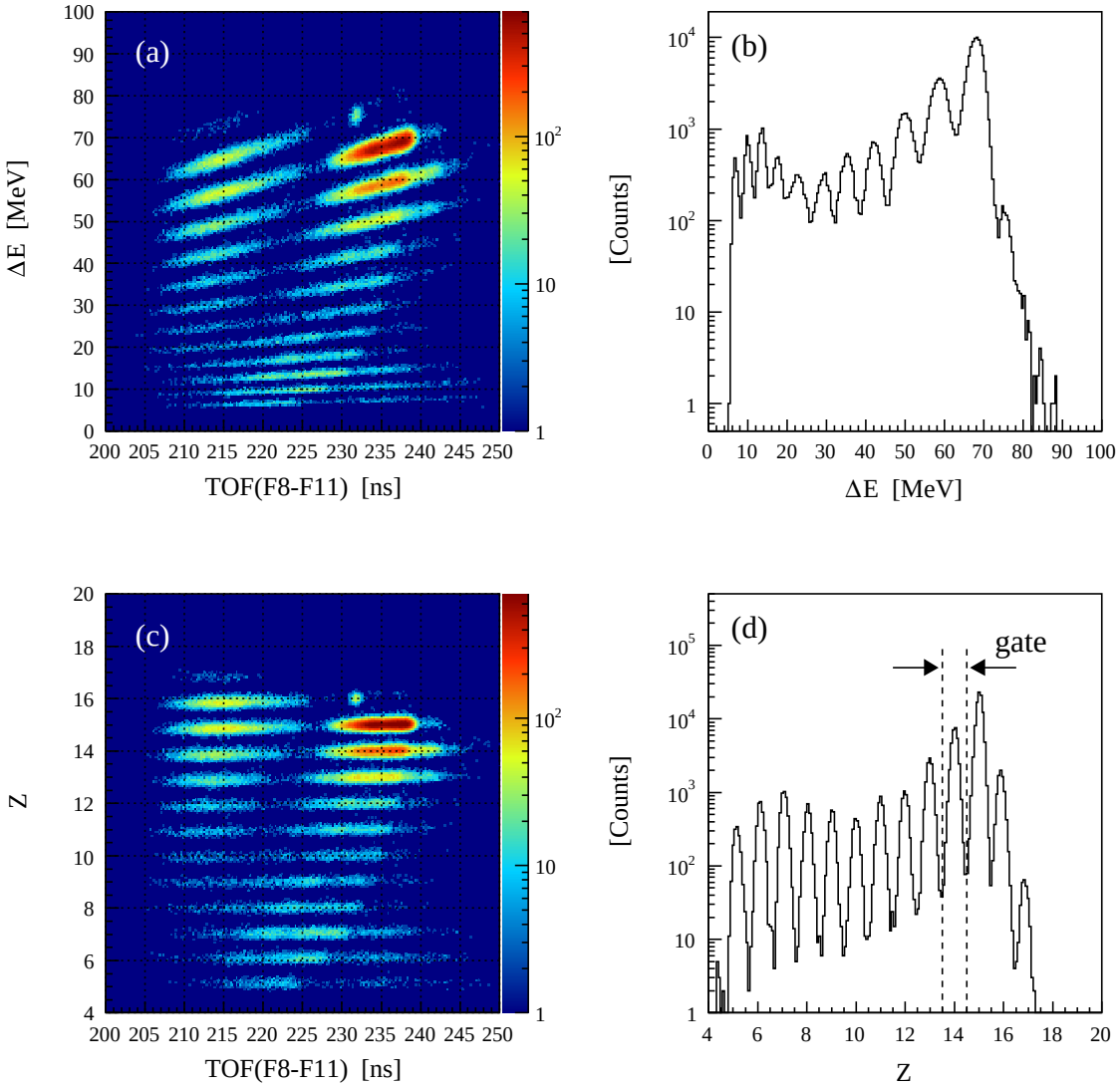

Figure 3.8: Determination of the atomic number Z. Panel (a) shows the correlation between TOF(F8-F11) and ΔE of the Ion Chamber located at F11. The one dimensional ΔE-distribution of the Ion Chamber is shown in panel (b). Panel (c) shows the correlation between TOF(F8-F11) and the atomic number Z deduced by using the Bethe-Bloch formula. The Z-distribution is shown in panel (d) with the applied gate for Si isotopes (13.5<Z<14.5).

Element		Element	
$(x\|x)$	-2.00	$(y\|y)$	-2.11
$(x\|a)$	-0.06 [mm/mrad]	$(y\|b)$	0.18 [mm/mrad]
$(x\|\delta)$	-24.83 [mm/%]		
$(a\|x)$	0.25 [mrad/mm]	$(b\|y)$	-0.02 [mrad/mm]
$(a\|a)$	-0.49	$(b\|b)$	-0.47
$(a\|\delta)$	0.01 [mm/%]		

Table 3.1: The elements of beam transfer matrix between F8 and F9 focal plane.

In the above expression, Qe represents the charge of the secondary beam particle. In the ZeroDegree spectrometer, the magnetic rigidity $B\rho$ can be measured as the relative difference δ with respect to the magnetic rigidity $B\rho_0$ of the central trajectory which can be obtained from the magnetic field intensity of a dipole magnet:

$$B\rho = B\rho_0(1+\delta). \tag{3.16}$$

The relative difference of the magnetic rigidity can be deduced by using beam transportation matrix between two focal planes. In the ZeroDegree spectrometer, the beam phase space at the momentum dispersive focal plane F9 is represented by the beam transportation matrix times the beam phase space at the achromatic focal plane F8:

$$\begin{pmatrix} F9X \\ F9A \\ F9Y \\ F9B \\ \delta \end{pmatrix} = \begin{pmatrix} (x|x) & (x|a) & 0 & 0 & (x|\delta) \\ (a|x) & (a|a) & 0 & 0 & (a|\delta) \\ 0 & 0 & (y|y) & (y|b) & 0 \\ 0 & 0 & (b|y) & (b|b) & 0 \\ 0 & 0 & 0 & 0 & 1 \end{pmatrix} \begin{pmatrix} F8X \\ F8A \\ F8Y \\ F8B \\ \delta \end{pmatrix}. \tag{3.17}$$

Solving this equation, the relative difference of the magnetic rigidity δ is obtained:

$$\delta = \frac{(a|a)F9X - (x|a)F9A - F8X}{(a|a)(x|\delta) - (x|a)(a|\delta)}. \tag{3.18}$$

The beam transportation matrix elements are deduced by the ion optics simulation code COSY INFINITY based on the measured magnetic field map. Table 3.1 shows the values between the F8 and F9 focal plane.

3.2.3 Particle Identification of Ejectiles

Many nuclei produced by reactions of the secondary beams inside the reaction target were accepted by the ZeroDegree spectrometer. The ΔE - TOF - $B\rho$ method was employed in order to identify ^{38}Si, ^{40}Si and ^{42}Si from the other accepted reaction products. The atomic number Z was deduced by measuring TOF and ΔE as described in Section 3.2.1. In addition, the mass to charge ratio A/Q was deduced by transforming Equation (3.15) into

$$\frac{A}{Q} = \frac{B\rho}{\beta\gamma}\frac{e}{m_0 c}. \tag{3.19}$$

Here, m_0 represents the atomic mass unit (931.49 MeV), while β and γ represent the beam velocity and the Lorentz factor, respectively. The velocity of reaction products was measured by the two thin plastic scintillators installed at F8 just before the reaction target and F11 at the final focal plane of the ZeroDegree spectrometer, respectively.

Figure 3.9 (a) shows the particle identification plot of the reaction products between the ^{40}S beam and the reaction target C. The ^{38}Si fragments, denoted by a dashed frame, are clearly separated from the other reaction products. The 1 - dimensional A/Q distribution of the produced Si(Z=14) isotopes is shown in Figure 3.9 (b). The absolute A/Q resolution in r.m.s, $\sigma_{A/Q}$ was 6.5×10^{-3}, sufficient to separate different isotopes. For the nucleus ^{38}Si, the required peak separation from the isotope ^{37}Si was 7.1×10^{-2}, corresponding to $11\sigma_{A/Q}$. A gate was imposed on the A/Q ($2.679 < A/Q < 2.750$) for ^{38}Si fragments, as shown by the dashed lines in Figure 3.9 (b). Similar analysis was performed on ^{40}Si and ^{42}Si, as shown in Figure 3.10. Two A/Q gates ($2.821<A/Q<2.893$ and $2.964<A/Q<3.036$), denoted by the dashed lines in Figure 3.10 (b), were imposed for these two fragments. The contributions from the neighboring isotopes to the imposed gates were negligible small, $< 0.001\%$ in every case.

3.3 Analysis of De-excitation γ-rays

The NaI(Tl) scintillation detector array DALI2 was used to measure the de-excitation γ-rays. Though DALI2 consisted of 186 NaI(Tl) detectors, 71 NaI(Tl) detectors were excluded in the analysis due to their bad intrinsic resolution and signal-to-noise (S/N) ratio. Only results from the analysis on the other 115 NaI(Tl) detectors are described in the following.

The energy calibration and resolution survey for each NaI(Tl) detector was carried out

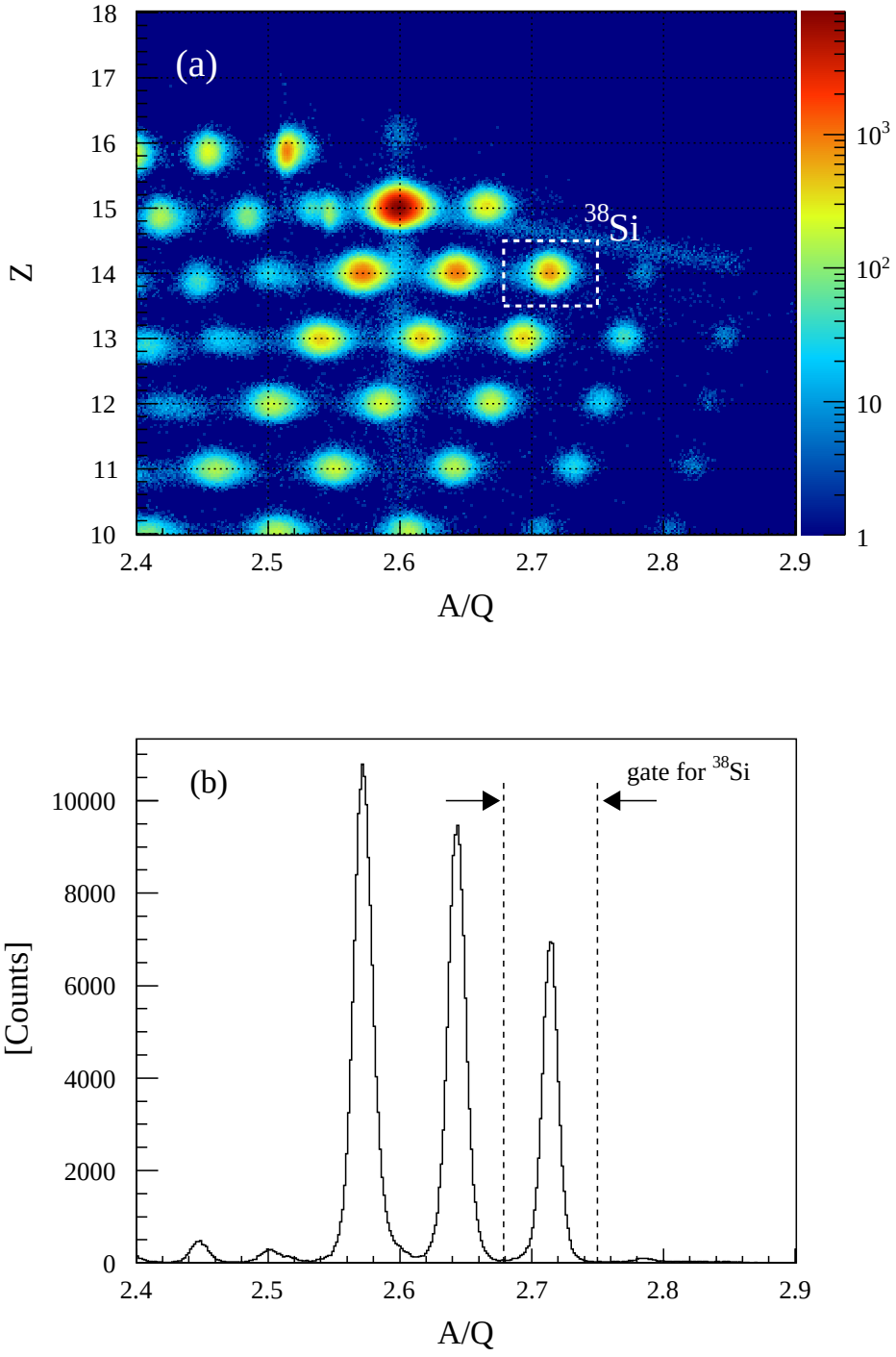

Figure 3.9: The A/Q versus Z particle identification plot of the reaction fragments between the ^{40}S secondary beam and the reaction target C is shown in panel (a). The ^{38}Si fragments (A/Q=2.72, Z=14, dashed line) were clearly separated from other isotopes. Panel (b) shows the A/Q distribution of Si(Z=14) isotopes with the imposed gate (dashed lines and arrows) for ^{38}Si.

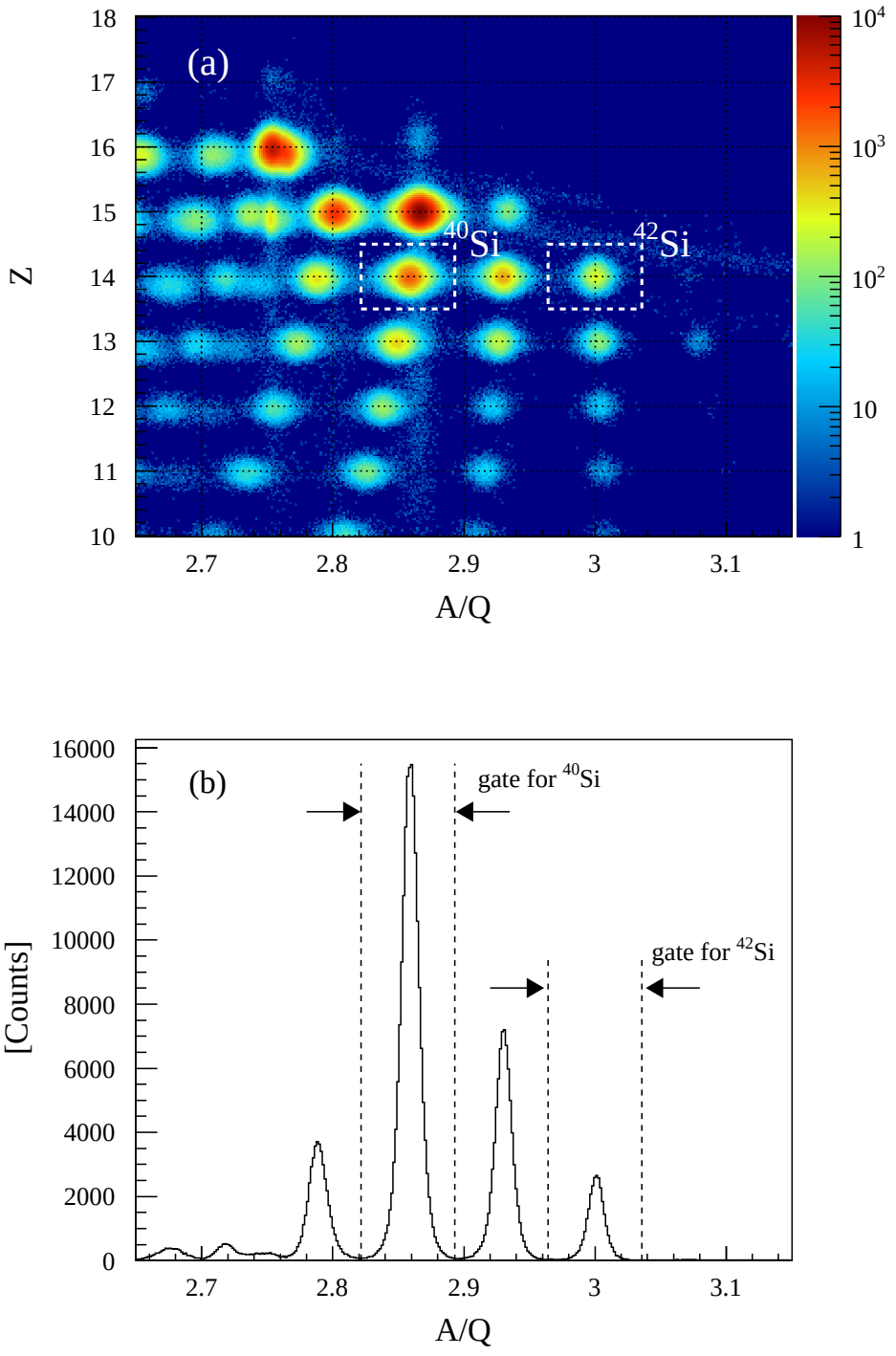

Figure 3.10: The A/Q versus Z particle identification plot of the reaction fragments between the ^{44}S secondary beam and the reaction target C is shown in panel (a). The ^{40,42}Si fragments, indicated by the dashed line, were clearly separated from other isotopes. Panel (b) shows the A/Q distribution of Si(Z=14) isotopes with the imposed gate (dashed lines and arrows) for ^{40,42}Si.

using standard γ-ray reference sources of ^{60}Co, ^{137}Cs and ^{88}Y. The analysis procedures and results are explained in Section 3.3.1. For in-beam γ-ray spectroscopy experiment based on the inverse kinematics, the γ-rays are emitted in-flight from the fast moving nuclei. Therefore, γ-rays detected in the laboratory system are subject to the Doppler-shift. In Section 3.3.2, the Doppler-shift correction is described. The NaI(Tl) detectors are sensitive not only to the γ-rays emitted from the ejectiles, but also to the charged particles, neutrons and γ-rays generated from the reaction target and other materials. A description on how to reduce such background events is given in Section 3.3.3.

3.3.1 Energy Calibration of NaI(Tl) Detectors

The energy calibration of the NaI(Tl) detectors was performed using three standard γ-ray sources: ^{137}Cs (662 keV), ^{60}Co (1173 keV and 1332 keV) and ^{88}Y (898 keV and 1836 keV). An example of the correspondence between channels of the ADC module for one of the NaI detectors and the reference values of the standard γ-ray energies is given in Figure 3.11 (a). The channel-to-keV conversion factors and offset parameters were determined by fitting the energies with a linear function for all the NaI(Tl) detectors individually.

Systematic errors due to the uncertainty in the energy calibration were determined by comparing the summed energy spectra of all the NaI(Tl) detectors with the reference energies of the standard sources. The deviations of the observed full-energy-peak positions from the reference energies of the standard sources are listed in Table 3.2. The calibration function could reproduce all γ-ray energies well within a few keV. The greatest deviation observed with the ^{60}Co γ-ray source, 3 keV for the 1332.49 keV γ-rays was adopted as systematic error due to the energy calibration.

The statistical uncertainty in the detected number of the scintillation-photons by a photo-multiplier is the main factor contributing to the energy resolution of a NaI(Tl) detector. Since the number of photons generated in a NaI(Tl) scintillator is roughly proportional to the energy of the incident γ-ray, E_γ, with an uncertainty of $\sqrt{E_\gamma}$, the intrinsic energy resolution should have a $\sqrt{E_\gamma}$ dependence. A power function of E_γ was used to evaluate the intrinsic energy resolution, assuming that other contributions also have the energy dependences:

$$\Delta E_\gamma = k_1 \times E_\gamma^{k_2}. \tag{3.20}$$

As the intrinsic energy resolution is different for every NaI(Tl) detector, $k_1 = 1 - 2$ and $k_2 = 0.5 - 0.6$ were obtained individually from fitting and then used as input parameters

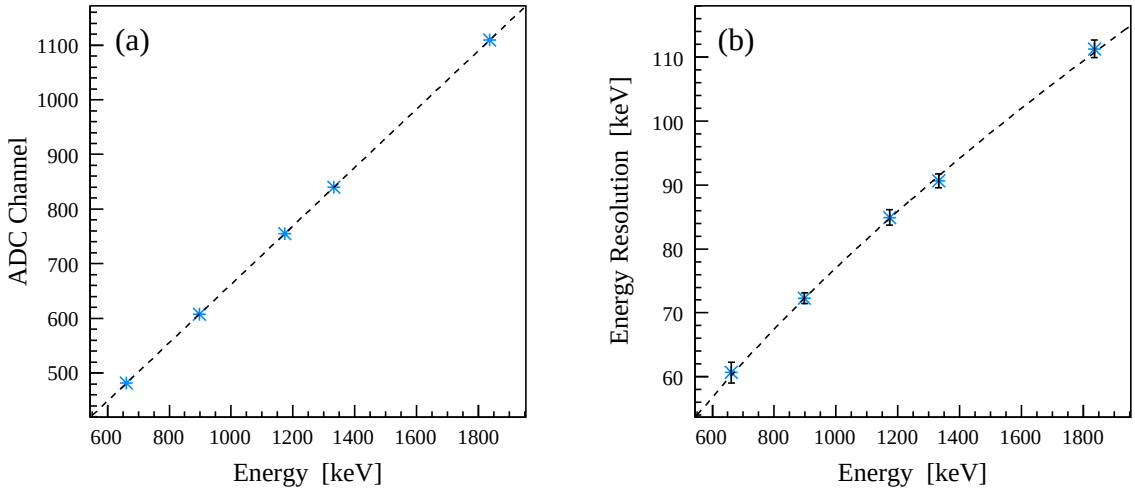

Figure 3.11: Example of energy calibration and evaluation of the intrinsic energy resolution. In panel (a), peak position obtained in ADC channels for one of the NaI(Tl) detectors is plotted against the reference energies of the standard γ-ray sources. The dashed line indicate the linear fit function. In panel (b), γ-ray source energies are plotted against the full-energy-peak resolution (FWHM) of a single NaI(Tl) detector. The intrinsic energy resolution as a function of γ-ray energy was evaluated by fitting the points with a power function (dashed curve).

γ Source	Energy [keV]	Calibrated Energy [keV]	Deviations [keV]
^{137}Cs	661.66	659.9	-1.8
^{60}Co	1173.23	1171.7	-1.5
	1332.49	1329.5	-3.0
^{88}Y	898.04	899.5	+1.5
	1836.06	1837.2	+1.1

Table 3.2: Deviations of the calibrated energies for the entire DALI2 spectrometer from the reference energies of the standard γ-ray sources.

for Monte Carlo Simulations (explained in Section 3.4). A full-energy peak in an observed spectrum is attributing to photo-electric absorption, electron pair production, and also Compton scattering. A NaI(Tl) scintillator, in general, has non-linear response to low energy electrons induced by Compton scattering and in photo-electric absorption of low energy γ-rays or X-rays [43], which is considered to be the reason of the deviation from $k_2 = 0.5$ ($\sqrt{E_\gamma}$). An example of the energy resolution (FWHM) measured with the three standard γ-ray sources as a function of the γ-ray energy is shown in Figure 3.11 (b).

3.3.2 Doppler Shift Correction

The γ-rays were detected in-flight from moving reaction products with relativistic velocities around $\beta \sim 0.55$. Hence, observed γ-rays in the laboratory frame needed to be corrected for the Doppler-shift into the rest frame of the fast moving projectile nuclei. For a proper Doppler-shift correction, it is necessary to know the fragment's velocity and the γ-ray emission angle. The relation between γ-ray energy in the projectile frame E_γ^{proj} and measured energy in the laboratory frame is given by

$$E_\gamma^{proj} = \gamma_v \left(1 - \beta \cos\theta_\gamma^{lab}\right) E_\gamma^{lab}, \tag{3.21}$$

where θ_γ^{lab} is the polar angle between fragments and the γ-ray, and γ_v represents the Lorentz factor $\gamma = 1/\sqrt{1-\beta^2}$. The angular distribution of the fragments was small ($<$ 1 degree relative to the beam axis). Therefore, the polar angles of the γ-ray detector positions were used as θ_γ^{lab} for the Doppler-shift correction. The polar angles were determined accurately by Monte Carlo Simulations (explained in Section 3.4) for every NaI(Tl) detectors.

Figure 3.12 (a) shows the γ-ray energy spectrum detected in coincidence with C(^{44}S,^{40}Si) reaction versus the ID numbers of the NaI(Tl) detectors, while the Doppler-shift corrected γ-ray energy spectrum is shown in Figure 3.12 (b). Here, a dense distribution at 985 keV is observed, which corresponds to the known $2_1^+ \rightarrow 0_{g.s.}^+$ transition of 986 keV. The ID numbers of the NaI(Tl) detectors were assigned in ascending order according to decreasing polar angle θ_γ^{lab}. After applying the Doppler-shift correction, it is clearly visible that the observed γ-ray energies are shifted to the proper transition energy for all NaI(Tl) detectors and thus for all θ_γ^{lab} angle. The overall energy resolution after applying the Doppler-shift correction was about 11.5 % (FWHM) for the 985 keV γ-ray transition, which was in agreements with the Monte Carlo Simulations.

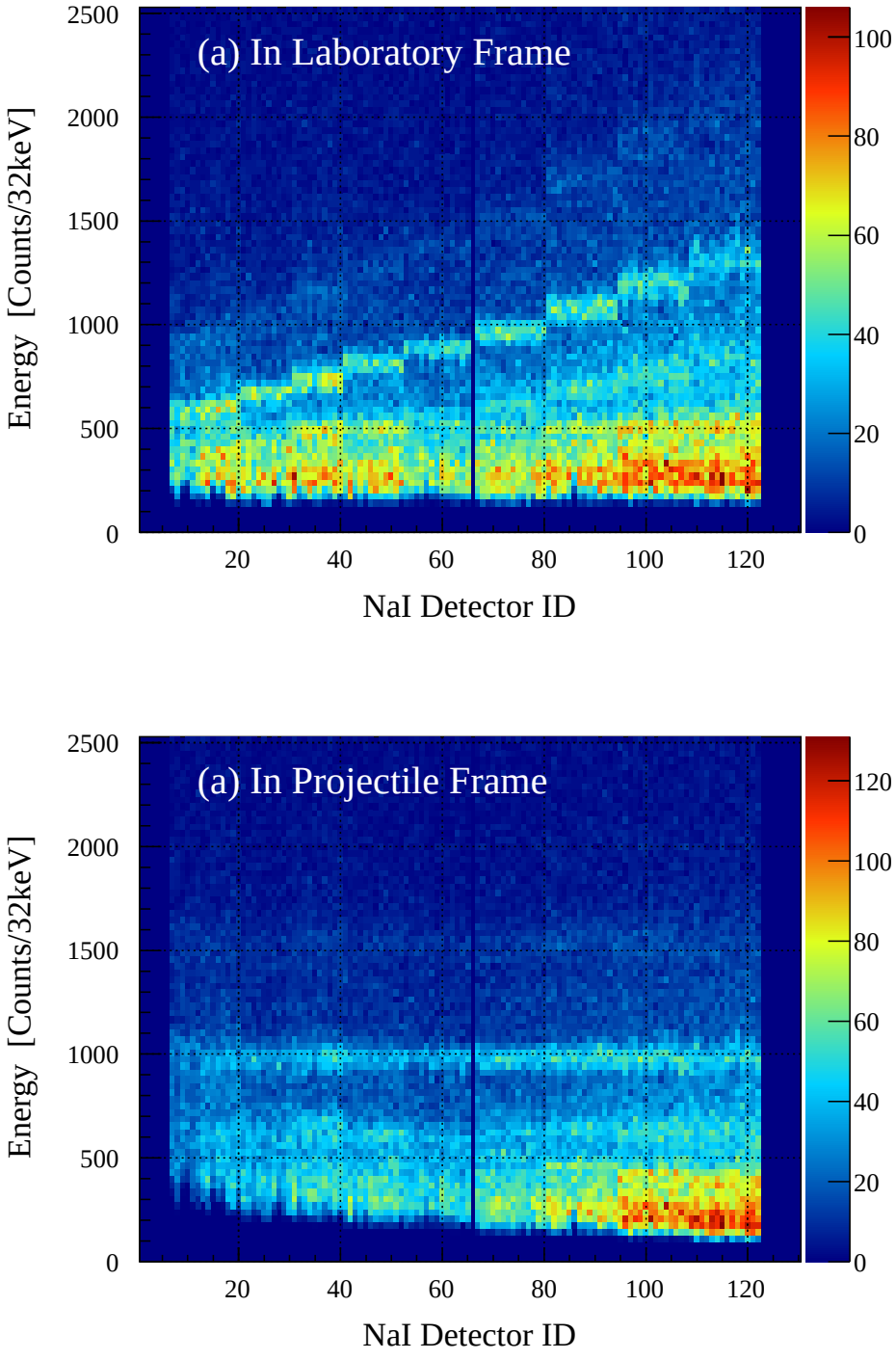

Figure 3.12: γ-ray energy spectra measured in coincidence with the C(^{44}S,^{40}Si) reaction. Panel (a) shows the ID numbers of NaI(Tl) detectors versus the γ-ray energies spectrum obtained in the laboratory frame, while for panel (b) a Doppler-shift correction into the projectile frame was applied.

3.3.3 Timing Gate for Background Reduction

The de-excitation γ-rays were detected in coincidence with the projectiles and secondary fragmentation products. In addition to the γ-rays emitted from the ejectiles excited in the secondary reaction target, the $COIN$ trigger condition included other background radiations. This background radiation originated from surrounding materials, light particles transmitted through BigRIPS, accidental coincident environmental radiations, and neutrons produced in the secondary reaction target or other materials. In order to reduce the background radiation, a timing gate was imposed on the observed γ-rays. The DALI2 time information was extracted relative to the F8Pl time information. Figure 3.13 (a) shows the DALI2 Timing spectrum in coincidence with the C(^{44}S,^{40}Si+γ) reaction. While large amounts of delayed events can be seen, there is no evident component of constant background radiation, indicating that the accidental coincident background radiation was negligible in γ-ray energy spectra. Figure 3.13 (b) shows the Doppler-shift corrected γ-ray energy versus the DALI2 Timing. The dense distribution seen at 985(11) keV corresponds to the known $2^+_1 \rightarrow 0^+_{g.s.}$ transition in ^{40}Si. In order to impose the appropriate gate on the DALI2 Timing, the intensity of the γ-ray peak at 985 keV was investigated as a function of the DALI2 Timing. This is shown in Fig. 3.13 (c), where a sharp peak can be seen. This peak was well-reproduced by the Gaussian function shown by the dashed curve with a width of 3.0 nsec (FWHM). The peak-to-total ratio as a function of the DALI2 Timing is shown in Fig. 3.13 (d). As conclusion of this analysis, the gate imposed on the DALI2 Timing had a width of 8 nsec (-5 nsec $<$ DALI2 Timing $<$ 3 nsec) as shown by the dashed lines in Fig. 3.13 (c) and (d).

3.4 Monte Carlo Simulations

The aim of the simulations was to obtain the the γ-ray detector response function and estimate the γ-ray detection efficiency under the realistic experimental conditions for the secondary reactions.

3.4.1 Input Information

The γ-rays induced by secondary reactions interact with all the materials of the experimental setup. Therefore, these materials, NaI(Tl) detectors and housing, reaction target, beam pipe and atomic background shield, were included into the simulations.

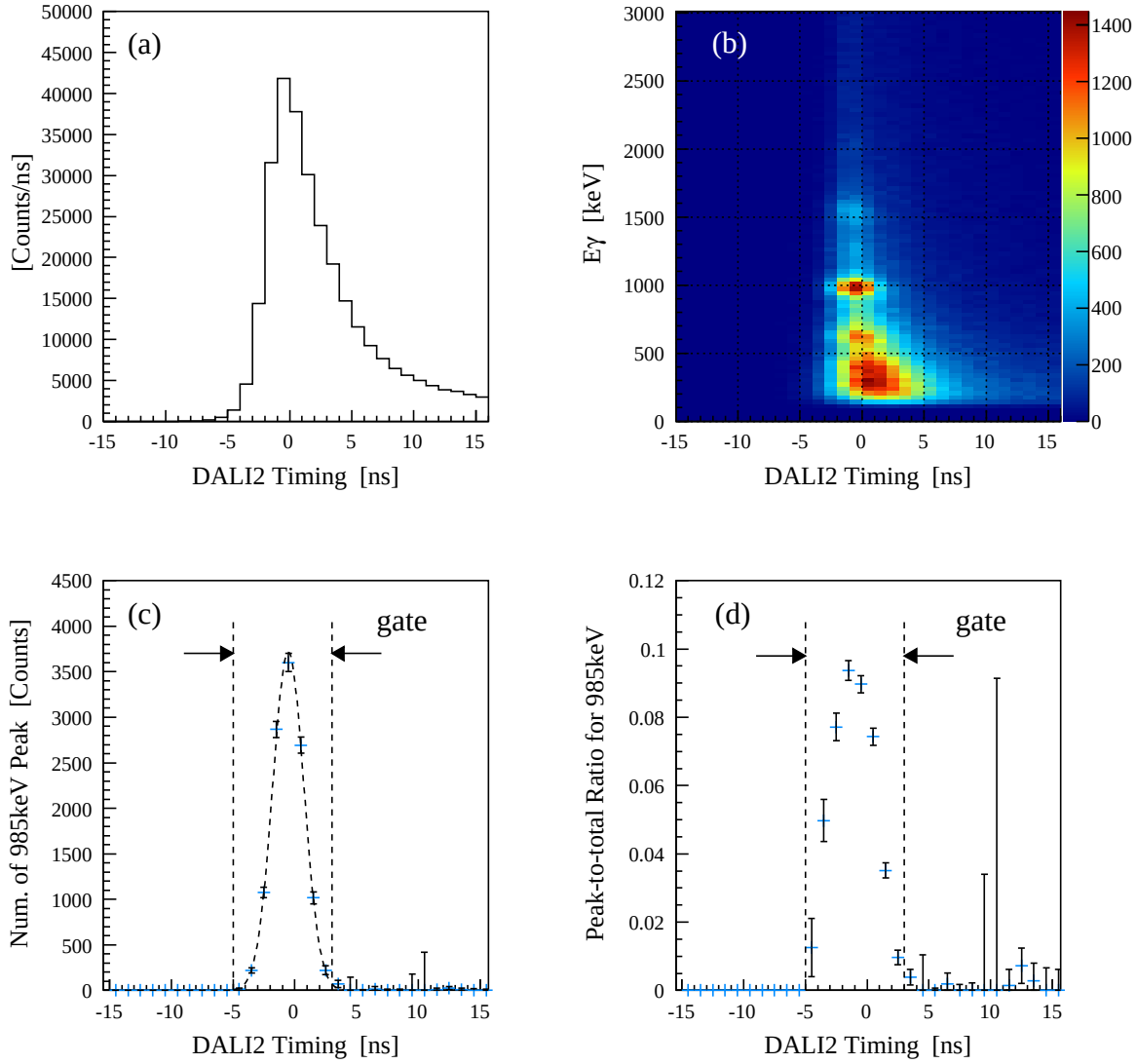

Figure 3.13: Spectra of the DALI2 Timing in coincidence with the C(^{44}S,^{40}Si+γ) reaction. Panel (a) shows the DALI2 Timing distribution where large amounts of delayed events attributed to background radiation are seen. Panel (b) shows the Doppler-shift corrected γ-ray energy versus the DALI2 Timing. The distribution observed at 985 keV corresponds to the known $2_1^+ \rightarrow 0_{g.s.}^+$ transition in ^{40}Si. The number of counts and the peak-to-total ratio for the 985 keV γ-ray peak as a function of the DALI2 Timing are shown in (c) and (d), respectively. The gate imposed on the DALI2 Timing (-5 nsec to +3 nsec) and a Gaussian fit function are indicated as dashed lines and a dashed curve, respectively.

The γ-ray energy resolution obtained from in-beam γ-ray spectroscopy depends not only on the intrinsic energy resolution of the NaI(Tl) detectors but also on the angular resolution and the velocity broadenings of the fast moving nuclei. Taking into account ΔE_γ^{lab}, $\Delta\beta$ and $\Delta\theta_\gamma^{lab}$ and the Doppler formula (3.21), the energy resolution results in

$$\left(\frac{\Delta E_\gamma^{proj}}{E_\gamma^{proj}}\right)^2 = \left(\frac{\Delta E_\gamma^{lab}}{E_\gamma^{lab}}\right)^2 + \left(\frac{\beta\gamma^2(\beta - cos\theta_\gamma^{lab})}{1-\beta cos\theta_\gamma^{lab}}\right)^2 \left(\frac{\Delta\beta}{\beta}\right)^2 + \left(\frac{\beta sin\theta_\gamma^{lab}}{1-\beta cos\theta_\gamma^{lab}}\right)^2 (\Delta\theta_\gamma^{lab})^2. \tag{3.22}$$

In the above expression, the first term represents the intrinsic energy resolution. In order to reproduce the intrinsic energy resolution in the Monte Carlo simulations, the experimentally deduced resolution for every NaI(Tl) detector (described in Section 3.3.1) was used as input parameter individually. The contribution of the velocity broadening to the γ-ray energy resolution is represented in the second term of Equation (3.22). Therefore, the velocity broadening of the projectile particle was extracted from the experimental data and inserted in the simulation. The projectile and ejectile energy loss in the reaction target was calculated based on the energy loss calculation code ATIMA and considered in the simulations as well. Secondary reactions introduce a velocity shift of the ejectiles. In the simulation, this velocity shift was taken into account according to the empirical formula established by V. Borrel *et al.*:

$$\frac{V_f^2}{V_p^2} = 1 - \frac{B_n(A_p - A_f)}{A_p E_f}, \tag{3.23}$$

where the index p and f stand for the projectile and the fragment, respectively, V is the velocity, A is the mass number, E is energy, and B_n is the binding energy per ablated nucleon. The position and angular distribution of the projectile particle at the reaction target were also taken into account in the simulation. The mean value and width of the distribution were extracted from the experimental data as described in Section 3.1.3 and used as parameters in the Monte Carlo simulations.

3.4.2 Determination of NaI(Tl) Detector Polar Angle

As described in Section 3.3.2, the Doppler-shift depends on the γ-ray emission angle relative to the beam axis.

Figure 3.14 (a) shows the simulated polar angle coverage of every NaI(Tl) detector. In this plot, events with a γ-ray multiplicity of M=1 were selected because Compton scattering events no longer have the correct polar angle information. The average value

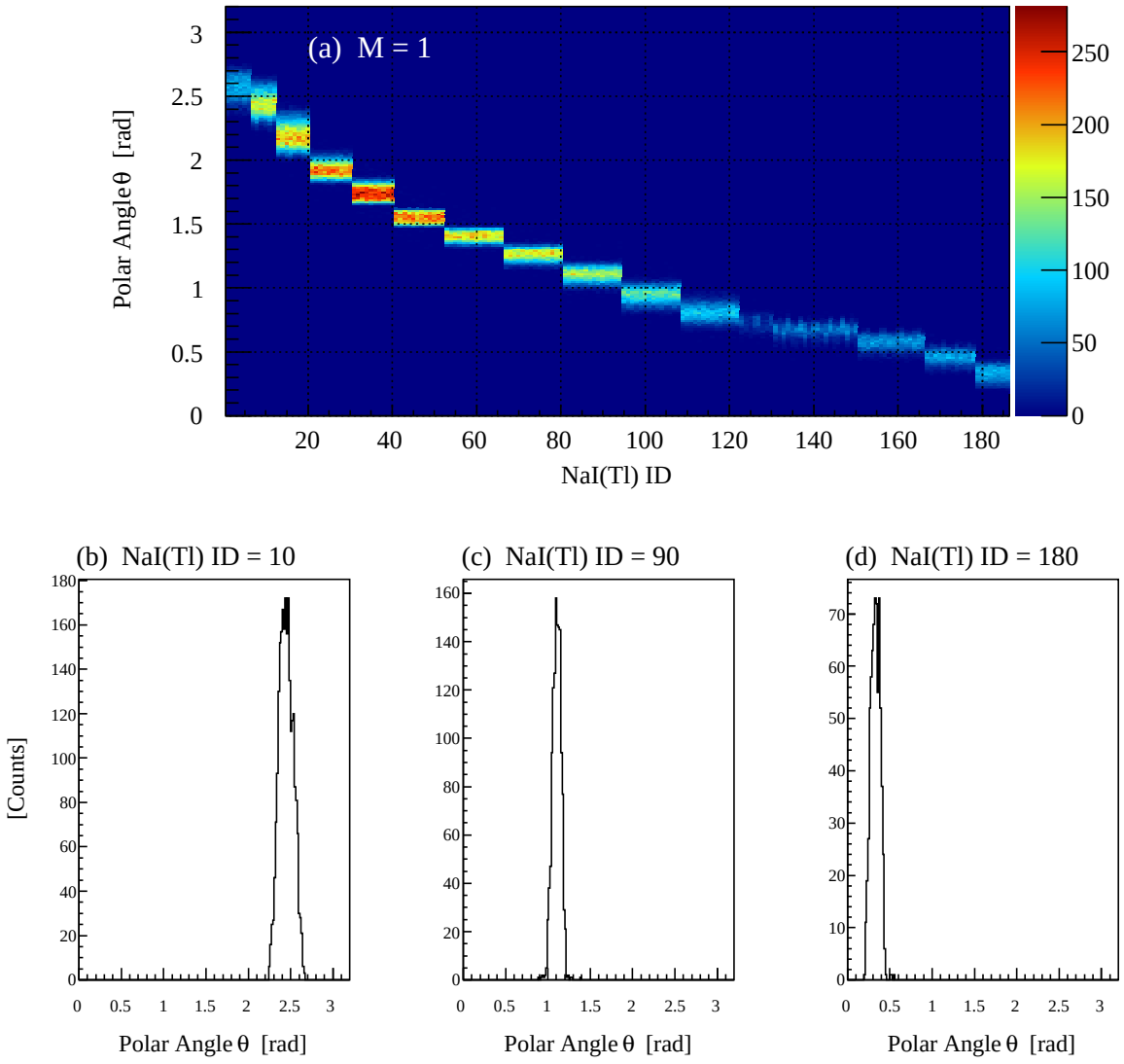

Figure 3.14: Panel (a) shows the correlation between the γ-ray emission polar angle and the NaI(Tl) detector ID obtained by the Monte Carlo simulations with multiplicity selected. Panel (b), (c) and (d) show examples of the polar angle distribution for individual NaI(Tl) detectors. The average polar angle of every NaI(Tl) detector was determined by these spectra and used for the Doppler-shift correction.

of the polar angle distribution was evaluated for each NaI(Tl) detector and used for the Doppler-shift correction. Examples of polar angle distributions for individual detectors are shown in Figure 3.14 (b) (c) (d).

3.4.3 Detection Efficiency Error

The Monte Carlo simulation of the γ-ray spectrometer was used to estimate intensities of unknown γ-ray lines. The error of γ-ray detection efficiency involved in the simulations was estimated by referring the well-known γ-ray lines of the standard sources.

Figure 3.15 (a), (b) and (c) shows the γ-ray energy spectra measured with standard γ-ray sources of ^{137}Cs, ^{60}Co and ^{88}Y, respectively. The Monte Carlo simulations were performed in such a way as to reproduce these spectra. As shown in figures, the simulated response functions, together with background spectrum, was used in fitting spectra. The measured spectra were well reproduced in the case of ^{137}Cs and ^{88}Y, whereas discrepancies around Compton edge could be seen in the spectrum of ^{60}Co. Although the response function in Figure 3.15 (b) are shown in the region above 400-keV to highlight the discrepancies, the measured spectra, in fact, were fitted in the region above 900-keV. These differences between the measured- and the simulated- spectrum are considered to be due to the non-linear response of a NaI(Tl) scintillator to low energy γ-rays or X-rays [43] and low energy electrons induced by Compton scattering. The simultaneous pile-up effects caused by two different γ-rays in a same detector, which are not reproduced in the present simulation, are also the possible reason for these discrepancies.

The error of the γ-ray detection efficiency was estimated by evaluating the number of decay event obtained in the measured- and the simulated- spectra. For the measured spectra, the number of the decay event can be deduced from a radiation intensity of source, I_γ, and a measuring time, T, :

$$N_{meas} = I_\gamma \times T. \tag{3.24}$$

The γ-ray detection efficiency, ε_{meas}, and the live time of data taking system, P, are factored into the number of decay event detected in a measured spectrum, N_{spec}, :

$$N_{spec} = P \times \varepsilon_{meas} \times N_{meas}. \tag{3.25}$$

Contrastively, in a simulated spectrum, the number of decay event, N_{sim}, is treated as a fitting parameter and, therefore, can be obtained in such a way as to reproduce a measured

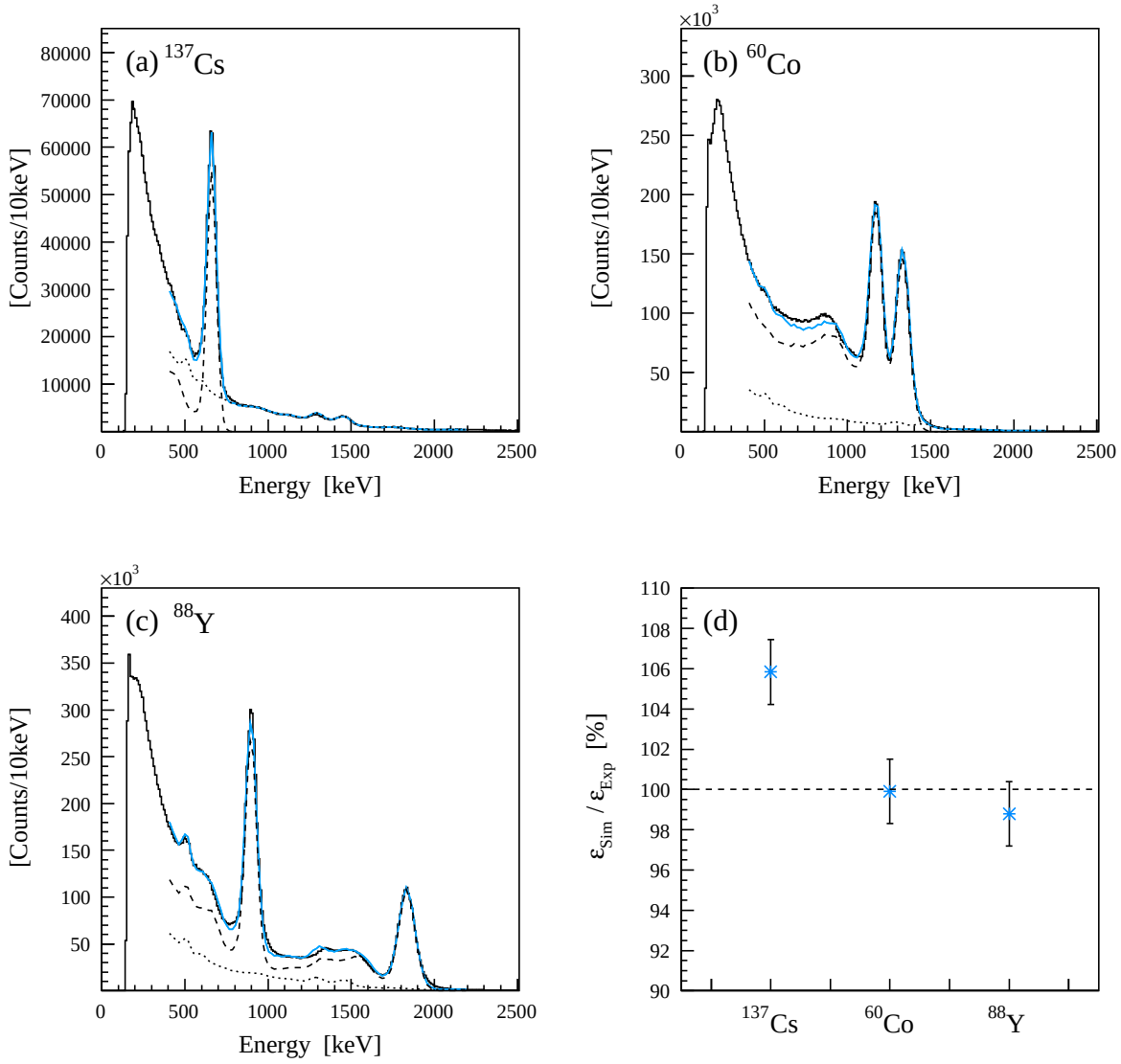

Figure 3.15: Efficiency calibration of the DALI2 γ-ray spectrometer using standard γ-ray sources. Panel (a), (b) and (c) show the energy spectra obtained from the γ-ray sources of ^{137}Cs, ^{60}Co and ^{88}Y, respectively. Each spectra was fitted with the simulated γ-ray source- and the background- spectra, as shown by solid lines (blue). The contributions of γ-ray source and background to fitted functions were indicated by dashed and dotted curves, respectively. Panel (d) shows deviations of γ-ray detection efficiency between measurement and simulation with 1.6% error bars due to the uncertainty of each γ-ray source intensity (details in text).

spectra. The γ-ray detection efficiency involved in a simulation, ε_{sim}, is expressed as

$$N_{spec} = \varepsilon_{sim} \times N_{sim}. \tag{3.26}$$

Considering the above relations, the deviation of ε_{sim} from ε_{meas} is given as

$$\frac{\varepsilon_{sim}}{\varepsilon_{meas}} = \frac{N_{meas} \times P}{N_{sim}} = \frac{I_\gamma \times T \times P}{N_{sim}}. \tag{3.27}$$

Figure 3.15 (d) shows the deviations obtained with γ-ray sources of ^{137}Cs, ^{60}Co and ^{88}Y. The error bars indicate the uncertainty of the radiation intensity of each source, 1.6-%. The error of the detection efficiency of the DALI2 γ-ray spectrometer was estimated to be 6.0-% which was the largest deviation observed with ^{137}Cs source as shown in the figure.

3.5 Summary of the Systematics Errors

The small contributions of other particles to the selection gate applied for the particle identification, selection of the mass- and atomic- number, were ignorable as given in Section 3.2.3.

The systematic errors in energies of the observed γ-ray peak were attributed to the error in energy calibration of γ-ray spectrometer and the uncertainty in γ-ray emission position due to the thick target and the life time of the excited states. The systematic error in energy calibration was obtained to be 3.0-keV as discussed in Section 3.3.1. The systematic error in the Doppler-shift correction due to the uncertainty in γ-ray emission position was estimated to be 0.83-% as a result of the Monte Carlo simulations.

As explained in Section 3.4.3, the systematic errors in intensities of the observed γ-rays were attributed to the error of the detection efficiency of the DALI2 γ-ray spectrometer, which were obtained to be 6.0-% by referring the well-known intensities of the standard γ-ray sources.

Chapter 4

Experimental Results and Discussions

In this chapter, the results and discussions concerning the in-beam γ-ray spectroscopy of ^{38,40,42}Si via multi nucleon removal reactions. The chapter is divided into two main parts. In Section 4.1, the de-excitation γ-rays obtained in the experiment and the excited level schemes of ^{38,40,42}Si nuclei are explained. Possible candidates for the 4^+ excited state of these nuclei can be extracted from obtained data. In Section 4.1, the systematics of the energies of 2^+ and the 4^+ excited state are described. Rapid developments of the nuclear deformation in neutron-rich Si isotopes are discussed here.

4.1 Spectroscopy of ^{36,38,40,42}Si via Multi Nucleon Removal Reactions

The purpose of the experiment was to investigate the excited states of neutron rich even-even nuclei ^{38,40,42}Si. In-beam γ-ray spectroscopy based on multi nucleon removal reaction was performed. Figure 4.1 shows two dimensional plot of the energies of de-excitation γ-rays measured by NaI detector array DALI2 versus produced Si isotopes identified by the ZeroDegree spectrometer. Figure 4.1 (a) was obtained via multi nucleon removal reaction of C(^{40}S,^{A}Si+γ)X, while Figure 4.1 (b) was measured in coincidence with C(^{44}S,^{A}Si+γ)X reaction. Clear peak components in γ-ray energy for some isotopes can be seen in these figures.

The result of the spectroscopy of ^{36}Si is explained at first in Section 4.1.1. Because of its previously known excited level scheme, ^{36}Si is an indicative nucleus to confirm

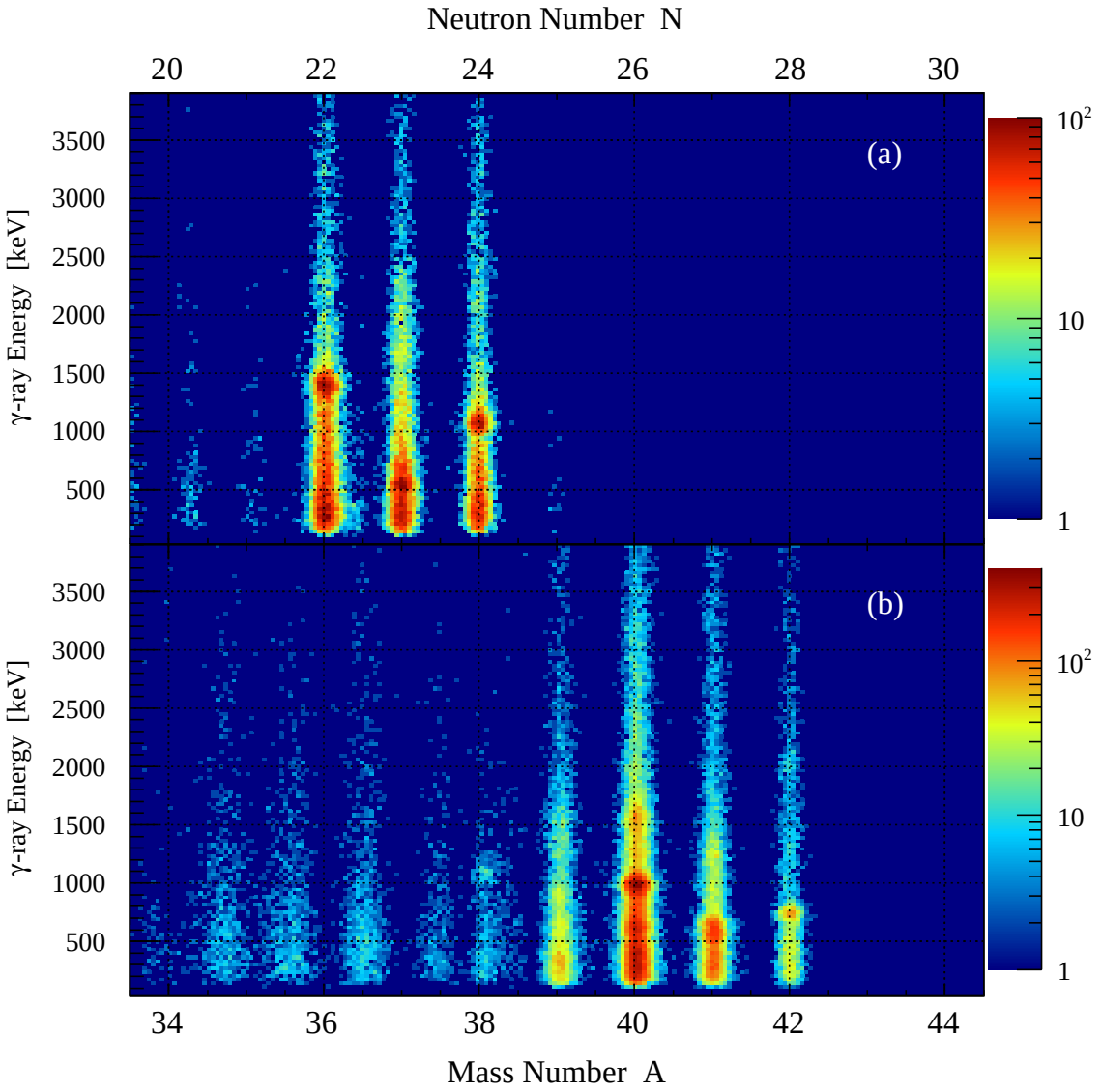

Figure 4.1: The plot of mass number A and Doppler-shift corrected γ-ray energy obtained in coincidence with reaction products of Si isotopes. (a) and (b) were measured via multi nucleon removal reaction of C(^{40}S,^{A}Si+γ)X and C(^{44}S,^{A}Si+γ)X, respectively.

the validity of the present experiment. The experimental results of the spectroscopy of ^{38,40,42}Si nuclei and the adopted level schemes are given in Section 4.1.2, 4.1.3 and 4.1.4, respectively.

4.1.1 Excited States in ^{36}Si

The excited states of ^{36}Si was investigated by in-beam γ-ray spectroscopy based on four nucleon removal reaction, C(^{40}S,^{36}Si). The γ-ray transitions and the excited level scheme of ^{36}Si obtained experimentally are explained here and compared with the previously known observables.

γ-ray Energy Spectrum

Figure 4.2 shows the γ-ray energy spectrum measured in coincidence with C(^{40}S,^{36}Si)X reaction, for which Doppler-shift effect is corrected. The timing window gate on the γ-ray detectors was imposed as described in Section 3.3.3. Figure 4.2 (a) shows the single spectrum, while (b) was obtained for the events with multiplicity selection. The multiplicity represents the number of the actuated NaI(Tl) detector in a trigger, which is expressed as M, hereinafter. An intense peak can be seen at around 1400 keV in both spectra, which attributes to the de-excitation γ-ray for the previously known $2^+ \rightarrow 0^+_{g.s}$ transition in ^{36}Si. This peak was compared with the response function of the NaI(Tl) detector array. The response function was obtained by the Monte Carlo simulations as described in Section 3.4. As a result, it was confirmed that the width of this peak was too wide to be fitted with a response function of single γ-ray. The width of peak in obtained spectra was $\sim$250 keV (FWHM), while the one of the response function in this energy region was $\sim$150 keV (FWHM), indicating that this peak was composed of two or more γ-rays. Hence, γ - γ analysis were applied with M=2 condition as shown in Figure 4.2 (c). A peak can be seen at $\sim$1400 keV in the figure and two different γ-ray peak was extracted as a best fitting result of the response function. However, there still was a possibility that it were coincident events with Compton scattering and/or background radiations because single γ-ray spectrum shown in Figure 4.2 (a) exhibited a large component of them at $\sim$1400-keV region. In order to make sure that the 1400-keV peak originated from two different γ-rays, calorimetric analysis was performed.

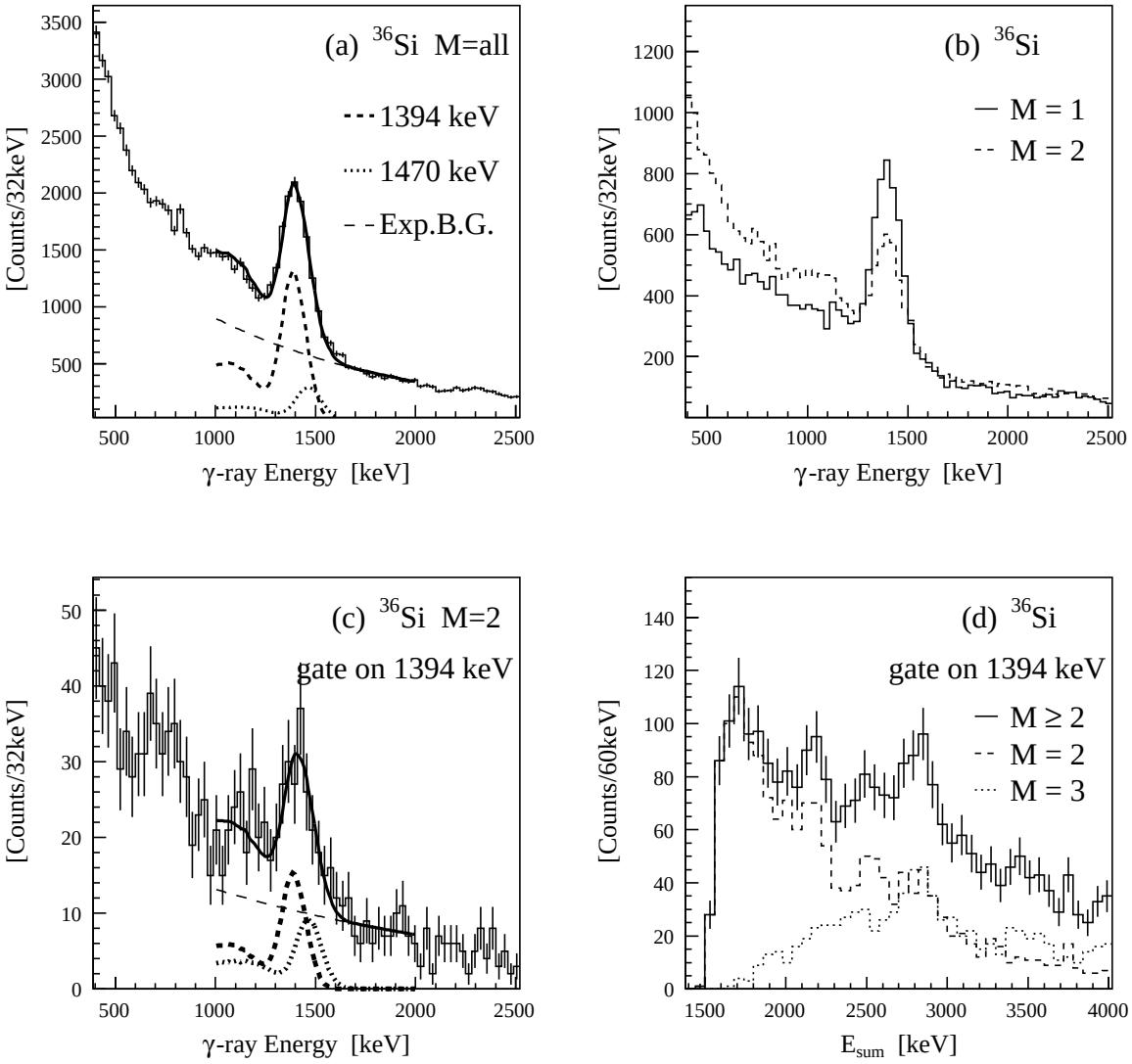

Figure 4.2: The spectra obtained in C(^{40}S,^{36}Si)X reaction. (a) shows the single γ-ray energy spectrum, while (b) is obtained in M=1 and M=2 conditions. The γ - γ spectrum with a gate on 1408-keV γ-ray and M=2 condition is shown in (c). The result of the calorimetric analysis, which is explained in text, is exhibited in (d).

Calorimetric Analysis for Gamma Decay

If both of the cascaded two or more γ-rays were detected as photo-peak, summation of these γ-ray energies,

$$E_{sum} = \sum_{i=1}^{M} E_{\gamma i}, \tag{4.1}$$

represents the energy of excited state and peak shape would be exhibited in an E_{sum} spectrum. On the other hand, if a γ-ray was measured in coincidence with Compton scattering and/or background radiations, no peak shapes would be seen in an E_{sum} spectrum.

Figure 4.2 (d) shows the result of this calorimetric analysis applied to ^{38}Si data, in which the solid line exhibit the E_{sum} spectrum obtained in coincidence with 1400-keV γ-ray for M$\geq$2 events, while the dashed and dotted lines were obtained with M=2 and M=3 conditions, respectively. A peak can be seen at $\sim$2800 keV indicating a 1400-keV peak obtained in single γ-ray energy spectrum, as exhibited in Figure 4.2 (a), was composed of two coincident γ-ray peaks. Based on this robust evidence of the 1400-keV doublet peak, γ-ray energy spectra were fitted by using two different response functions together with background shape as indicated by the solid, dashed and dotted lines in Figure 4.2 (a). The exponential function was assumed for background shape. Finally, two coincident γ-ray with the energy of 1394(15) and 1470(38) keV were obtained for the de-excitation γ-ray of ^{36}Si.

Comparison with the Known Level Scheme of ^{36}Si

The de-excitation γ-ray observed in the experiment, 1394(15) and 1470(38) keV, exhibited ^{36}Si nucleus has excited states at 1.394(15) and 2.864(40) MeV.

Figure 4.3 shows the comparison between the excited level scheme of ^{36}Si obtained in the experiment and the one previously proposed by X. Liang et al.[44], which was measured via deep inelastic reaction of ^{36}Si. As seen in the level scheme (Figure 4.3), the adopted energies of two excited states in the experiment was consistent to the previously known energies of 2^+ and 4^+ excited states within errors, indicating the validity of the present experiment and the high productivity of 4^+ excited state via multi nucleon removal reaction.

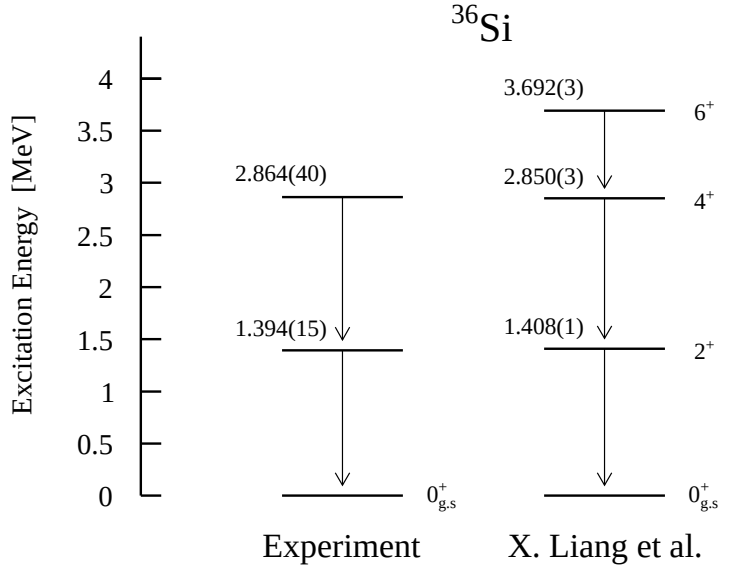

Figure 4.3: Comparison between the excited level scheme of ^{36}Si obtained in the experiment and the one previously proposed by X. Liang et al..

4.1.2 Excited States in ^{38}Si

The excited states of ^{38}Si was investigated by in-beam γ-ray spectroscopy based on two proton removal reaction, C(^{40}S,^{38}Si). The γ-ray transitions and the excited level scheme of ^{38}Si obtained experimentally are explained here.

γ-ray Energy Spectrum

The Doppler-shift corrected γ-ray energy spectrum measured in coincidence with C(^{40}S,^{38}Si) reaction are shown in Figure 4.4. A single γ-ray energy spectrum is given in Figure 4.4 (a), while (b) exhibits the spectra obtained with M=1 and M=2 conditions. An intense peak were observed at around 1100 keV in both figure (a) and (b). This peak mostly attributes to the $2^+ \rightarrow 0^+_{g.s}$ transition in ^{36}Si, which were obtained at 1084(20) keV by previous work [26, 45]. However, a possibility of the doublet or triplet peak was confirmed as a result of comparison with the response function of the NaI(Tl) detector array. The width of peak in obtained spectra was $\sim$220 keV (FWHM), while the one of the response function in this energy region was $\sim$120 keV (FWHM). In addition three γ-ray lines were observed around this energy by proton inelastic reaction of ^{38}Si in a previous experiment [45]. With the help of the previous result, three γ-ray lines with energies

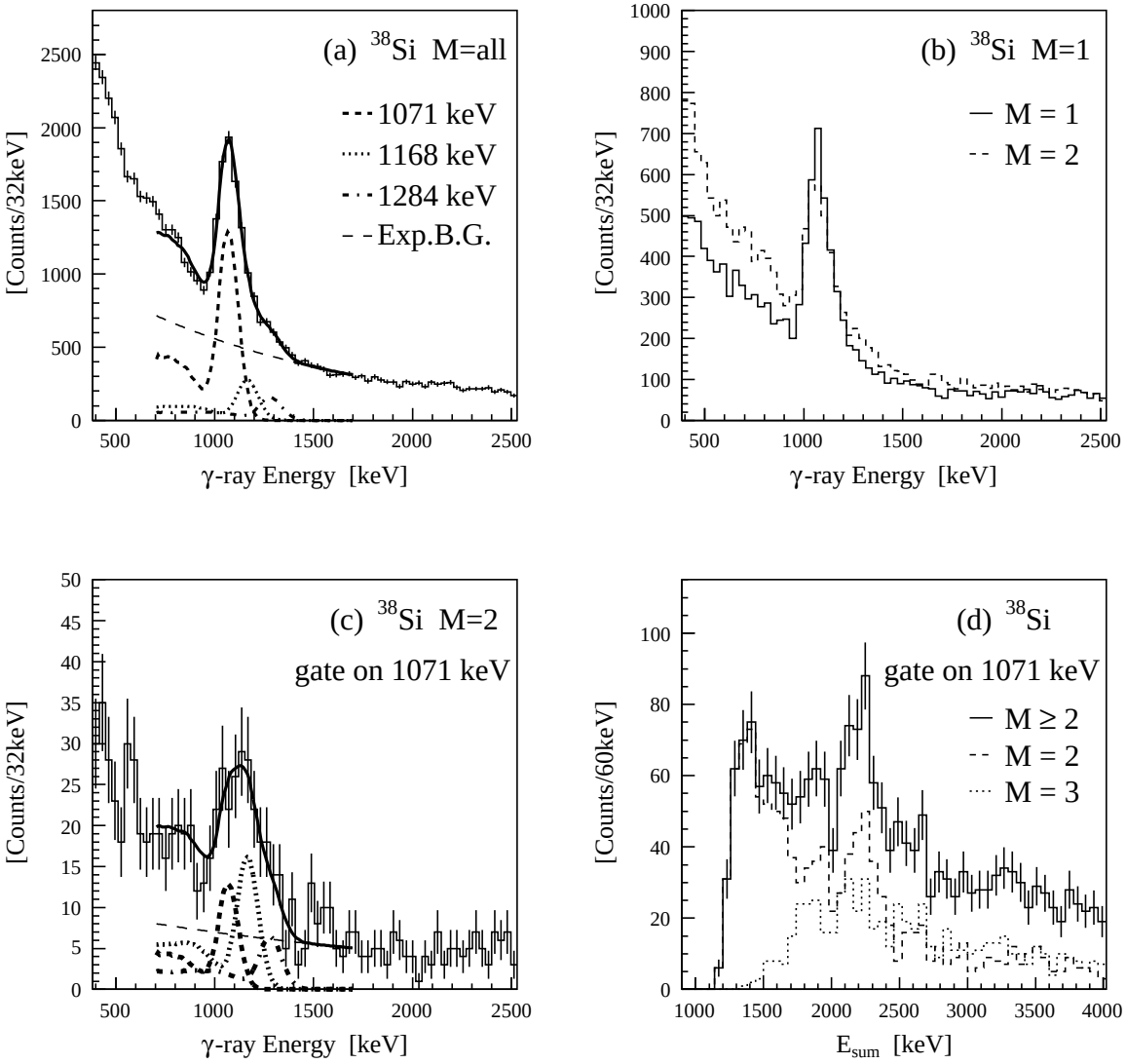

Figure 4.4: The spectra obtained in C(^{40}S,^{38}Si) reaction. (a) shows the single γ-ray energy spectrum, while (b) is obtained in M=1 and M=2 conditions. The γ - γ spectrum with a gate on 1071-keV γ-ray and M=2 condition is shown in (c). The spectrum of E_{sum} with a gate on 1071-keV γ-ray and multiplicity is exhibited in (d).

of 1071(12), 1168(22) and 1284(26) keV were obtained by fitting the spectrum shown in Figure 4.4 (a), where three peaks with initial γ-ray energies estimated from Ref. [45] were used in the fitting procedure. Figure 4.4 (c) shows the γ-ray energy spectrum obtained by γ - γ analysis with a gate on 1071-keV γ-ray and M=2 condition, which also supports the existence of three γ-ray lines. The results of calorimetric analysis with a gate on 1071-keV γ-ray are shown in Figure 4.4 (d), where a clear peak can be seen at around 2200 keV. Considered with the yield in γ - γ spectrum and a peak observed in E_{sum} spectrum, the extracted γ-ray lines with the energy of 1168(22) and 1284(26) keV were confirmed to be in coincidence with 1071-keV γ-ray which corresponds to the $2_1^+ \rightarrow 0_{g.s}^+$ transition.

Level Scheme of ^{38}Si

In this experiment, three γ-ray transitions with energies of 1071(12), 1168(22) and 1284(26) keV in ^{38}Si were extracted. The 1071(12)-keV γ-ray corresponds to the previously known $2_1^+ \rightarrow 0_{g.s}^+$ transition [26]. The others, 1168(22) and 1284(26)-keV γ-ray lines, were confirmed to populate the 2_1^+ state experimentally, which are candidates for the $4_1^+ \rightarrow 2_1^+$ transition. From the known tendency that yrast states, including the 2_1^+ and 4_1^+ states, tend to be favorably populated with larger cross sections in nucleon removal reactions, the 1168(22)-keV γ-ray line is the more probable candidate for the $4_1^+ \rightarrow 2_1^+$ transition among these two possibilities. The 2239(25)-keV (= 1071 keV + 1168 keV) state was therefore tentatively assigned to be the most probable candidate for the 4^+ state. It is noted that the alternative 4^+ state assignment to the 2355(29)-keV (= 1071 keV + 1284 keV) state does not affect the discussion on the systematics of the level energies of neutron-rich Si isotopes given later.

The excited level scheme in ^{36}Si tentatively adopted, based on the assumption discussed above, is shown in Figure 4.5, where the one previously reported by R. W. Ibbotson et al. [26] is also shown for comparison. The γ-ray decays from 2.239 and 2.355-MeV state to the 2_1^+ state were confirmed for the first time in the present experiment. The ratio $R_{4/2}$ of the 4_1^+ and 2_1^+ state energies with the value of 2.09(5) was deduced with this scheme.

4.1.3 Excited States in ^{40}Si

The excited states of ^{40}Si was investigated by in-beam γ-ray spectroscopy based on four four removal reaction, C(^{44}S,^{40}Si). The γ-ray transitions and the excited level scheme

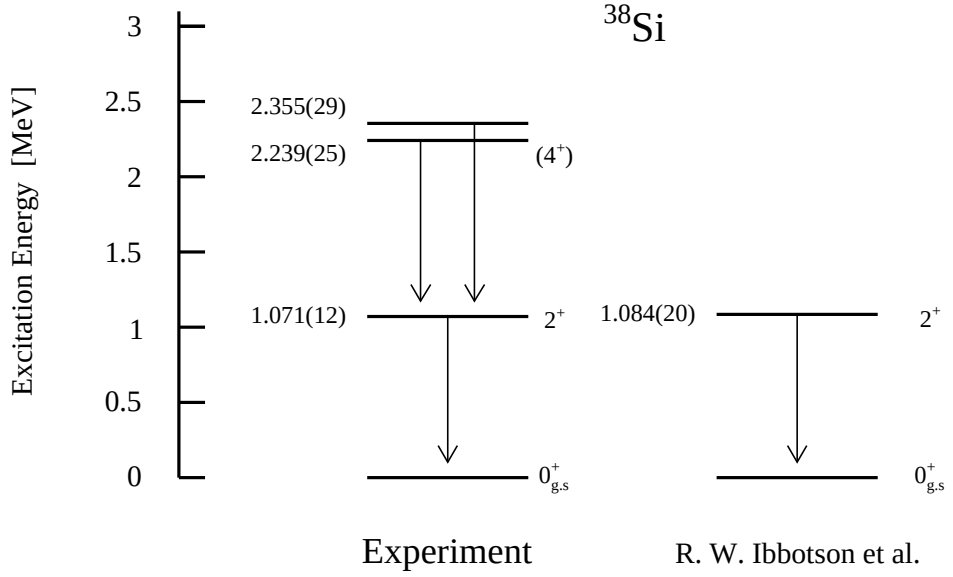

Figure 4.5: Comparison between the excited level scheme of ^{38}Si obtained in the experiment and the one previously proposed by R. W. Ibbotson et al..

of ^{40}Si obtained experimentally are explained here.

γ-ray Energy Spectrum

The Doppler-shift corrected γ-ray energy spectra measured in coincidence with C(^{44}S,^{40}Si) reaction were shown in Figure 4.6. Three peaks were clearly observed in single γ-ray energy spectrum as shown in Figure 4.6 (a) and also obtained under M=1 and M=2 conditions as shown in Figure 4.6 (b). As a result of fitting using response function of NaI(Tl) detector array together with an exponential background shape on single spectrum (a), the γ-ray lines with energies of 629(8), 985(11) and 1539(16) keV were extracted. The most intense γ-ray line obtained at 985(11) keV corresponds to the $2^+_1 \rightarrow 0^+_{g.s}$ transition previously observed at 986(5) keV by C.M. Campbell et.al. [37], who also reported 638(5)-keV de-excitation γ-ray of ^{40}Si. The 1539(16)-keV γ-ray line was observed for the first time in this work.

The γ - γ spectrum with a gate on 985-keV γ-ray under M$\geq$2 condition is shown in Figure 4.6 (c) together with the fitted curve composed of response functions and an exponential background curve. In this fitting procedure, the amplitudes of response functions used for 629-keV and 1539-keV γ-ray lines were fixed by the estimated values from single

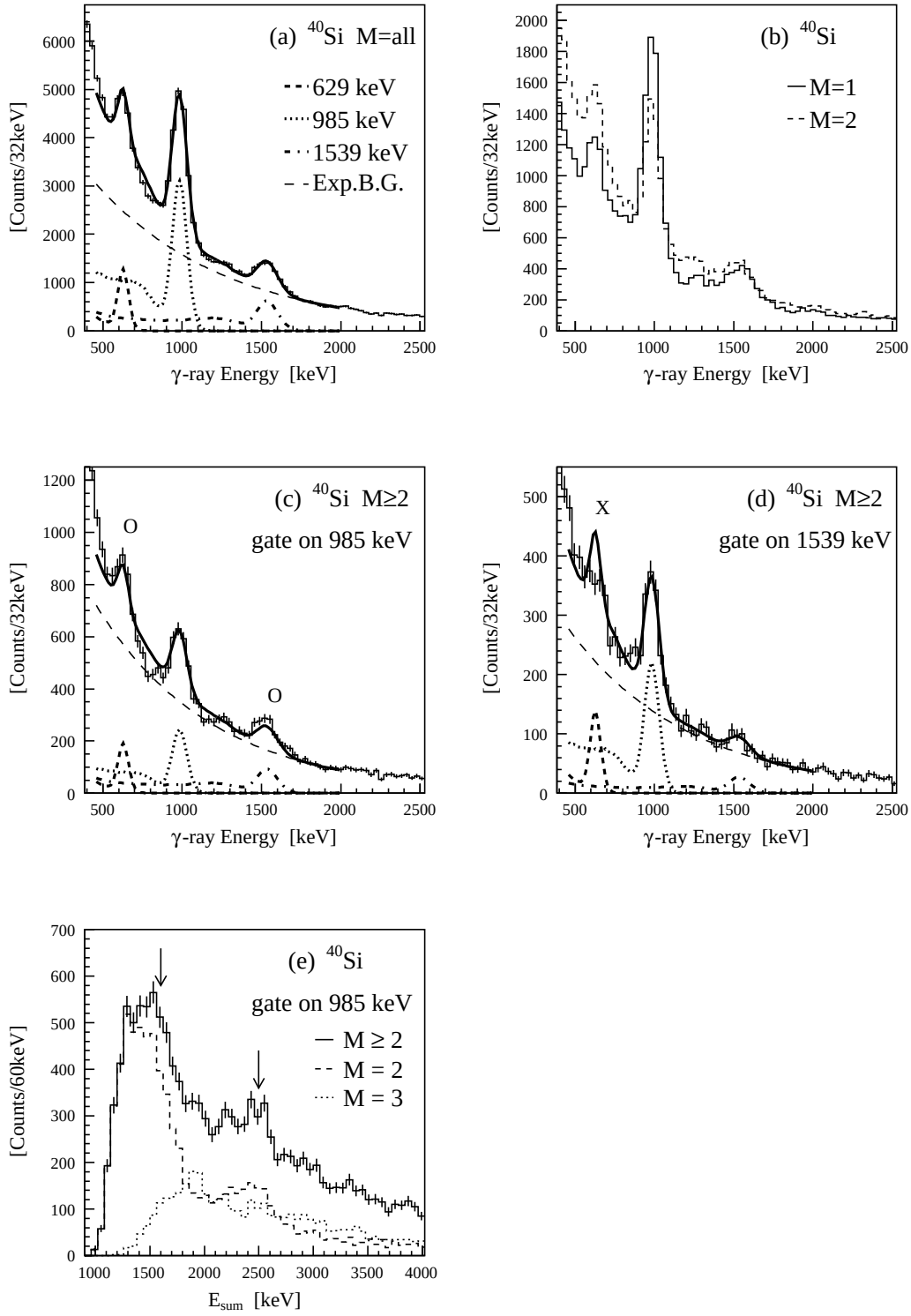

Figure 4.6: Doppler-shift corrected γ-ray energy spectrum obtained in C(^{44}S,^{40}Si) reaction (a), while (b) is obtained under M=1 and M=2 conditions. The γ - γ analysis is performed with gates on 985 and 1539keV as shown in (c) and (d), respectively. (e) shows the results of calorimetric analysis with a gate on 985-keV γ-ray.

spectrum (a): yield of each γ-ray was multiplied by the full-energy-peak efficiency for 985 keV γ-ray. The spectrum was well reproduced by the fitting curve, indicating that both of two γ-ray lines, 629- and 1539-keV γ-ray, were in coincidence with the $2_1^+ \rightarrow 0_{g.s.}^+$ transition of 985-keV γ-ray. In order to examine the coincidence between 629- and 1539-keV γ-ray, γ - γ analysis with a gate on 1539-keV γ-ray was also performed. The extracted spectrum and fitted curve are shown in Figure 4.6 (d). Similar to the above, the amplitude of response function used for 629-keV γ-ray line was fixed by the estimated value. As can be seen in the figure, the fitting curve overestimates the spectrum around 629 keV. Thus, the both γ-ray lines of 629- and 1539-keV are considered to be transitions directly feeding to the 2_1^+ state of ^{40}Si.

Figure 4.6 (e) shows the E_{sum} spectrum obtained as a result of calorimetric analysis with a gate on 985-keV γ-ray peak under M$\geq$2 (solid line), M=2 (dashed line) and M=3 (dotted line) conditions. Two peaks at around 1614 keV (= 985 keV + 629 keV) and 2524 keV (=985 keV + 1539 keV) were observed in this spectra, showing existences of the excited states at these energy. It is noted that no significant peak can be observed at around 1970 keV, twice energy as much as 985 keV, in this spectrum, indicating the validity of calorimetric analysis applied to ^{36}Si and ^{38}Si cases.

Level Scheme of ^{40}Si

In the experiment, three γ-ray transitions with energies of 629(9), 985(11) and 1539(16) keV were extracted for de-excitation γ-rays in ^{40}Si. The 985 keV γ-ray corresponds to the previously known $2_1^+ \rightarrow 0_{g.s.}^+$ transition. The others, 629- and 1539-keV γ-ray lines, were confirmed to populate the 2_1^+ state directly by applying γ - γ analysis.

The excited level scheme extracted for ^{40}Si from the present experimental data is shown in Figure 4.7, where the one reported by the previous work [37] is exhibited together for a comparison purpose. In the previous work, 638(5)- and 845(6)-keV γ-rays were observed in addition to the $2_1^+ \rightarrow 0_{g.s.}^+$ transition of 986(5) keV γ-ray line. The 629(9)-keV γ-ray line observed in the present experiment is consistent to the previous 638(5)-keV γ-ray within the margin of error, whereas no clear γ-ray line could be obtained for the previous 845(6)-keV γ-ray.

The two states obtained in the present experiment at 1.61(1) and 2.52(2)-MeV were the candidates for the 4_1^+ state. As a result of analysis, the population yield of 2.52(2)-MeV state was almost twice as much as that of 1.61(1)-MeV state. Thus, the 2.52(2)-MeV state was more likely to be the 4_1^+ state based on the same consideration for preferential

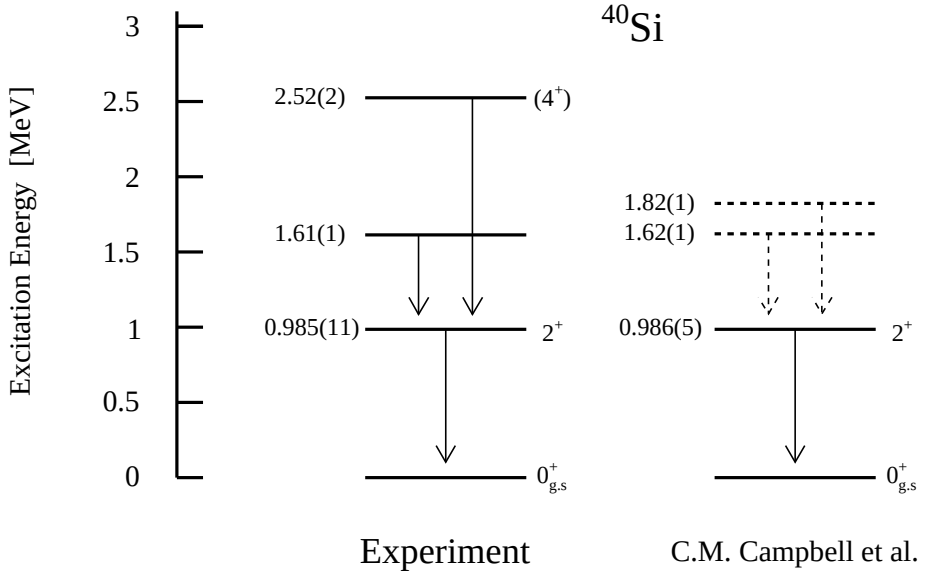

Figure 4.7: The excited level scheme extracted for ^{40}Si from the present experimental data is shown in comparison with a previous work performed by C.M. Campbell et.al..

yrast feeding that were discussed for ^{38}Si. In addition, the systematics trend of 2_1^+ energy also supported 2.52(2)-MeV state as 4_1^+ state. The gradual decrease of the 2_1^+ energy observed in even-even Si isotopes around $A \sim 40$ suggested the enhancement of nuclear collectivities. If the 1.61 MeV state were assumed to be 4_1^+ state, the small $R_{4/2}$ value, 1.63, indicating the characteristic property of magic nuclei, would conflict with the feature inferred by the lowering 2_1^+ energy. Based on the above considerations, 2.52(2)-MeV state therefore was tentatively assigned to 4_1^+ state of ^{40}Si. The ratio $R_{4/2}$ of the 4_1^+ and 2_1^+ state energies with the value of 2.55(3) was deduced with this scheme.

4.1.4 Excited States in ^{42}Si

The excited states of ^{42}Si was investigated by in-beam γ-ray spectroscopy based on four two proton removal reaction, C(^{44}S,^{42}Si). The γ-ray transitions and the excited level scheme of ^{42}Si obtained experimentally are explained here.

γ-ray Energy Spectrum

The Doppler-shift corrected γ-ray energy spectra obtained in coincidence with C(^{44}S,^{42}Si) reaction is shown in Figure 4.8. Figure 4.8 (a) was single γ-ray energy spectrum, while

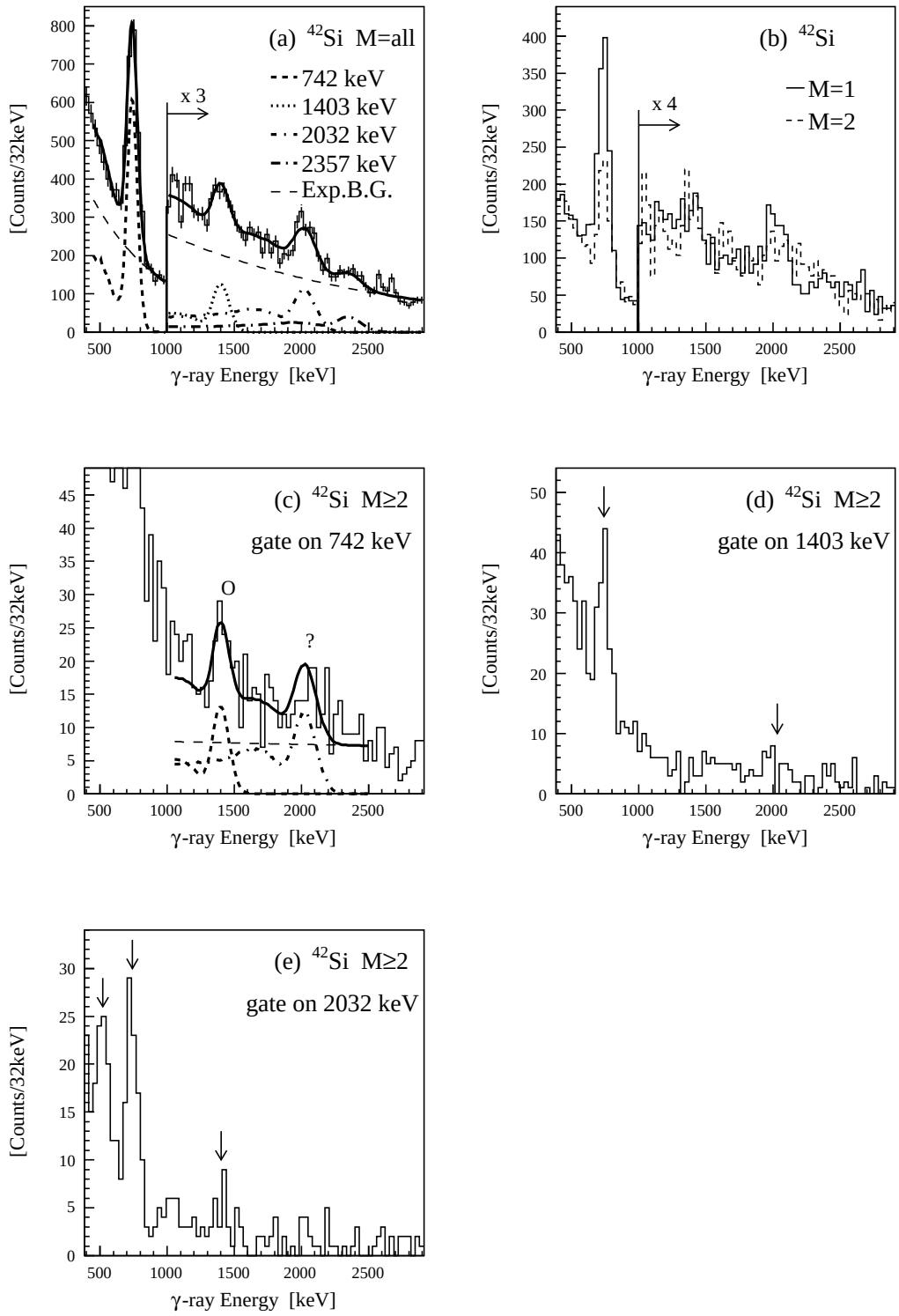

Figure 4.8: Doppler-shift corrected γ-ray energy spectrum obtained in coincidence with C(^{44}S,^{42}Si) reaction (a), while (b) was obtained under M=1 and M=2 conditions. The γ - γ spectra obtained with a gate on 742-, 1043- and 2032-keV γ-ray full-energy peaks are shown in (c), (d) and (e), respectively.

(b) was obtained with M=1 (solid line) and M=2 (dashed line) conditions. Three γ-ray lines were observed in both spectra. The energies of three γ-ray lines were determined to 742(8), 1403(11), 2032(9) and 2357(15) keV by fitting spectra with response functions. The most intense peak observed at 742(8) keV was considered to be the $2_1^+ \rightarrow 0_{g.s.}^+$ transition. The observed energy of this transition agrees with 1.5 standard deviation with the value of 770(19) keV reported in the previous study at GANIL [33].

In order to examine coincidences between observed γ-rays, γ - γ analysis was applied. Figure 4.8 (c) shows the γ - γ spectrum obtained with a gate on 742-keV γ-ray full-energy peak together with a fitted curve (solid line). In this fitting procedure, the amplitude of each γ-ray response function was fixed with a value estimated on an assumption of its full feeding to the 2_1^+ state (742 keV). Two peak-like structures can be seen around 1403 and 2032 keV in figure. The fitted curve reproduced well for 1403-keV peak, whereas yield of 2032-keV peak was likely to be smaller than above estimation. Therefore, full feeding of 1403-keV γ-ray line and partial or no feeding of 2032-keV γ-ray line to the 2_1^+ state are inferred from this spectrum. Figure 4.8 (d) shows the γ - γ spectrum obtained with a gate on 1403-keV γ-ray full-energy peak. As seen in spectrum, an intense peak observed around 742 keV indicates that transition of 1403-keV γ-ray line is feeding to the 2_1^+ state. The concentrations of events was observed also around 2032 keV, implying coincidence between these two γ-rays. Figure 4.8 (e) shows the γ - γ spectrum obtained with a gate on 2032-keV γ-ray full-energy peak. In this spectrum, γ-ray lines with energies of 516(13)- and 742-keV were observed, and the concentrations of events exist around 1403 keV. It was difficult to probe the coincident γ-ray line for 2357-keV γ-ray due to its low statistics.

Level Scheme of ^{42}Si

In the experiment, five γ-ray transitions with energies of 516(13), 742(8), 1403(11), 2032(9) and 2357(15) keV were extracted for de-excitation γ-rays in ^{42}Si. The low energy 2_1^+ state reported in the previous study at GANIL [33, 32] were confirmed by present observation of 742(8)-keV γ-ray transition. As a result of γ - γ analysis, 1403(11) and 2032(9)-keV γ-rays were considered to be the candidates for the $4_1^+ \rightarrow 2_1^+$ transition. The feeding ratio of 2032-keV γ-ray to the 2_1^+ state was smaller than that of 1403-keV γ-ray and estimated value, indicating that it populate fully and directly to the 2_1^+ state at least. Hence, 1403-keV γ-ray was assigned to the $4_1^+ \rightarrow 2_1^+$ transition tentatively in the present study.

The level scheme extracted for ^{42}Si from the present experimental data is shown in

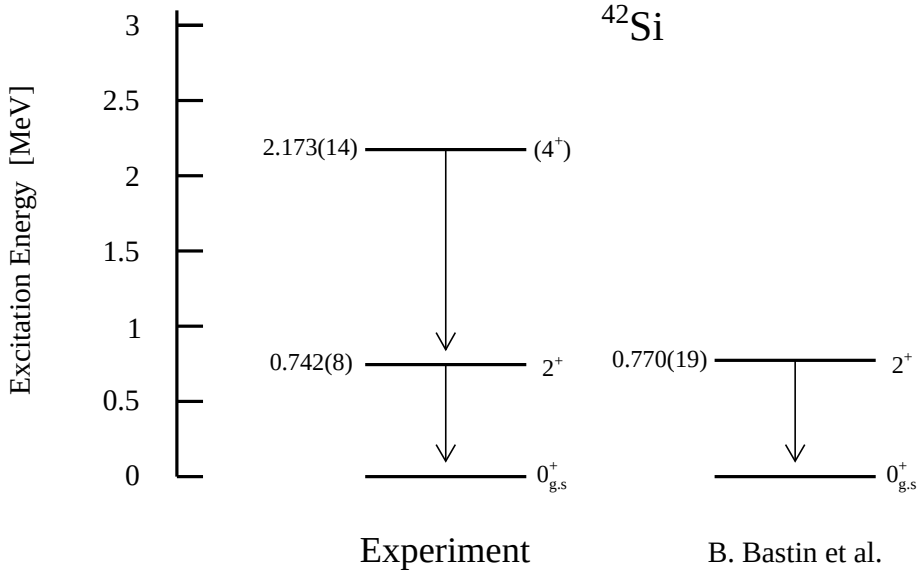

Figure 4.9: The excited level scheme extracted for ^{42}Si from the present experimental data is shown in comparison with a previous work performed by B. Bastin et.al..

Figure 4.9, where the one reported by the previous work [33, 32] is exhibited together for a comparison purpose. The ratio $R_{4/2}$ of the 4_1^+ and 2_1^+ state energies with the value of 2.93(5) was deduced with this scheme.

4.1.5 Summary of Observed γ-rays

The de-excitation γ-rays obtained in this study is summarized in Table 4.1, where the new observables in the present study are indicated by bold text. The energies of observed γ-rays, their intensities, coincidence with other observed γ-rays, and the known or assigned transitions are listed. The γ-ray intensity is given in a relative value to the intensity of $2_1^+ \rightarrow 0_1^+$ transition, and its error includes only the statistical one. The γ - γ analysis and the yield estimation for each γ-ray transition allow tentative spin-parity assignment to the $4_1^+ \rightarrow 2_1^+$ transitions in ^{38,40,42}Si.

4.2 Collectivities and Deformations

Experimentally obtained systematics of the 2_1^+- and 4_1^+- state energy were compared with neighboring isotopes and isotones.

Reaction	E_γ [keV]	I_γ [%]	Coincidence	Transition
C(^{40}S,^{36}Si+γ)	1394(15)	100.0(2.5)	1470	$2_1^+ \rightarrow 0_1^+$
	1470(38)	25.0(2.3)	1394	$4_1^+ \rightarrow 2_1^+$
C(^{40}S,^{38}Si+γ)	1071(12)	100.0(2.5)	1168, 1284	$2_1^+ \rightarrow 0_1^+$
	1168(22)	23.8(2.1)	1071	$(\mathbf{4_1^+}) \rightarrow \mathbf{2_1^+}$
	1284(26)	15.5(1.9)	1071	-
C(^{44}S,^{40}Si+γ)	629(8)	22.2(1.1)	985	$\mathbf{X} \rightarrow \mathbf{2_1^+}$
	985(11)	100.0(1.6)	629, 1539	$2_1^+ \rightarrow 0_1^+$
	1539(16)	37.7(1.4)	985	$(\mathbf{4_1^+}) \rightarrow \mathbf{2_1^+}$
C(^{44}S,^{42}Si+γ)	**516(13)**	-	2032	-
	742(8)	100.0(3.5)	1403, (2032)	$2_1^+ \rightarrow 0_1^+$
	1403(11)	17.0(3.3)	742, (2032)	$(\mathbf{4_1^+}) \rightarrow \mathbf{2_1^+}$
	2032(9)	25.8(3.6)	516, (742), (1403)	-
	2357(15)	11.5(3.3)	-	-

Table 4.1: Summary of observed γ-ray transitions. The intensity is given in a ratio to the yield of $2_1^+ \rightarrow 0_1^+$ transition. The values indicated with bold text were newly obtained in the present study. The $4_1^+ \rightarrow 2_1^+$ transition in ^{38,40,42}Si was tentatively assigned.

Figure 4.10 shows the systematic trend of excitation energies and $R_{4/2}$ values for $N = 22, 24, 26$ and 28 isotones. The left panels show the 2_1^+- and 4_1^+- states energies in even-even isotopes, while the right panels show the $R_{4/2}$ values. As shown in Figure 4.10 (a) and (b), a decrease of 2_1^+ excitation energy and an increase of $R_{4/2}$ ratio are apparent at ^{34}Mg ($Z = 12$) in $N = 22$ isotonic chain. The $N = 22$ isotope ^{34}Mg and ^{32}Ne is considered to be inside the "island of inversion", the region of largely deformed nuclei. The low energy 2_1^+ state and a large $R_{4/2}$ ratio of about 3.2 [20, 46], which is very close to the value 3.3 expected for a rigid rotor, are the evidence for the large enhanced collectivity due to the nuclear deformation [47] and a narrowed shell gap at $N = 20$ [48]. The low energy 2_1^+ state recently observed for ^{32}Ne also suggested the large collectivity [49]. Contrastively, the relatively high energy 2_1^+ state in ^{36}Si and the other $N = 22$ isotones indicates the more stability or the less collectivity compared with ^{34}Mg and ^{32}Ne. The $R_{4/2}$ values around 2.0 also does not show the property of the deformed nuclei. Similar trends of the excitation energies and the ratio $R_{4/2}$ can be seen in the $N = 24$ isotonic chain shown in Figure 4.10 (c) and (d). The changes in systematics occurs in the $N = 26$ isotones. The small increase in the 4_1^+ excitation energies inducing the enhancement of $R_{4/2}$ values are seen at ^{40}Si and ^{46}Ar. The doubly magic stable nuclei ^{48}Ca and ^{42}Si exhibits the drastic changes in systematics from a spherical shape to a deformed shape as shown in Figure 4.10 (g) and (h). The small $R_{4/2}$ value of ^{48}Ca is originating from a typical seniority $\nu = 2$ scheme induced by doubly magic structure. On the other hand, ^{42}Si shows the property of well deformed nuclei with the ratio $R_{4/2} = 2.93$.

Figure 4.11 shows the systematics along the silicon isotopic chain, together with the results of two shell model calculations. The result of the shell model calculation using the effective interaction SDPF-U-MIX [50] are shown in the dashed line. The effective interaction SDPF-U-MIX is an extension of SDPF-U interaction [51], which was designed for $0\hbar\omega$ calculations of the very neutron rich *sd* nuclei around N = 28 in a valence space comprising the full *sd* shell for the protons and the full *pf* shell for the neutrons, meaning that interaction was defined with a core of ^{28}O. The solid line shows the results of the shell model calculation using SDPF-MU interaction, which include the tenor force in the effective interaction [52]. As for the systematics of the ratio $R_{4/2}$, the shell model calculation using SDPF-MU interaction is in better agreement with the experimental results. Enhancement of the ratio $R_{4/2}$ obtained by the present study, together with the lowering of the 2_1^+ state energies due to the development of the nuclear collectivity, suggest a rapid development of deformation from $N = 26$ to ,at least, $N = 28$ along

silicon isotopic chain.

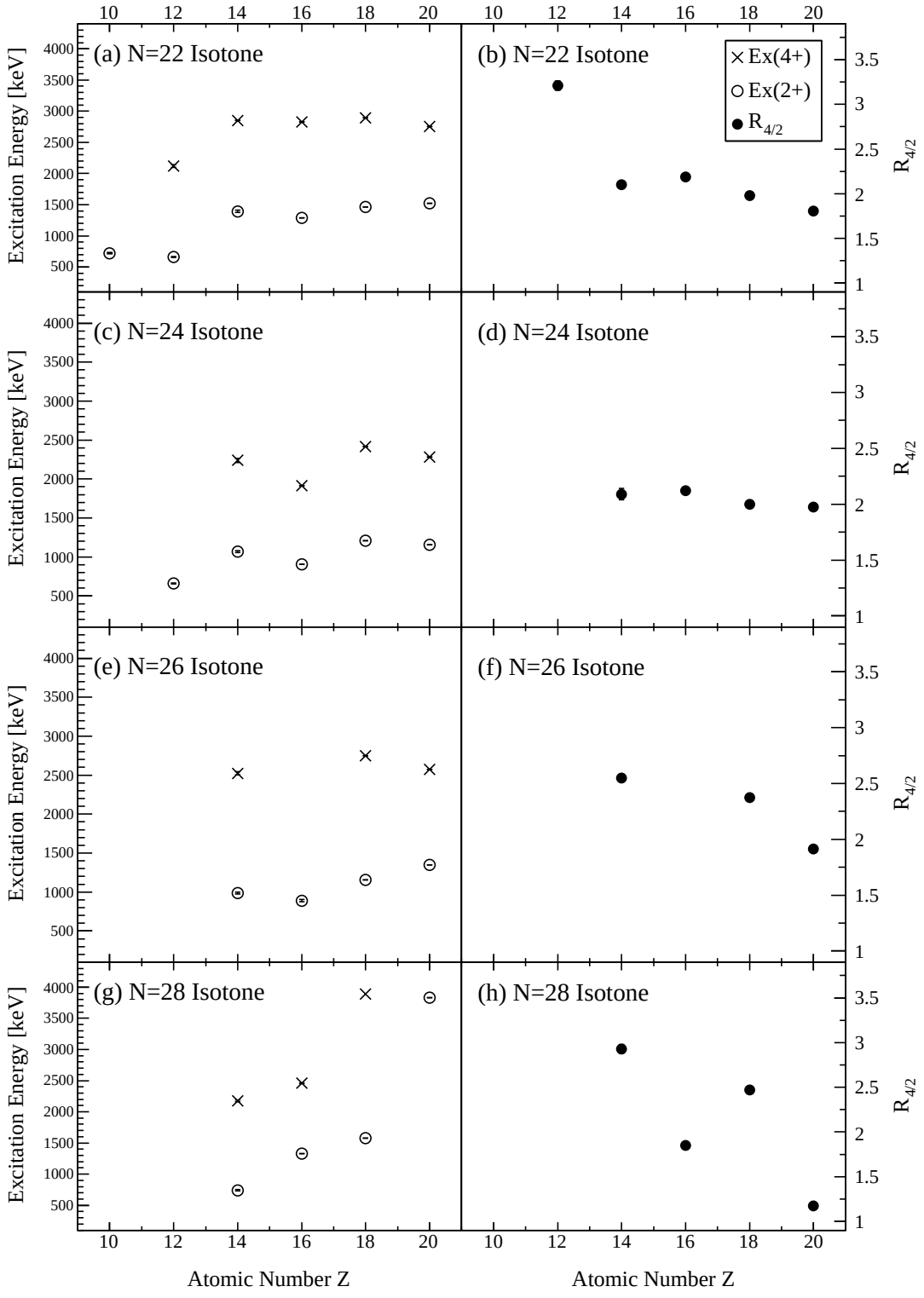

Figure 4.10: Systematics in isotonic chain. Panel (a), (c), (e) and (g) show the excitation energy of the 2_1^+ and the 4_1^+ states for the N=22, 24, 26 and 28 isotones, respectively, while panel (b), (d), (f) and (h) show the $R_{4/2}$ values for each isotonic chain.

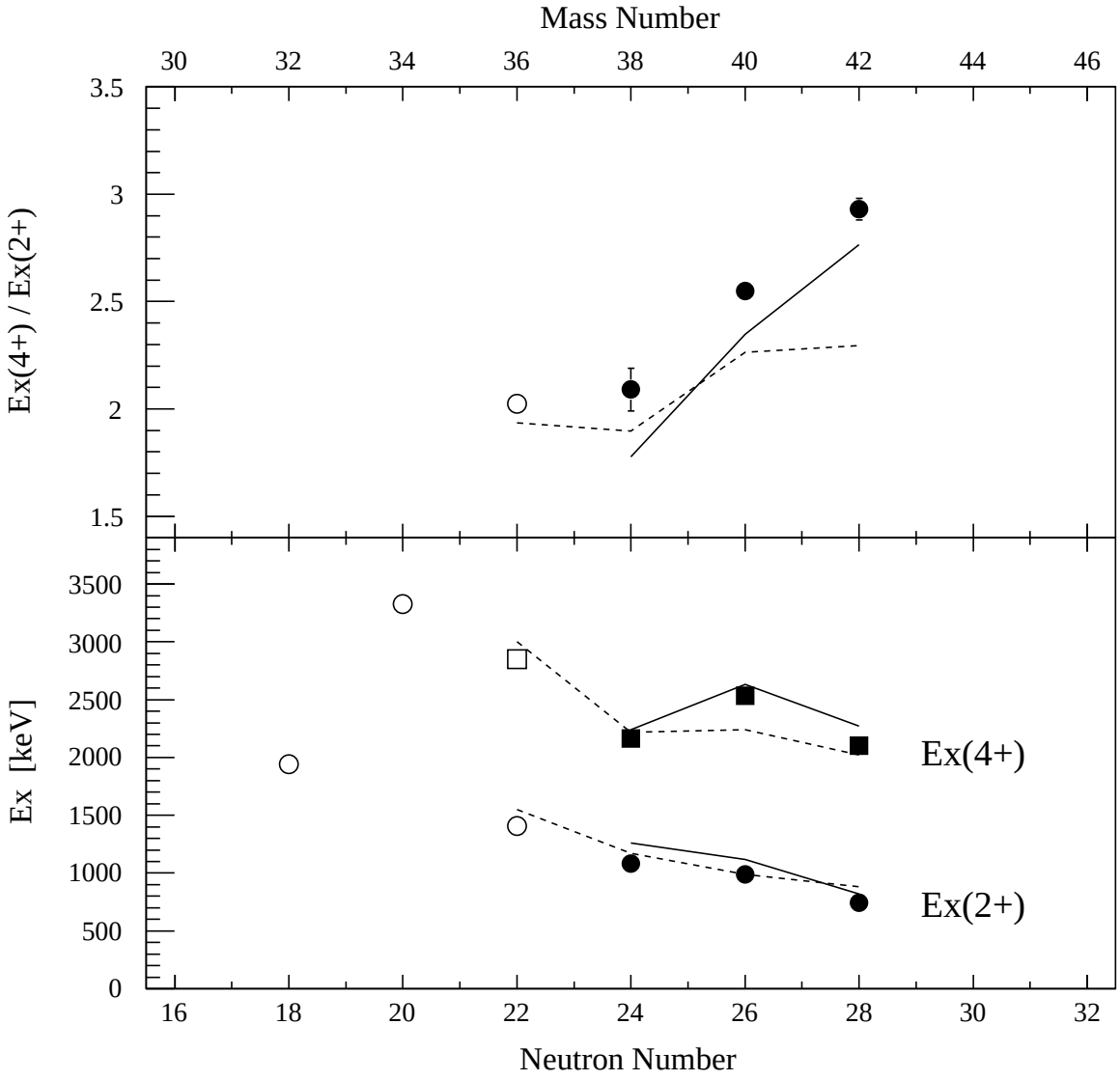

Figure 4.11: Top panel shows the ratio of the energies of the 2_1^+ and 4_1^+ states ($R_{4/2}$) for Si isotopes. Bottom panel shows the excitation energies for the 2_1^+ and the 4_1^+ states indicated by circles and squares, respectively. In both figures, filled symbols show the present results. The dashed- (solid-) line shows the shell model calculation using SDPF-U-MIX (SDPF-MU with tensor force) effective interaction.

Chapter 5

Summary

The excited states in the neutron-rich isotopes ^{38,40,42}Si were studied by in-beam γ-ray spectroscopy. The $N = 28$ isotope ^{42}Si can be regarded as a magic nucleus in the traditional shell model since a large energy gap exists at $N = 28$ due to the spin-orbit splitting. The enhanced collectivity in the vicinity of ^{42}Si, however, have been suggested by the recent studies, which show the lowering of the energies of the 2^+_1 state along the isotopic chain toward $N = 28$. In addition to such information on 2^+_1 states, the systematic data on higher-lying states, which may contribute valuable information on the nature of the nuclear collectivity and/or shell evolution, were required for the further understandings of nuclear structure in this mass region.

The in-beam γ-ray spectroscopy method based on inverse kinematics have been employed for this experimental study. The multi-nucleon removal reactions have been employed to produce the excited states in ^{38,40,42}Si since this reaction has a high accessibility to the highly excited states compared with the inelastic scattering reaction such as Coulomb excitation and proton inelastic scattering. The de-excitation γ-ray from each excited states have been measured by γ-ray spectrometer in coincidence with C(^{40}S,^{38}Si), C(^{44}S,^{40}Si) and C(^{44}S,^{42}Si) reactions.

As the results of the experiment, several new γ-ray transitions were observed for the first time in addition to the previously reported $2^+_1 \rightarrow 0^+_1$ transitions. For the $N = 24$ isotope ^{38}Si, 1168(22)- and 1284(26)-keV γ-ray transitions were newly observed in the present study, and the 1168(22)-keV transition was assigned to the $4^+_1 \rightarrow 2^+_1$ transition by referring the γ-γ coincidence and the intensity of each peak. This tentative assignment of spin-parity was based on the empirically known feature of that population of yrast states are prefered in even-even nuclei produced by the fragmentation-like reactions, such

as multi-nucleon removal reactions employed for the present study. Similar analysis were also applied to the experimental data obtained for C(^{44}S,^{40}Si+γ) reaction, and 1539(16)-keV γ-ray transition was obtained as the candidate for the $4_1^+ \rightarrow 2_1^+$ transition in the $N = 26$ isotope ^{40}Si. Owing to the high intensity primary and secondary beams, the γ-ray transition from the 2_1^+ state to the ground state were also observed with high statistics in ^{42}Si. The low energy 2_1^+ state, previously reported 770(15)-keV γ-ray transition, was observed at 742(8)-keV in the present study, strongly suggesting the enhanced nuclear collectivity and the vanishing of the $N = 28$ magicity. In addition, γ-ray transitions with energies of 516(13)-, 1403(11)-, 2032(9)- and 2357(15)-keV were observed for the first time, and the 1403(11)-keV line was tentatively assigned to the $4_1^+ \rightarrow 2_1^+$ transition.

The energy ratios between the 4_1^+- and the 2_1^+- states, $R_{4/2}$ values, were obtained to be 2.09(5), 2.55(3) and 2.96(5) for ^{38}Si, ^{40}Si and ^{42}Si, respectively, and revealed to be systematically increased and closed to the rotational limit (3.33) along Si isotopic chain toward $N = 28$. The $R_{4/2}$ ratio for ^{38}Si, 2.09(5), are close to the vibrational limit (2.00), suggesting a nearly spherical shape, whereas the one for ^{40}Si increases to 2.55(9), indicating deviation from the spherical shape or enhancement of quadrupole collectivity at $N = 26$. In the case of ^{42}Si, larger value of $R_{4/2}$ ratio of 2.96(5) was obtained though ^{42}Si has the neutron magic number $N = 28$. These results indicate a rapid development of nuclear deformation from $N = 26$ up to at least $N = 28$ and excludes the possibility of a doubly magic nature of ^{42}Si.

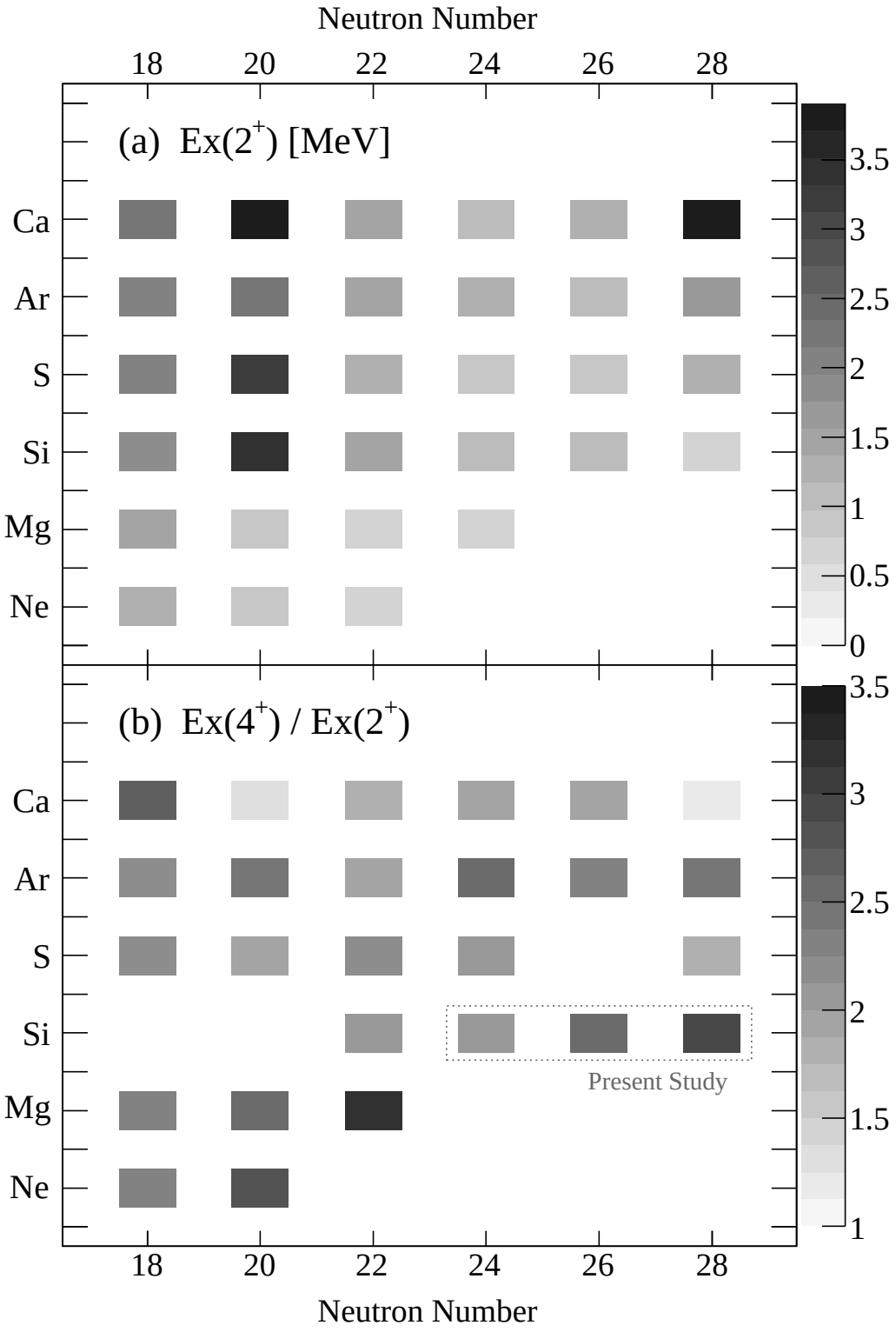

Figure 5.1: The energies of the 2_1^+ states (a) and energy ratios $R_{4/2}$ between 2_1^+ and 4_1^+ state (b) are shown on the nuclear chart in the vicinity of ^{42}Si. Present study exhibited the rapid evolution of the nuclear deformation along Si isotopic chain toward $N = 28$.

Acknowledgements

I would like to express my sincere gratitude to many people for their invaluable advice, supports, and encouragement.

I am particularly indebted to Prof. K. Ieki, my supervisor, who introduced me to this field and has given me patient supports and continuous encouragement. Special thanks are also due to Dr. S. Takeuchi, my thesis adviser, for making great contribution to the present study and for continuous advice and encouragement during my research activity. Without a lot of things I had learned from him, I would not have finished the experiment and this thesis.

I would like to express thanks to all the in-beam gamma group member. My thesis has been proofread by Dr. P. Doornenbal. His comments were always accurate and helpfull feedback. I would like to thank for his advice on data analysis and simulations also. Thanks are also due to Prof. N. Aoi, who introduced me to in-beam gamma spectroscopy and has given me valuable advice and discussions on the experimental nuclear physics. I would like to thank Prof. H. Scheit, Dr. K. Yoneda, Dr. D. Steppenbeck, and Dr. J. Lee for their great help and contribution during and after the experiment. In in-beam gamma group, I have learned as a student together with Dr. W He, Miss L. Honga and Mr. Y. Shiga. I wish to express thanks also to them for their encouragement and friendship. I would like to express my gratitude to Prof. T. Motobayashi and Prof. H .Sakurai for valuable advice, discussions, and supporting my research in RIKEN.

I wish to thank all the members of Center for Nuclear Study, University of Tokyo. I would like to thank Prof. S. Shimoura, Asso. Prof. K. Yako, and Assi. Prof. S. Michimasa. With their continuous encouragement and supports, I could finally submit this thesis. I am also grateful to students in CNS, Mr. H. Miya, Mr S. Go, Mr K. Kisamori, Mr M. Takaki, Mr R. Yokoyama, Mr M. Kobayashi, Mr K. Kobayashi for their help and friendship. Thanks are also due to Miss H. Kim for helping and supporting me continuously.

Many thanks to all the collaborator of this experiment and the members of Radio-

Isotopes Physics Laboratory in RIKEN, Heavy Ion Laboratory in RIKEN, and Nuclear and Radiation Physics Laboratory in Rikkyo University for their continuous support.

Finally, I would like to thank my family and friends for their continuous encouragement and supports.

Bibliography

[1] E. Rutherford. The scattering of α and β particles by matter and the structure of the atom. *Philosophical Magazine Series 6*, 21(125):669–688, 1911.

[2] Maria G. Mayer. On closed shells in nuclei. *Phys. Rev.*, 74:235–239, Aug 1948.

[3] Maria Goeppert Mayer. On closed shells in nuclei. ii. *Phys. Rev.*, 75:1969–1970, 1949.

[4] Maria Goeppert Mayer. Nuclear configurations in the spin-orbit coupling model. i. empirical evidence. *Phys. Rev.*, 78:16–21, 1950.

[5] Otto Haxel, J. Hans D. Jensen, and Hans E. Suess. On the "magic numbers" in nuclear structure. *Phys. Rev.*, 75:1766–1766, 1949.

[6] I. Tanihata, H. Hamagaki, O. Hashimoto, Y. Shida, N. Yoshikawa, K. Sugimoto, O. Yamakawa, T. Kobayashi, and N. Takahashi. Measurements of interaction cross sections and nuclear radii in the light p-shell region. *Phys. Rev. Lett.*, 55:2676–2679, 1985.

[7] J.P. Dufour, R. Del Moral, H. Emmermann, F. Hubert, D. Jean, C. Poinot, M.S. Pravikoff, A. Fleury, H. Delagrange, and K.-H. Schmidt. Projectile fragments isotopic separation: Application to the lise spectrometer at GANIL. *Nuclear Instruments and Methods in Physics Research Section A: Accelerators, Spectrometers, Detectors and Associated Equipment*, 248:267 – 281, 1986.

[8] B.M. Sherrill, D.J. Morrissey, J.A. Nolen Jr., and J.A. Winger. The A1200 projectile fragment separator. *Nuclear Instruments and Methods in Physics Research Section B: Beam Interactions with Materials and Atoms*, 56/57:1106 – 1110, 1991.

[9] H. Geissel, P. Armbruster, K.H. Behr, A. Brunle, K. Burkard, M. Chen, H. Folger, B. Franczak, H. Keller, O. Klepper, B. Langenbeck, F. Nickel, E. Pfeng, M. Pfutzner, E. Roeckl, K. Rykaczewski, I. Schall, D. Schardt, C. Scheidenberger, K.-H. Schmidt,

A. Schroter, T. Schwab, K. Summerer, M. Weber, G. Munzenberg, T. Brohm, H.-G. Clerc, M. Fauerbach, J.-J. Gaimard, A. Grewe, E. Hanelt, B. Knodler, M. Steiner, B. Voss, J. Weckenmann, C. Ziegler, A. Magel, H. Wollnik, J.P. Dufour, Y. Fujita, D.J. Vieira, and B. Sherrill. The GSI projectile fragment separator (FRS): a versatile magnetic system for relativistic heavy ions. *Nuclear Instruments and Methods in Physics Research Section B: Beam Interactions with Materials and Atoms*, 70:286 – 297, 1992.

[10] T. Kubo, M. Ishihara, N. Inabe, H. Kumagai, I. Tanihata, K. Yoshida, T. Nakamura, H. Okuno, S. Shimoura, and K. Asahi. The RIKEN radioactive beam facility. *Nuclear Instruments and Methods in Physics Research Section B: Beam Interactions with Materials and Atoms*, 70:309 – 319, 1992.

[11] H. Wollnik, F.K. Wohn, K.D. Wunsch, and G. Jung. Experimental indication of the onset of nuclear deformation in neutron-rich Sr isotopes at mass 98. *Nuclear Physics A*, 291:355 – 364, 1977.

[12] R.E. Azuma, G.L. Borchert, L.C. Carraz, P.G. Hansen, B. Jonson, S. Mattsson, O.B. Nielsen, G. Nyman, I. Ragnarsson, and H.L. Ravn. The strongly deformed nucleus 100Sr. *Physics Letters B*, 86:5 – 8, 1979.

[13] Hiroyoshi Sakurai. RI Beam Factory Project at RIKEN. *Nuclear Physics A*, 805:526c – 532c, 2008.

[14] C. Thibault, R. Klapisch, C. Rigaud, A. M. Poskanzer, R. Prieels, L. Lessard, and W. Reisdorf. Direct measurement of the masses of ^{11}Li and $^{26-32}$Na with an on-line mass spectrometer. *Phys. Rev. C*, 12:644–657, 1975.

[15] E. K. Warburton, J. A. Becker, and B. A. Brown. Mass systematics for $A = 29$ - 44 nuclei: The deformed $A \sim 32$ region. *Phys. Rev. C*, 41:1147–1166, 1990.

[16] S. Raman, C.W. Nestor JR., and P. Tikkanen. TRANSITION PROBABILITY FROM THE GROUND TO THE FIRST-EXCITED 2+ STATE OF EVEN-EVEN NUCLIDES. *Atomic Data and Nuclear Data Tables*, 78:1 – 128, 2001.

[17] C. Détraz, D. Guillemaud, G. Huber, R. Klapisch, M. Langevin, F. Naulin, C. Thibault, L. C. Carraz, and F. Touchard. Beta decay of $^{27-32}$Na and their descendants. *Phys. Rev. C*, 19:164–176, 1979.

[18] D. Guillemaud-Mueller, C. Detraz, M. Langevin, F. Naulin, M. de Saint-Simon, C. Thibault, F. Touchard, and M. Epherre. β-Decay schemes of very neutron-rich sodium isotopes and their descendants. *Nuclear Physics A*, 426:37 – 76, 1984.

[19] T. Motobayashi, Y. Ikeda, K. Ieki, M. Inoue, N. Iwasa, T. Kikuchi, M. Kurokawa, S. Moriya, S. Ogawa, H. Murakami, S. Shimoura, Y. Yanagisawa, T. Nakamura, Y. Watanabe, M. Ishihara, T. Teranishi, H. Okuno, and R.F. Casten. Large deformation of the very neutron-rich nucleus 32Mg from intermediate-energy Coulomb excitation. *Physics Letters B*, 346:9 – 14, 1995.

[20] K. Yoneda, H. Sakurai, T. Gomi, T. Motobayashi, N. Aoi, N. Fukuda, U. Futakami, Z. Gacsi, Y. Higurashi, N. Imai, N. Iwasa, H. Iwasaki, T. Kubo, M. Kunibu, M. Kurokawa, Z. Liu, T. Minemura, A. Saito, M. Serata, S. Shimoura, S. Takeuchi, Y. X. Watanabe, K. Yamada, Y. Yanagisawa, K. Yogo, A. Yoshida, and M. Ishihara. Deformation of ^{34}Mg Studied via In-Beam γ-Ray Spectroscopy using Radioactive-Ion Projectile Fragmentation. *Phys.Lett.*, 499B:233, 2001.

[21] S. Takeuchi, N. Aoi, T. Motobayashi, S. Ota, E. Takeshita, H. Suzuki, H. Baba, T. Fukui, Y. Hashimoto, K. Ieki, N. Imai, H. Iwasaki, S. Kanno, Y. Kondo, T. Kubo, K. Kurita, T. Minemura, T. Nakabayashi, T. Nakamura, T. Okumura, T. K. Onishi, H. Sakurai, S. Shimoura, R. Sugou, D. Suzuki, M. K. Suzuki, M. Takashina, M. Tamaki, K. Tanaka, Y. Togano, and K. Yamada. Low-lying states in ^{32}Mg studied by proton inelastic scattering. *Phys. Rev. C*, 79:054319, 2009.

[22] H. Iwasaki, T. Motobayashi, H. Akiyoshi, Y. Ando, N. Fukuda, H. Fujiwara, Zs. Flp, K.I. Hahn, Y. Higurashi, M. Hirai, I. Hisanaga, N. Iwasa, T. Kijima, A. Mengoni, T. Minemura, T. Nakamura, M. Notani, S. Ozawa, H. Sagawa, H. Sakurai, S. Shimoura, S. Takeuchi, T. Teranishi, Y. Yanagisawa, and M. Ishihara. Low-lying intruder 1^- state in ^{12}Be and the melting of the N=8 shell closure. *Physics Letters B*, 491:8 – 14, 2000.

[23] H. Simon, D. Aleksandrov, T. Aumann, L. Axelsson, T. Baumann, M. J. G. Borge, L. V. Chulkov, R. Collatz, J. Cub, W. Dostal, B. Eberlein, Th. W. Elze, H. Emling, H. Geissel, A. Grünschloss, M. Hellström, J. Holeczek, R. Holzmann, B. Jonson, J. V. Kratz, G. Kraus, R. Kulessa, Y. Leifels, A. Leistenschneider, T. Leth, I. Mukha, G. Münzenberg, F. Nickel, T. Nilsson, G. Nyman, B. Petersen, M. Pfützner, A. Richter, K. Riisager, C. Scheidenberger, G. Schrieder, W. Schwab,

M. H. Smedberg, J. Stroth, A. Surowiec, O. Tengblad, and M. V. Zhukov. Direct experimental evidence for strong admixture of different parity states in ^{11}Li. *Phys. Rev. Lett.*, 83:496–499, 1999.

[24] A. Ozawa, T. Kobayashi, T. Suzuki, K. Yoshida, and I. Tanihata. New Magic Number, $N = 16$, near the Neutron Drip Line. *Phys. Rev. Lett.*, 84:5493–5495, 2000.

[25] Y. Togano, Y. Yamada, N. Iwasa, K. Yamada, T. Motobayashi, N. Aoi, H. Baba, S. Bishop, X. Cai, P. Doornenbal, D. Fang, T. Furukawa, K. Ieki, T. Kawabata, S. Kanno, N. Kobayashi, Y. Kondo, T. Kuboki, N. Kume, K. Kurita, M. Kurokawa, Y. G. Ma, Y. Matsuo, H. Murakami, M. Matsushita, T. Nakamura, K. Okada, S. Ota, Y. Satou, S. Shimoura, R. Shioda, K. N. Tanaka, S. Takeuchi, W. Tian, H. Wang, J. Wang, and K. Yoneda. Hindered Proton Collectivity in $^{28}_{16}S_{12}$: Possible Magic Number at $Z = 16$. *Phys. Rev. Lett.*, 108:222501, 2012.

[26] R. W. Ibbotson, T. Glasmacher, B. A. Brown, L. Chen, M. J. Chromik, P. D. Cottle, M. Fauerbach, K. W. Kemper, D. J. Morrissey, H. Scheit, and M. Thoennessen. Quadrupole Collectivity in ^{32,34,36,38}Si and the N = 20 Shell Closure. *Phys.Rev.Lett.*, 80:2081, 1998.

[27] L. Gaudefroy, O. Sorlin, D. Beaumel, Y. Blumenfeld, Z. Dombrádi, S. Fortier, S. Franchoo, M. Gélin, J. Gibelin, S. Grévy, F. Hammache, F. Ibrahim, K. W. Kemper, K.-L. Kratz, S. M. Lukyanov, C. Monrozeau, L. Nalpas, F. Nowacki, A. N. Ostrowski, T. Otsuka, Yu.-E. Penionzhkevich, J. Piekarewicz, E. C. Pollacco, P. Roussel-Chomaz, E. Rich, J. A. Scarpaci, M. G. St. Laurent, D. Sohler, M. Stanoiu, T. Suzuki, E. Tryggestad, and D. Verney. Reduction of the Spin-Orbit Splittings at the $N = 28$ Shell Closure. *Phys. Rev. Lett.*, 97:092501, 2006.

[28] S. Grévy, F. Negoita, I. Stefan, N.L. Achouri, J.C. Angélique, B. Bastin, R. Borcea, A. Buta, J.M. Daugas, F. De Oliveira, O. Giarmana, C. Jollet, B. Laurent, M. Lazar, E. Liénard, F. Marchal, J. Mrázek, D. Pantelica, Y. Penionzhkevich, S. Piétri, O. Sorlin, M. Stanoiu, C. Stodel, and M.G. St-Laurent. Observation of the 0_2^+ state in 44S. *The European Physical Journal A - Hadrons and Nuclei*, 25:111–113, 2005.

[29] T. Glasmacher, B.A. Brown, M.J. Chromik, P.D. Cottle, M. Fauerbach, R.W. Ibbotson, K.W. Kemper, D.J. Morrissey, H. Scheit, D.W. Sklenicka, and M. Steiner. Collectivity in 44S. *Physics Letters B*, 395:163 – 168, 1997.

[30] J. Fridmann, I. Wiedenhover, A. Gade, L. T. Baby, D. Bazin, B. A. Brown, C. M. Campbell, J. M. Cook, P. D. Cottle, E. Diffenderfer, D. C. Dinca, T. Glasmacher, P. G. Hansen, K. W. Kemper, J. L. Lecouey, W. F. Mueller, H. Olliver, E. Rodriguez-Vieitez, J. R. Terry, J. A. Tostevin, and K. Yoneda. 'Magic' nucleus ^{42}Si. *Nature(London)*, 435:922, 2005.

[31] J. Fridmann, I. Wiedenhover, A. Gade, L. T. Baby, D. Bazin, B. A. Brown, C. M. Campbell, J. M. Cook, P. D. Cottle, E. Diffenderfer, D. C. Dinca, T. Glasmacher, P. G. Hansen, K. W. Kemper, J. L. Lecouey, W. F. Mueller, E. Rodriguez-Vieitez, J. R. Terry, J. A. Tostevin, K. Yoneda, and H. Zwahlen. Shell structure at N = 28 near the dripline: Spectroscopy of ^{42}Si, ^{43}P, and ^{44}S. *Phys.Rev. C*, 74:034313, 2006.

[32] S. Grevy, B. Bastin, Zs. Dombradi, D. Sohler, N. L. Achouri, J. C. Angelique, F. Azaiez, D. Baiborodin, R. Borcea, C. Bourgeois, A. Buta, A. Burger, R. Chapman, J. C. Dalouzy, A. Drouard, Z. Elekes, S. Franchoo, S. Iacob, B. Laurent, M. Lazar, X. Liang, E. Lienard, J. Mrazek, L. Nalpas, F. Negoita, N. A. Orr, Y. Penionshkevitch, Zs. Podolyak, F. Pougheon, P. Roussel-Chomaz, O. Sorlin, M. Stanoiu, I. Stefan, M. G. Saint-Laurent, F. Nowacki, and A. Poves. First observation of the 2_1^+ excited state in the neutron-rich ^{42}Si. Technical Report ATOMKI 2005 Annual,P13, 2006.

[33] B. Bastin, S. Grevy, D. Sohler, O. Sorlin, Zs. Dombradi, N. L. Achouri, J. C. Angelique, F. Azaiez, D. Baiborodin, R. Borcea, C. Bourgeois, A. Buta, A. Burger, R. Chapman, J. C. Dalouzy, Z. Dlouhy, A. Drouard, Z. Elekes, S. Franchoo, S. Iacob, B. Laurent, M. Lazar, X. Liang, E. Lienard, J. Mrazek, L. Nalpas, F. Negoita, N. A. Orr, Y. Penionzhkevich, Zs. Podolyak, F. Pougheon, P. Roussel-Chomaz, M. G. Saint-Laurent, M. Stanoiu, I. Stefan, F. Nowacki, and A. Poves. Collapse of the N = 28 Shell Closure in ^{42}Si. *Phys.Rev.Lett.*, 99:022503, 2007.

[34] S. Grévy, J.C. Anglique, P. Baumann, C. Borcea, A. Buta, G. Canchel, W.N. Catford, S. Courtin, J.M. Daugas, F. de Oliveira, P. Dessagne, Z. Dlouhy, A. Knipper, K.L. Kratz, F.R. Lecolley, J.L. Lecouey, G. Lehrsenneau, M. Lewitowicz, E. Liénard, S. Lukyanov, F. Maréchal, C. Miehé, J. Mrazek, F. Negoita, N.A. Orr, D. Pantelica, Y. Penionzhkevich, J. Péter, B. Pfeiffer, S. Pietri, E. Poirier, O. Sorlin, M. Stanoiu, I. Stefan, C. Stodel, and C. Timis. Beta-decay half-lives at the N=28 shell closure. *Physics Letters B*, 594:252 – 259, 2004.

[35] B. Jurado, H. Savajols, W. Mittig, N.A. Orr, P. Roussel-Chomaz, D. Baiborodin, W.N. Catford, M. Chartier, C.E. Demonchy, Z. Dlouhý, A. Gillibert, L. Giot, A. Khouaja, A. Lépine-Szily, S. Lukyanov, J. Mrazek, Y.E. Penionzhkevich, S. Pita, M. Rousseau, and A.C. Villari. Mass measurements of neutron-rich nuclei near the and 28 shell closures. *Physics Letters B*, 649:43 – 48, 2007.

[36] A. Gade, P. Adrich, D. Bazin, B. A. Brown, J. M. Cook, C. Aa. Diget, T. Glasmacher, S. McDaniel, A. Ratkiewicz, K. Siwek, and D. Weisshaar. In-Beam γ -Ray Spectroscopy of Very Neutron-Rich Nuclei: Excited States in ^{46}S and ^{48}Ar. *Phys. Rev. Lett.*, 102:182502, 2009.

[37] C. M. Campbell, N. Aoi, D. Bazin, M. D. Bowen, B. A. Brown, J. M. Cook, D. C. Dinca, A. Gade, T. Glasmacher, M. Horoi, S. Kanno, T. Motobayashi, W. F. Mueller, H. Sakurai, K. Starosta, H. Suzuki, S. Takeuchi, J. R. Terry, K. Yoneda, and H. Zwahlen. Measurement of Excited States in ^{40}Si and Evidence for Weakening of the N = 28 Shell Gap. *Phys.Rev.Lett.*, 97:112501, 2006.

[38] Toshiyuki Kubo. In-flight RI beam separator BigRIPS at RIKEN and elsewhere in Japan. *Nuclear Instruments and Methods in Physics Research Section B: Beam Interactions with Materials and Atoms*, 204:97 – 113, 2003.

[39] S. Takeuchi, T. Motobayashi, H. Murakami, K. Demichi, and H. Hasegawa. NaI(Tl) array for in-beam γ-ray spectrometer. *RIKEN Accel. Prog. Rep.*, 36:148, 2003.

[40] H. Kumagai, A. Ozawa, N. Fukuda, K. Summerer, and I. Tanihata. Delay-line ppac for high-energy light ions. *Nuclear Instruments and Methods in Physics Research Section A: Accelerators, Spectrometers, Detectors and Associated Equipment*, 470:562 – 570, 2001.

[41] K. Kimura, T. Izumikawa, R. Koyama, T. Ohnishi, T. Ohtsubo, A. Ozawa, W. Shinozaki, T. Suzuki, M. Takahashi, I. Tanihata, T. Yamaguchi, and Y. Yamaguchi. High-rate particle identification of high-energy heavy ions using a tilted electrode gas ionization chamber. *Nuclear Instruments and Methods in Physics Research Section A: Accelerators, Spectrometers, Detectors and Associated Equipment*, 538:608 – 614, 2005.

[42] H. W. Schnopper, Hans D. Betz, J. P. Delvaille, K. Kalata, A. R. Sohval, K. W. Jones, and H. E. Wegner. Evidence for Radiative Electron Capture by Fast, Highly Stripped Heavy Ions. *Phys. Rev. Lett.*, 29:898–901, 1972.

[43] W. R. Leo. *Techniques for Nuclear and Particle Physics Experiments*. Second edition.

[44] X. Liang, F. Azaiez, R. Chapman, F. Haas, D. Bazzacco, S. Beghini, B. R. Behera, L. Berti, M. Burns, E. Caurier, L. Corradi, D. Curien, A. Deacon, G. de Angelis, Zs. Dombradi, E. Farnea, E. Fioretto, A. Hodsdon, A. Gadea, F. Ibrahim, A. Jungclaus, K. Keyes, A. Latina, S. Lunardi, N. Marginean, R. Menegazzo, G. Montagnoli, D. R. Napoli, F. Nowacki, J. Ollier, A. Papenberg, G. Pollarolo, V. F. E. Pucknell, M. D. Salsac, F. Scarlassara, J. F. Smith, K. Spohr, M. Stanoiu, A. M. Stefanini, S. Szilner, N. Toniolo, M. Trotta, D. Verney, Z. Wang, and J. Wrzesinski. Study of the neutron-rich nucleus ^{36}Si. *Phys.Rev. C*, 74:014311, 2006.

[45] C. M. Campbell, N. Aoi, D. Bazin, M. D. Bowen, B. A. Brown, J. M. Cook, D. C. Dinca, A. Gade, T. Glasmacher, M. Horoi, S. Kanno, T. Motobayashi, L. A. Riley, H. Sagawa, H. Sakurai, K. Starosta, H. Suzuki, S. Takeuchi, J. R. Terry, K. Yoneda, and H. Zwahlen. Quadrupole collectivity in silicon isotopes approaching neutron number N=28. *Phys.Lett. B*, 652:169, 2007.

[46] K. Yoneda. *In-Beam Gamma Spectroscopy of the Neutron-Rich Nucleus ^{34}Mg via Radioactive-Isotope Projectile Fragmentation*. PhD thesis, University of Tokyo, 2003.

[47] H. Iwasaki, T. Motobayashi, H. Sakurai, K. Yoneda, T. Gomi, N. Aoi, N. Fukuda, Zs. Fulop, U. Futakami, Z. Gacsi, Y. Higurashi, N. Imai, N. Iwasa, T. Kubo, M. Kunibu, M. Kurokawa, Z. Liu, T. Minemura, A. Saito, M. Serata, S. Shimoura, S. Takeuchi, Y. X. Watanabe, K. Yamada, Y. Yanagisawa, and M. Ishihara. Large Collectivity of ^{34}Mg. *Phys.Lett.*, 522B:227, 2001.

[48] Y. Utsuno, T. Otsuka, T. Mizusaki, and M. Honma. Varying Shell Gap and Deformation in N $\sim$ 20 Unstable Nuclei Studied by the Monte Carlo Shell Model. *Phys.Rev.*, C60:054315, 1999.

[49] P. Doornenbal, H. Scheit, N. Aoi, S. Takeuchi, K. Li, E. Takeshita, H. Wang, H. Baba, S. Deguchi, N. Fukuda, H. Geissel, R. Gernhauser, J. Gibelin, I. Hachiuma, Y. Hara, C. Hinke, N. Inabe, K. Itahashi, S. Itoh, D. Kameda, S. Kanno, Y. Kawada, N. Kobayashi, Y. Kondo, R. Krucken, T. Kubo, T. Kuboki, K. Kusaka,

M. Lantz, S. Michimasa, T. Motobayashi, T. Nakamura, T. Nakao, K. Namihira, S. Nishimura, T. Ohnishi, M. Ohtake, N. A. Orr, H. Otsu, K. Ozeki, Y. Satou, S. Shimoura, T. Sumikama, M. Takechi, H. Takeda, K. N. Tanaka, K. Tanaka, Y. Togano, M. Winkler, Y. Yanagisawa, K. Yoneda, A. Yoshida, K. Yoshida, and H. Sakurai. Spectroscopy of ^{32}Ne and the "Island of Inversion". *Phys.Rev.Lett.*, 103:032501, 2009.

[50] F. Rotaru, F. Negoita, S. Grevy, J. Mrazek, S. Lukyanov, F. Nowacki, A. Poves, O. Sorlin, C. Borcea, R. Borcea, A. Buta, L. Caceres, S. Calinescu, R. Chevrier, Zs. Dombradi, J. M. Daugas, D. Lebhertz, Y. Penionzhkevich, C. Petrone, D. Sohler, M. Stanoiu, and J. C. Thomas. Unveiling the Intruder Deformed 0_2^+ State in ^{34}Si. *Phys.Rev.Lett.*, 109:092503, 2012.

[51] F. Nowacki and A. Poves. New effective interaction for $0\hbar\omega$ shell-model calculations in the *sd-pf* valence space. *Phys. Rev. C*, 79:014310, 2009.

[52] Takaharu Otsuka, Toshio Suzuki, and Yutaka Utsuno. Exotic Nuclei and Yukawa's Forces. *Nuclear Physics A*, 805:127c – 136c, 2008.